AN EXAMINATION INTO THE EFFECTS OF CORROSION BLENDS ON STURDY, INTEGRALLY STIFFENED AIRCRAFT COMPRESSION PANELS

by

Jason Andrew Jauchler

A thesis submitted to the faculty of
The University of Utah
in partial fulfillment of the requirements for the degree of

Master of Science

Department of Mechanical Engineering

The University of Utah

May 2017

The University of Utah Graduate School

STATEMENT OF THESIS APPROVAL

The thesis of **Jason Andrew Jauchler**

has been approved by the following supervisory committee members:

Kenneth L. DeVries	, Chair	**11/10/2016** Date Approved
Daniel Adams	, Member	**11/10/2016** Date Approved
Mark L. Thomsen	, Member	**11/10/2016** Date Approved

and by **Timothy A. Ameel** , Chair/Dean of

the Department/College/School of **Mechanical Engineering**

and by David B. Kieda, Dean of The Graduate School.

ABSTRACT

Corrosion of aircraft structures is of utmost concern to operators of aging aircraft fleets. Ongoing research abounds in methods to control, prevent, and detect corrosion damage. For corrosion which inevitably manifests on an aircraft surface, however, removal of the corrosion products by mechanical means is a necessary action. This study examines the effects of such corrosion blends on the overall buckling resistance of integrally stiffened upper wing skin panels.

Damage parameters considered in this study include center-of-panel blends on the outer skin surface ranging from depths of 0% to 75% of the skin thickness. A relationship was found between the lost load carrying capability of a blended panel and a function of its lost cross-sectional area. It was also found that this relationship can be closely approximated through minor modifications to traditional analytical methods, without the need for more complex numerical methods such as finite element analysis. Although the finite element method is capable of explicitly addressing local surface blends, experimental validation of such results is often expensive, time consuming, and unavailable to the typical structures analyst.

TABLE OF CONTENTS

Appendices

LIST OF TABLES

Table

ACKNOWLEDGMENTS

It is with much gratitude that I thank all involved in this project for their support, encouragement, and technical expertise over the past several years.

Many thanks go out to Dallen Andrew, Thom Hooks, Jody Cronenberger, Luciano Smith, Jim Feiger, and everyone at Southwest Research Institute who supported the testing portions of this project. Your knowledge and enthusiasm in the early phases of this venture ensured a solid foundation on which to build. Thank you also to Dr. Mark Thomsen and Jason Hamburg of Hill Air Force Base for your encouragement and support in getting this project off the ground. Thank you to Andrew Clark, Marcus Stanfield, and Roger Beal, also of Hill Air Force Base, for answering my many questions along the way.

Most importantly, I would like to thank my wife and children for their continued patience, encouragement, and devotion through this effort, which likely surpassed my own. I absolutely could not have done it without you.

CHAPTER 1

INTRODUCTION

1.1 Aging Aircraft

The problem of aging aircraft fleets presents unique challenges to the engineering community. Fleet-wide inspection programs must be capable of detecting the products of aging, and maintenance programs must be capable of addressing them. The Federal Aviation Administration has identified the following as some of its primary areas of concern: widespread fatigue damage, degradation of electrical wiring and fuel tank sealant, damage tolerance-based inspection and repair programs, and corrosion prevention and control [1]. One need only survey recent conference proceedings on the subject of aging aircraft to see that the problem of widespread fatigue damage and associated damage tolerance analysis methodologies are ubiquitous research subjects. Corrosion research, for its part, often revolves around prevention, detection, and better understanding of corrosion-fatigue synergism [2]. This approach is attractive from a research standpoint as well as an axiomatic mindset (i.e., an ounce of prevention is worth a pound of cure). It cannot be overstated, however, that repair methodologies are necessary for the inevitable damage that presents itself *despite our best efforts to the contrary*.

It is important to note that aging effects can be time-based (sealant degradation), usage-based (fatigue), environment-based (corrosion), or more typically, some

combination of the above. Thus, single-factor approaches to reduce the effects of aging, such as simply reducing flight hours or flight severity, do not fully address or solve what is often a more complex set of problems. In other words, maintenance costs can be expected to increase with aircraft age, even if aircraft usage remains within the original design service objective (DSO). An illustration of this trend is seen in Figure 1 for a sampling of large transport aircraft.

The data points in Figure 1 show a rough trend of depot maintenance costs doubling approximately every ten years. The shaded area along the X-axis implies a 20 to 30 year typical DSO for large transport aircraft [4], though factors such as spectrum

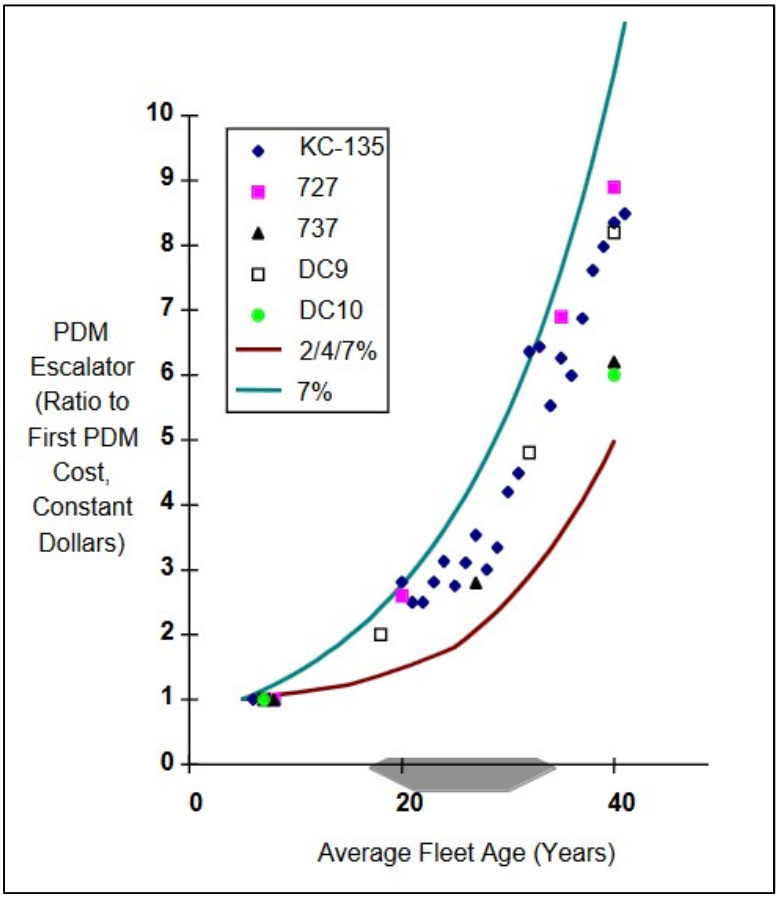

Figure 1 Costs of Programmed Depot Maintenance (PDM) for Aging Fleets [3]

severity make direct comparisons between time in service and DSO problematic. Civil and military organizations continue to struggle with both the safety and economic concerns (which are not necessarily exclusive of one another) inherent to aging aircraft fleets. The Federal Aviation Administration has codified a series of associated maintenance and repair requirements to address many of these concerns [5]. The United States Air Force, however, has presented possibly the most comprehensive evaluation regarding the economic consequences of aging on an aircraft fleet. Its Scientific Advisory Board has the following to say on the subject of parts supportability and obsolescence [6]:

> Diminishing Manufacturing Sources become an increasing sustainment issue as aircraft age and Original Equipment Manufacturer (OEM) involvement is reduced…
>
> Remanufacturing is expensive. One has to take the aircraft apart and reassemble it in order to accomplish the task and it cannot always be done without complete removal and reinstallation of systems in order to rebuild the structure around these systems. Thus, remanufacturing is very manpower intensive involving much "touch" labor and few opportunities for automation. The consequence of these actions is that costs for each Programmed Depot Maintenance cycle are increased markedly as the platform ages. Depot cycles are planned around parts obsolescence and usage – fatigue crack initiation and growth. But, aging (corrosion, sealant and wiring degradation, and exposure to ultraviolet light) adds additional failure modes and life limitations that reduce planned maintenance intervals or increase the work associated with maintaining these components. In addition, life extension requires continued airworthiness assessments and qualifications, involving structural life extension programs and many other expensive activities…
>
> Commercial airlines maintenance procedures differ from those used in the USAF. They maintain aircraft at flight capable rates exceeding 90% (K. Davis, Senior Principal Engineer, Delta TechOps, Personal Communication, March 24, 2011) versus the 65-70% rates seen for large transport aircraft in the USAF. *They do as much repair and maintenance in the field as possible and minimize depot maintenance*, and they document the predicted depot maintenance so they know what parts are required before the aircraft ever hits the tarmac at the depot. This allows commercial airlines to run aircraft through the depot in 30-45 days (versus the USAF 180-280 days) and schedule them so they are ready with the next

> induction as the prior is rolled out the door (K. Davis, Personal Communication, March 24, 2011). *They have as few aircraft on the ground at the depot as possible because aircraft on the ground do not earn money*. It is a different paradigm than the Air Force where every aircraft costs the USAF money whether it flies or not. (Emphasis added.)

An obvious conclusion from the above excerpts is that significant cost savings can be expected through actions that include (but are not limited to) salvaging damaged aircraft structure without replacing it and performing aircraft maintenance in a manner which requires as little structural disassembly as possible. One of the ways in which these actions can be accomplished is through simple material removal. Oversizing of damaged holes and blending of damaged structure (often due to corrosion damage and/or tool strikes) are two of the more common examples. Given conservative engineering assumptions during an aircraft's design phase, positive safety margins in its stress reports, and/or more accurate (i.e., less conservative) repair analysis methodologies, it may be possible to verify safety of flight following removal of structural material without the need for repair doublers or other means of restoring lost load carrying ability.

1.2 Structural Considerations

1.2.1 Sturdy Integrally Stiffened Panels

Aircraft wing loading generally decreases in magnitude from inboard to outboard. This change in loading along the span of a wing has implications to the design of the wing structure. An inefficient design carries penalties in both cost and weight, whereas an efficient design requires thorough analysis to optimize the structure [7]. This optimization is typically achieved through reductions in cross-sectional area as the loading magnitude decreases. Integrally stiffened panels have become a common structural feature in aircraft wing skins due to their cost and weight savings over more conventional designs (such as

a built-up structure of extruded shapes bolted or riveted to a plate-style skin) [7]. See Figure 2 for an example of a five stringer section of integrally stiffened panel. This example is a section cut from between wing rib stations; a typical panel would be much longer in the axial (extruded) direction.

Although integrally stiffened panels are prevalent on both upper and lower wing skin structures, the nature of the loading on these structures is quite different (as is the nature of associated analysis and repair strategies). Tension loading generally dominates in lower wing skins where an understanding of fatigue behavior is necessary [8]. Conversely, compressive loading generally dominates in upper wing skins where an understanding of inherent cross-sectional stability becomes more important. There are a number of accepted analytical methods for determining the compressive load carrying capability of an integrally stiffened panel, as well as newer numerical approaches such as the finite strip method and finite element method. These methods are examined in further detail in later sections of this report. The use of the word “sturdy” in the context of this

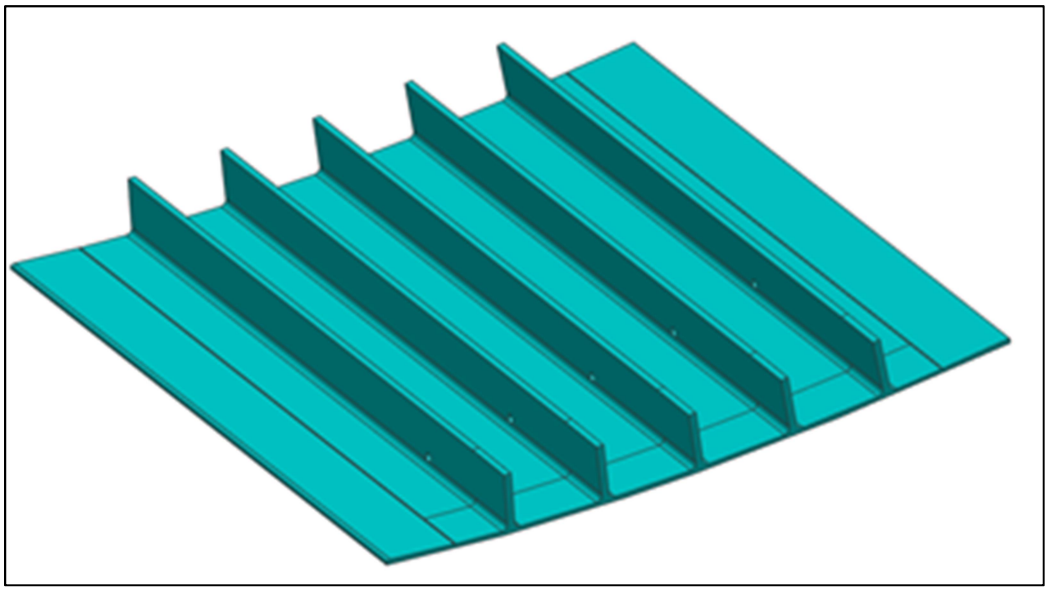

Figure 2 Five Stringer Integrally Stiffened Panel

report is loosely defined as “when the proportions of a stiffener are such that it is sturdy with respect to the plate which it is stiffening” [9].

1.2.2 Corrosion Blends

Removal of corrosion products from aircraft surfaces by mechanical means (i.e., blending) is both a standard and necessary practice, and appropriate maintenance procedures are well documented [10]. The basic principle involves removing all corrosion products from the aircraft surface, as well as any fatigue cracks which may have formed concurrent with the corrosion. By tapering the blend back into the surrounding structure, stress concentrations due to blending can be reduced to as low as 1.1 for a 20:1 taper ratio [11]. Taper ratios of 10:1 or greater are typically utilized in the direction of primary loading, whereas taper ratios as low as 5:1 may be authorized in the transverse direction [10]. Illustrations of various blend strategies are shown in Figure 3 and Figure 4.

1.3 Project Overview

Appropriate analysis methods to account for the presence of surface blends are uncommon, especially in the context of compressive loading and structural stability. A review of applicable literature revealed very little in the way of research into this subject despite its obvious similarities to the problem of cutouts in compression structure, a design feature described as “one of the most troublesome problems in stress analysis” [11]. Although the stability impacts of local changes in cross section are examined in several studies, the conclusions are typically presented in a manner that does not support analytical methods (as opposed to numerical methods such as the finite element method

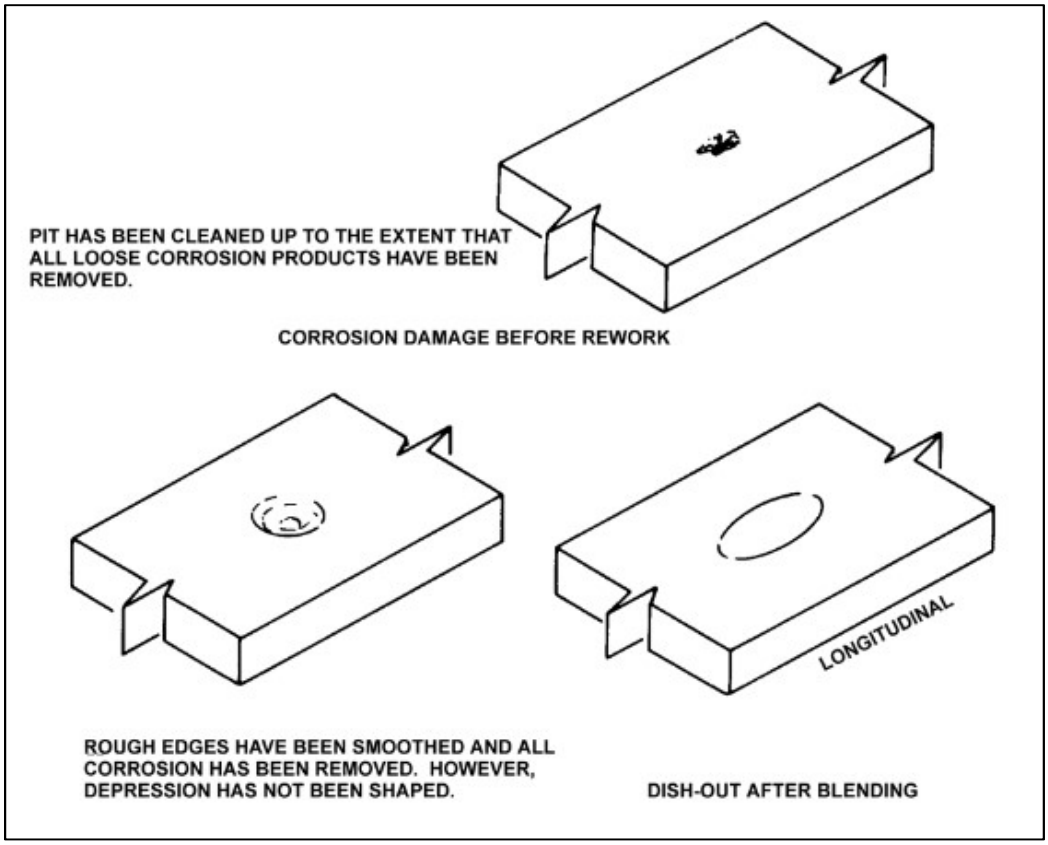

Figure 3 Blending of Isolated Corrosion Damage [10]

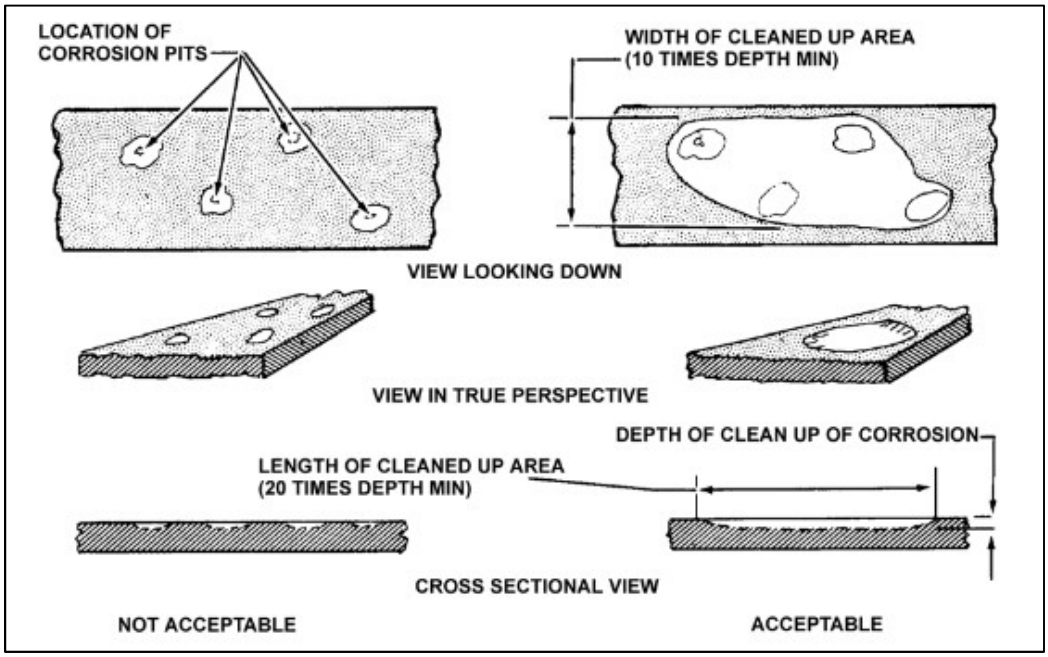

Figure 4 Corrosion Cleanup Parameters [10]

or finite strip method) [7], [12], [13]. Other studies have focused on developing computationally inexpensive methods for stability analysis, but with a focus on simplifying the optimization of panel shapes for new design (i.e., local changes in cross section are not explored) [14], [15].

This study attempts to characterize the impacts to the compressive load carrying capability of an integrally stiffened panel due to blending of corrosion damage, and to do so in a manner conducive to use in analytical rather than numerical methods. That said, finite element analysis simulations are used to generate the bulk of the comparative data. Although finite element analysis is generally known to be capable of accurately predicting buckling loads for complex shapes, it is also generally accepted that experimental validation of computer simulations is appropriate. Thus, this study includes both finite element simulations and experimental evaluations. Additionally, this study compares the finite element results to the results of more traditional closed-form analysis methods (which are typically unable to account for local changes in cross section such as those due to a surface blend).

Structural stability is highly influenced by both the shape of a structure as well as its material properties [7]. While material properties are readily available in engineering databases, such references typically utilize statistically conservative values [16] which may not correlate well with experimental results. Therefore, material property testing is added as a necessary component of this study.

Due to the nature of this study, all numerical simulations rely solely on nonlinear finite element methods. Neither the finite strip method nor eigenvalue (linear) buckling are explored. The finite strip method is not expected to yield any benefits over the finite

element method, and it is of limited value in simulating geometric features which are not constant along the axial length of the specimen (such as a local blend and/or sections of tapering thickness) [13]. Eigenvalue buckling analysis is equally unsuitable for the purposes of this study due to its inability to predict postbuckling phenomena [12], [14].

There are a nearly infinite number of possible permutations of panel shapes, stringer types, blend shapes, blend sizes, and blend locations available for examination. It is therefore necessary to place limitations on the scope of this study. Panel geometry and stringer type are limited by the materials available for study. The experimental portions of this study utilize integral stiffeners which were cut from the upper wing skin of an operational aircraft (the aircraft type is intentionally omitted for the purposes of protecting sensitive and/or proprietary design information). Previous studies have highlighted the difficulties in drawing stability-related conclusions from a small sample size [12]. Therefore, each stringer panel was cut into a series of "pi shaped" dual-stringer sections with the intent of maximizing the number of specimens available for testing. Blend location for all specimens is placed at the center of the panel on its outer skin surface. Multiple blend shapes, sizes, and taper ratios are considered in this study. All blends taper to a single point at their geometric center.

Ultimately, it is intended that the results of this study will support engineering analyses for maintenance and repair of the aircraft type from which the skin specimens were cut. It is not within the scope of this study to develop empirical data in support of all possible panel geometries and/or blend shapes (a rather massive undertaking). However, it is hoped that this study can be used as a baseline for further evaluations of alternate panel geometries and/or blend shapes. The experimental portions of this study may be

valuable in validating future finite element studies, a conglomeration of which may be used to expand the amount of data available for empirical evaluation.

CHAPTER 2

TEST SETUP AND EQUIPMENT

2.1 Test Phases

The experimental portion of this study was broken into three test phases: 1) compression testing of aircraft skin specimens; 2) compression testing of bar specimens; and 3) compressive modulus testing. Basic details of the test phases are provided below, with more specific specimen details following in later sections.

Phase 1 (compression testing of aircraft skin specimens) produced the primary data of interest. Ten specimens were tested in total. Five of these specimens were tested in nominal condition (as cut from the aircraft) and five specimens were tested with machined blends of varying depth.

Phase 2 (compression testing of bar specimens) is included in this study due to the simplicity of analytical evaluations of rectangular cross sections (i.e., no local buckling effects). The results are intended to provide verification of the elastic restraint utilized in the test specimen fixturing. Three bar specimens were tested, each in an unblended condition.

Phase 3 (modulus testing) was included in order to determine various material properties for each of the test materials. The primary data of interest is the compressive modulus (E_c) and the compressive yield stress (F_{cy}), though the stress/strain data are used for additional material characterizations in later portions of this study. Due to the

significance of these values in closed-form buckling calculations [11], [17], it is imperative that the analyses performed in this study utilize experimentally verified values rather than statistically conservative values from material databases. The difficulty in validating finite element results against experimental results without specific material testing is also noted [12]. Six specimens were tested in this phase, including two from the forward aircraft skin, two from the aft aircraft skin, and two from the bar specimen material stock.

It is noted that test phase 3 is probably more appropriately titled "stress/strain testing" rather than "modulus testing" due to the actual data captured from this test phase. Nevertheless, both the test setup and the coupon design are representative of standard test methods for modulus determination, regardless of the results which are ultimately derived. Therefore, for the purposes of simple and consistent verbiage, this report utilizes a "modulus" qualifier for all relevant details of test phase 3 (e.g., "modulus testing" and "modulus specimens").

2.2 Test Specimens

2.2.1 Aircraft Skin Specimens

In order to reduce specimen manufacturing costs, as well as provide direct applicability to an existing aircraft design, all aircraft skin specimens were cut directly from an upper wing skin retired from an operational aircraft. The particular wing selected for this experiment had previously been removed from operational service for unspecified reasons. In the interests of limiting the distribution of potentially sensitive aircraft design data, the aircraft type is intentionally omitted from this report, as are geometry details which are not necessary for validation and/or duplication of the experiment.

All skin specimens were cut from the aircraft's upper wing skin, which itself is made up of a forward skin panel and an aft skin panel. The forward and aft panels are both manufactured from 7075-T76511 aluminum alloy extrusion and include a series of integral stiffeners. Although the forward and aft skin panels are of the same alloy and temper, they are not necessarily from the same material or production lots. Rough sections were cut from between wing rib and spar locations. These rough sections were then further divided into multiple "pi shaped" (dual-stringer) test specimens. This geometry was chosen in order to maximize the number of test specimens which could be obtained, while also allowing for a high resistance against out of plane buckling ($I_{yy} >> I_{xx}$). Therefore, lateral edge support was deemed unnecessary during compression testing.

Several factors limited the number of specimens which could be utilized for testing, including the presence of fuel line holes and access panel cutouts on the as-manufactured wing skins, noncontinuous thicknesses (e.g., chemical milled steps), existing service damage and associated repairs, and attaching/mating structure (see Figure 5 for examples of some of these features). Only ten specimens could be obtained which, in the judgement of this author, were reasonably continuous so as to not introduce unpredictable geometric irregularities. Overall specimen cross-sectional geometry is detailed in Figure 6, with specific dimensions for each specimen listed in Table 1. Dimensions shown are only for the portion of each specimen located within the test section (i.e., the unsupported column).

2.2.2 Bar Specimens

As previously noted, the bar specimens utilize a simple, rectangular cross section for ease of comparison between analytical predictions and test results. Bar specimen

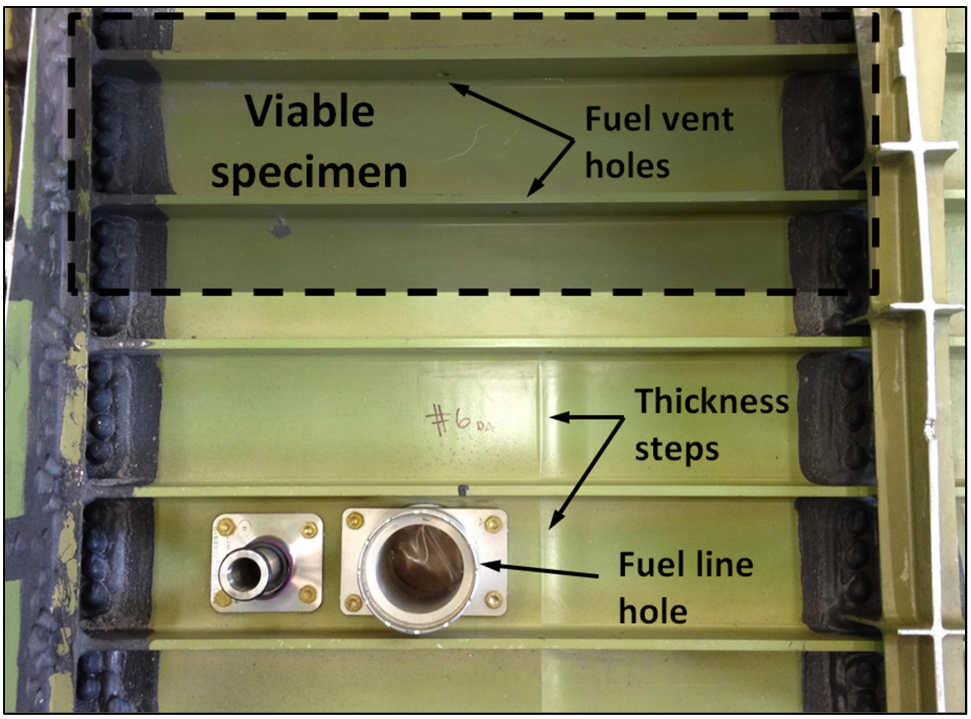

Figure 5 Skin Discontinuities

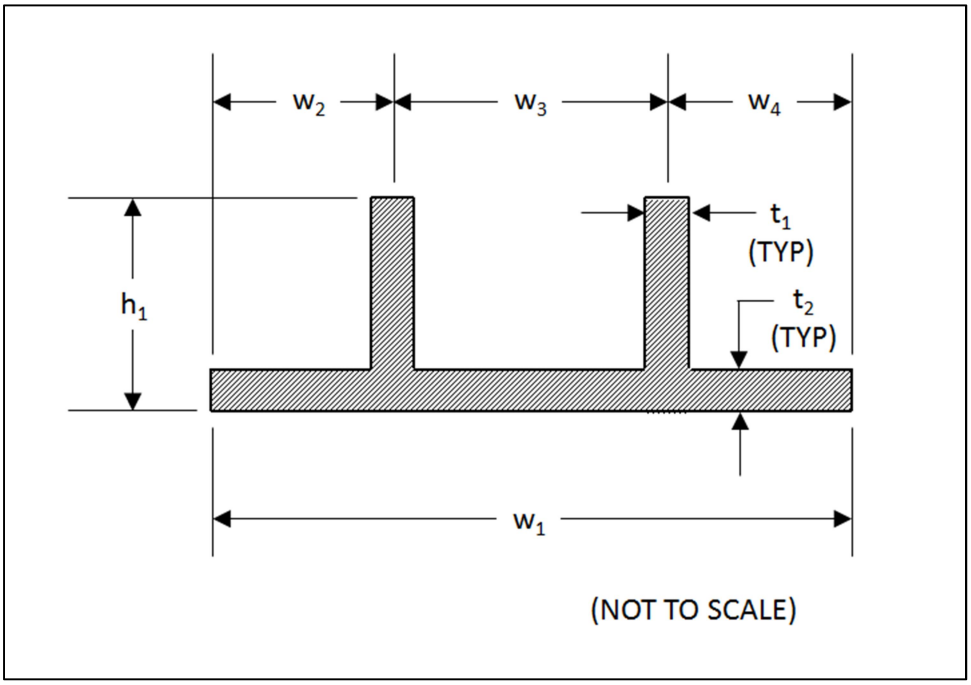

Figure 6 Skin Specimen Cross Section

Table 1 Skin Specimen Geometry

Specimen	t_1 (in)	t_2 (in)	w_1 (in)	w_2 (in)	w_3 (in)	w_4 (in)	h_1 (in)	$L_{vent\ hole}$ (in)[1]	L_{column} (in)
2B	Linear Taper 0.222-0.202	Linear Taper 0.177-0.172	8.062	1.995	4.079	1.988	2.041-2.121 Stepped[2]	15.00, 16.00	24.10
2C	Linear Taper 0.222-0.202	Linear Taper 0.177-0.170	8.074	1.999	4.084	1.991	2.030-2.109 Stepped[2]	13.13, 14.19	24.27
3B	Linear Taper 0.308-0.279	Linear Taper 0.200-0.194	8.095	2.024	4.039	2.032	Linear Taper 2.524-2.277	17.19, 18.13	21.77
3C	Linear Taper 0.307-0.277	Linear Taper 0.205-0.197	8.080	2.025	4.049	2.006	Linear Taper 2.535-2.290	15.19, 16.25	22.02
5B	0.312	0.196	8.085	2.037	4.038	2.010	2.527	18.89, 19.75	21.33
5C	0.313	0.199	8.081	2.014	4.071	1.996	2.543	16.00, 17.00	21.24
7B	Linear Taper 0.275-0.240	Linear Taper 0.211-0.191	8.092	2.027	4.046	2.019	Linear Taper 2.319-2.045	17.50, 18.50	21.60
7C	Linear Taper 0.273-0.239	Linear Taper 0.215-0.194	8.079	2.022	4.053	2.004	Linear Taper 2.331-2.057	15.63, 16.63	21.85
8B	Linear Taper 0.236-0.217	Linear Taper 0.190-0.170	8.083	2.006	4.078	1.999	Linear Taper 2.152-2.035	12.63, 13.50	21.65
8C	Linear Taper 0.238-0.217	Linear Taper 0.184-0.166	8.081	2.005	4.075	2.001	Linear Taper 2.138-2.021	10.50, 11.50	21.66

[1] See Appendix A for fuel vent hole geometry overview.

[2] See Appendix A for details of the specimen 2B and 2C stepped profile.

material is 7075-T7651 aluminum plate with an approximate cross section of 0.50 x 1.75 in. These dimensions were chosen to ensure that structural instability (column failure) occurs in the elastic range, with a moment of inertia ratio (I_{yy} / I_{xx}) similar to that of the aircraft skin specimens. See Table 2 for full geometry details. As before, the length dimension includes only the portion of each specimen located inside the test section.

2.2.3 Modulus Specimens

Specimens intended for modulus testing were taken from "leftover" phase 1 and phase 2 materials. Two modulus specimens were obtained from each of the primary test materials (forward wing skin, aft wing skin, and bar specimen material stock), for a total of six modulus specimens. Modulus specimen geometry is shown in Figure 7.

2.3 Specimen Preparation

2.3.1 Final Machining

Requirements for specimen processing and finishing were necessary to prevent skewing of test results. Ideally, the loaded edges of all specimens were to be flat and parallel within 0.0005 in/in and perpendicular to the lateral edges within 0.05°, with fixturing (or "bearing blocks") machined flat and parallel within 0.0002 in/in before beginning each test [17]. Postmachining specimen quality measurements revealed that

Table 2 Bar Specimen Geometry

Specimen	t (in)	w (in)	A (in^2)	I (in^4)	ρ (in)	L_{column}
FP-1	0.504	1.749	0.8815	0.0187	0.1455	21.79
FP-2	0.503	1.748	0.8792	0.0185	0.1452	21.66
FP-3	0.503	1.749	0.8797	0.0185	0.1452	21.48

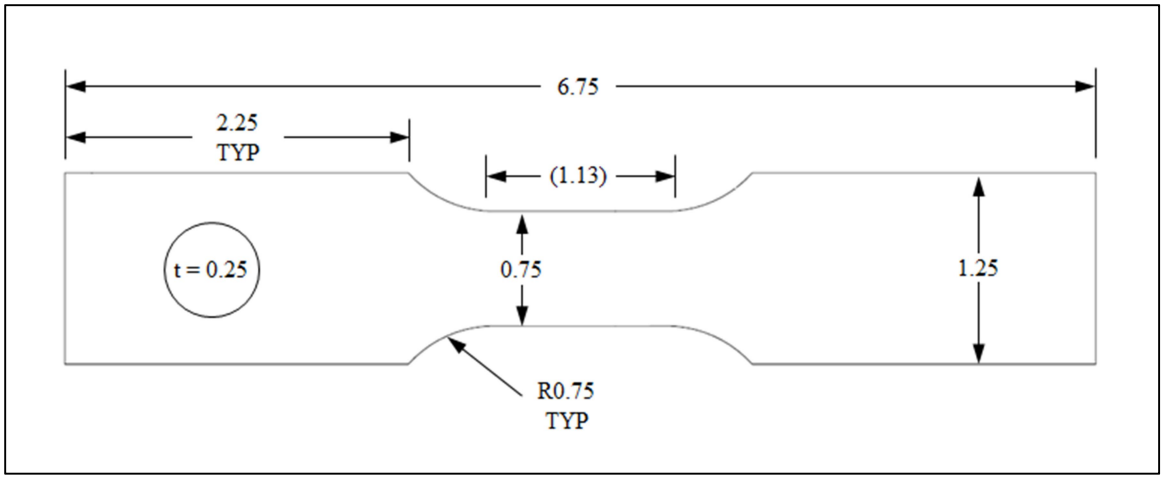

Figure 7 Modulus Specimen Geometry

end plane flatnesses were within the 0.0005 in/in recommendation for all but one specimen (specimen 7C), with a worst case flatness measurement of 0.0052 in (approximately 0.0006 in/in). However, parallel measurements between the opposing end faces averaged 0.0053 in (approximately 0.0006 in/in), with a worst case parallel measurement of 0.0103 in (approximately 0.0013 in/in, or 2.5 times the recommended allowance), also for specimen 7C. Due to the test program budget and schedule, final machining of the test fixtures was not performed and specimen final surface finish was not specified in the test plan. Despite test specimen quality being below the recommendations of ASTM International [17], the time and expense necessary for additional, more intricate machining, especially considering the nonstandard shape of the specimens, could not be justified. Overall, the test specimen quality was deemed acceptable by the testing organization.

Final preparation details for the bar and modulus specimens were not directed in the test plan and were primarily determined by the testing organization. Quality measurements were not provided for review and are therefore not discussed within this

report. The testing organization utilized ASTM standards E9 and E111 for general test guidance; its compliance with all necessary specimen preparation recommendations is assumed.

2.3.2 Surface Blends

Half of the aircraft skin specimens received a surface blend which was intended to simulate the cleanup and removal of corrosion, tool gouges, or other damage encountered during typical aircraft maintenance operations. See Figure 8 for an overview of the blend parameters and Table 3 for full blend details and dimensions for each specimen. In order to properly locate and size each blend, an electron discharge machining (EDM) notch was placed on the outer skin surface and centered on the test specimen within 0.100 in (see Appendix B for machining instructions). The EDM notch simulated a corrosion pit and established the proper depth for each blend. A circular or elliptical (depending on the specimen) surface blend was then cut to the full depth of the EDM notch. Standard maintenance and repair practices for corrosion removal [10] dictated the overall blend parameters. Blending was only performed on aircraft skin specimens, not bar specimens.

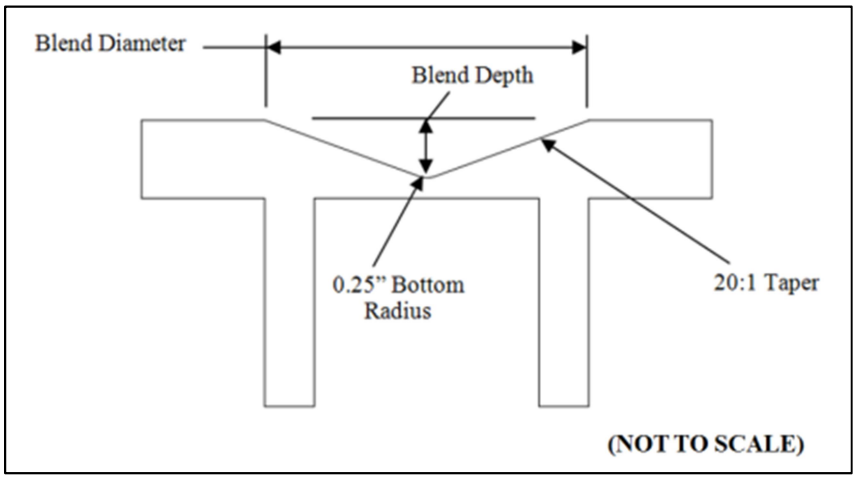

Figure 8 Blend Parameters

Table 3 Blend Dimensions

Specimen ID	Skin Thickness at Mid Span (in)	Blend Depth (in)	Blend Depth (% t_{skin})	Blend Diameter (in)
2B	0.1745	N/A	0%	N/A
2C	0.1735	0.08	46%	3.2
3B	0.1970	N/A	0%	N/A
3C	0.2010	0.08	40%	3.2
5B	0.1960	N/A	0%	N/A
5C	0.1990	0.14	70%	2.8 / 5.6[3]
7B	0.2010	N/A	0%	N/A
7C	0.2045	0.11	54%	2.2 / 4.4[3]
8B[4]	0.1800	N/A	0%	N/A
8C[4]	0.1750	0.08	46%	3.2

[3] Specimens 5C and 7C were blended with a 20:1 taper in the axial direction and a 10:1 taper in the transverse direction.

[4] Fuel vent holes were plugged on specimens 8B and 8C.

As noted in Table 3, specimens 5C and 7C utilize a modified blend profile due to the depths, and therefore, widths of the blends. The intent of this modification was to keep the entire blend profile within the width of the vertical stringer flanges, which could not be accomplished with a 20:1 taper ratio in the transverse direction. This, in turn, was intended to prevent unnecessary weakening of the corner sections and, hopefully, force initial instability to occur in the skin at the center of the blend rather than at a weakened skin/stringer "corner."

2.3.3 Plugging Fuel Vent Holes

The final processing requirement involved plugging open fuel vent holes common to the vertical stringer flanges. Each aircraft skin specimen includes two vent holes: one per vertical stringer flange. The vent holes are located near the stringer/skin interfaces, but do not cut into the corner radii.

The initial test plan did not specify plugging of any fuel vent holes, primarily due to an assumption that the holes would negligibly impact the overall specimen buckling load. While the quantitative impact of these holes is examined in greater detail in later chapters of this report, visual examination of the initial test specimens revealed an interesting trend: buckling in some cases occurred at the vent holes rather than at the center of the blend (see Figure 9 for an example). The initial conclusion was that, in some cases, the open holes had a greater effect on buckling load than did the presence of a surface blend.

The decision to plug these holes only for the final test specimens (8B and 8C) was not made lightly. While the test results from these final specimens could definitively suppress the effects of an open hole specimen configuration, the process would introduce

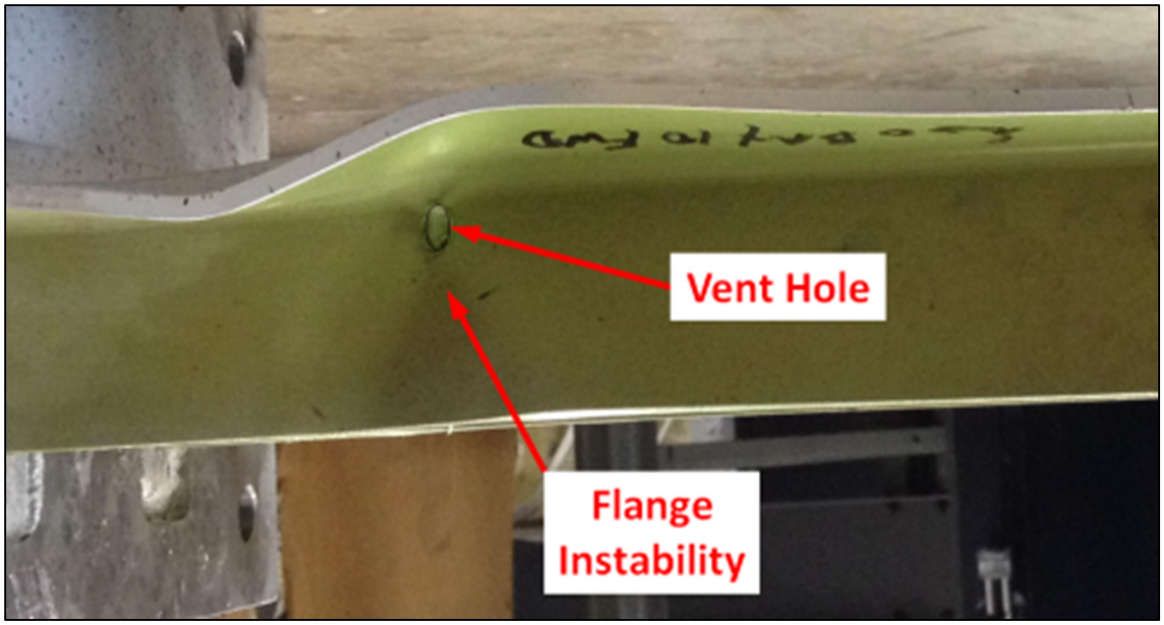

Figure 9 Buckling at a Fuel Vent Hole

yet another variable to consider during post-test data analysis. Ultimately, however, the usefulness of gathering plugged hole data offset the risks of introducing an additional test variable (at least in the opinion of this author). Specifically, the plugged hole data could be used to evaluate whether blending decreased the buckling resistance of the test specimens below that which had already been "established" by the presence of fuel vent holes. The presence of an additional test variable was also hoped to help justify additional testing, though funding for such an effort was ultimately not provided.

Decisions on the ideal plug material and type were necessary to ensure that plugs would have the same elastic modulus as the test specimen and would completely fill the vent hole. Aluminum rivets provided the simplest solution and the most complete hole fill, but were ultimately rejected in favor of press-fit aluminum plugs. The deciding advantages of press-fit plugs were the ease of installation, lack of a rivet head and tail, and a reduction in the residual stress effects typically induced by rivet installation [18].

2.4 Test Equipment

2.4.1 Compression Specimen Fixturing

Two sets of end cap fixtures were designed for the test specimens: one set for the aircraft skin specimens and one set for the bar specimens. The purpose of each fixture was to protect the load frame crossheads by distributing contact loads across a larger surface area, as well as to provide end restraint for the test specimens. Fixtures were manufactured from an unspecified steel alloy and filled with Wood's metal as a potting compound during testing. Dimensions for each of the two specimen fixtures are shown in Figure 10 and Figure 11. Due to the lateral stability inherent to the specimen shape (see section 2.2.1), lateral edge support was deemed unnecessary for this experiment.

2.4.2 Specimen Potting

Prior to testing, the loaded ends of each compression specimen were centered within an appropriate test fixture (see Figure 10 and Figure 11) and potted with Wood's metal. The purpose of potting the test specimens was to provide end restraint without the need to design a complex clamping mechanism for the unusual specimen cross section. Wood's metal was chosen as a potting compound over more common epoxies due to uncertainty regarding the potential for epoxies to crack at high loads, as well as the difficulty or outright inability to reuse test fixtures once filled with epoxy and allowed to cure.

Wood's metal is a fusible (low melting temperature) alloy comprised of 50% bismuth, 25% lead, 12.5% cadmium, and 12.5% tin [19]. In addition to the aforementioned advantages of Wood's metal over epoxy, Wood's metal is known for its ease of use as a potting material primarily due to its low (158 °F) melting temperature

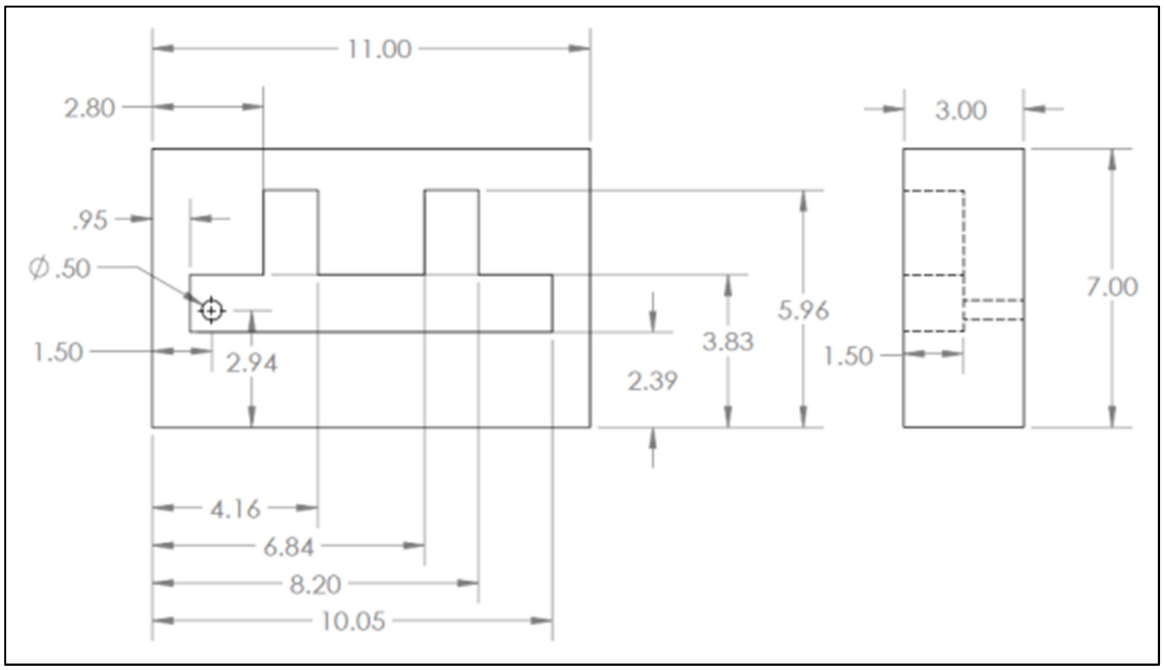

Figure 10 Skin Specimen Fixture Dimensions

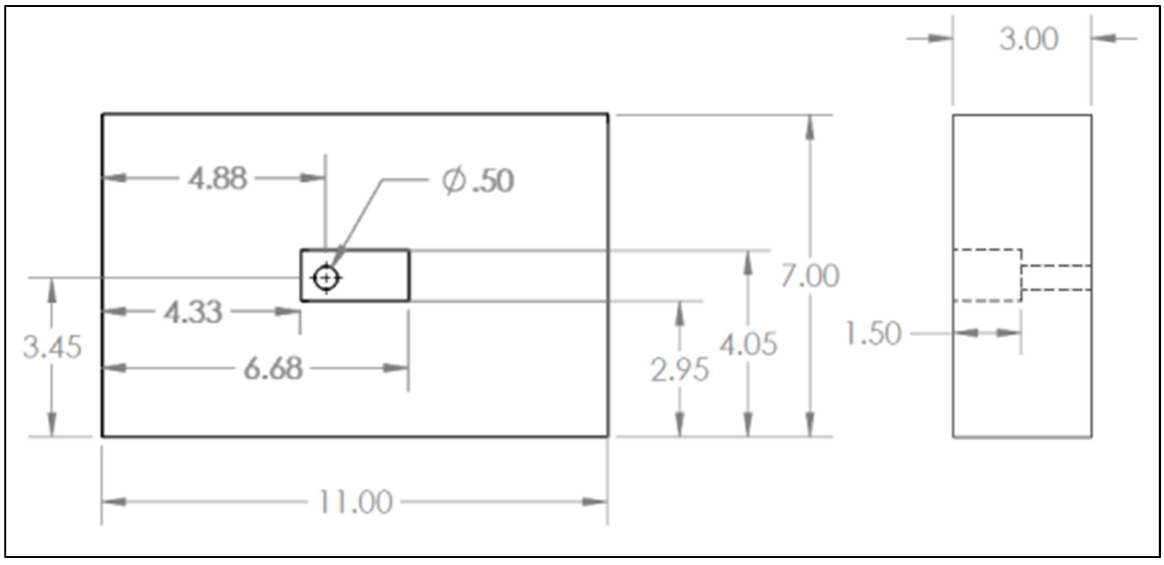

Figure 11 Bar Specimen Fixture Dimensions

and consistency of mechanical properties both between melt-remelt cycles and irrespective of strain rate [20]. Figure 12 details the loaded end of a post-test specimen as potted into a test fixture. The ability of the potting material to conform to the specimen cross section is clearly shown, as is the ability of the potting material to provide end restraint for the specimen (as indicated by the buckled flanges returning to an axial orientation near the fixturing).

The primary disadvantage of Wood's metal is its low elastic modulus compared to the steel test fixtures, and even compared to the aluminum test specimens [16], [20]. In other words, Wood's metal can only provide an elastic end restraint, rather than a true "fully clamped" condition. Hence, the inclusion of bar testing (test phase 2) as an attempt to characterize this elastic restraint.

Figure 12 Specimen Potting

2.4.3 Load Frames

Preliminary analysis (not detailed in this report) highlighted the need for a load frame with a 300 kip capacity and a 30 in minimum clearance in the loading direction. The load frame selected for use was a Tinius Olsen Super “L” Universal Testing Machine (UTM). The Super “L” is a four column, hydraulically actuated UTM designed for vertical load application [21]. The load frame type utilized for modulus testing was not provided by the test organization.

2.4.4 Instrumentation

Primary load data for the compression tests is based on test fixture hydraulic pressure as measured by a Sensotec FPG pressure transducer (part number 060-E641-03). Backup load data were obtained from a second pressure transducer wired directly to the test frame controller (Tinius Olsen Model CMH 496). The pressure transducers were independently calibrated and gave results within approximately 1% of each other. A pair of Ametek Rayelco PT-420-2 linear motion transducers (string pots) mounted to opposing corners of the test fixtures provided deflection data. Due to the out-of-plane deflection and nonlinear behavior inherent to a buckled specimen, strain gages were assumed to be a poor choice for determining total specimen deflection and were therefore not utilized as a primary data source for compression tests (though some early specimens utilized strain gage placements for secondary data evaluation).

The original test plan called for painting (“speckling”) the test specimens for use with digital image correlation (DIC). Unfortunately, however, the time and expense necessary for specimen preparation, DIC camera setup, and post-test data processing were greater than this test program could support. Recording of internal stresses within

the test specimens was ultimately deemed to be of low importance to the goals of this experiment and the effort was abandoned after three specimens.

Modulus tests utilized a pair of strain gages mounted near the center of each modulus specimen on opposite sides. An extensometer provided backup data. Modulus tests were performed away from the supervision of this author, and the test organization did not provide manufacturer or model information for the instrumentation.

CHAPTER 3

TEST PROCEDURES AND RESULTS

3.1 ASTM Testing Standards

The experimental portions of this study were modeled after ASTM standards E9 and E111 for baseline guidance of compression and modulus testing, respectively. While reasonable attempts were made to implement all relevant details of the ASTM standards, the overall goals of this experiment neither require nor allow for absolute compliance (the most prominent example is this experiment's goal of intentionally inducing specimen instability, a condition which standard E9 seeks to prevent [17]). Therefore, it is noted that the ASTM standards were primarily utilized for general test guidance rather than step-by-step instruction.

3.2 Test Procedures

3.2.1 Compression Testing

After potting each end of a specimen into a test fixture, the Wood's metal potting material was allowed to cool and solidify for a minimum of two hours. Final instrumentation checks and load testing were directed as follows.

1) Place the fixtured specimen vertically into the load frame and apply a slight load to secure the specimen.
2) Install two stringpots onto the specimen fixturing at opposite corners.

3) Ensure all instrumentation is connected to the data acquisition system and the data acquisition system is recording.
4) Load the test specimen using deflection control at a constant rate of 0.1 in/min (approximately 0.005 in/in-min [17]).
5) Continue loading the test specimen while monitoring real time data acquisition system displays (specifically, load vs. time).
6) Final failure is assumed to have occurred once the load curve peaks and the slope becomes negative. At this point, stop crosshead movement, save all test data, and remove the test specimen from the load frame.

Figure 13 shows a fixtured test specimen in the load frame; buckling of the skin is evident. The data acquisition system recorded a total of three data channels (deflection 1, deflection 2, and load) at a sampling rate of 100 Hz. Although the data acquisition system technically captured load frame hydraulic pressure (rather than direct force via a load cell), a pressure-to-load algorithm was applied to the data during initial processing. Therefore, raw pressure data were not recorded or saved, and all data acquisition system outputs displayed load as a primary data channel. Figure 14 shows a sample screenshot from the data acquisition system (two channels deflection vs. time on the left, one channel load vs. time on the right). Final failure (peak load) is easily visible in Figure 14.

The load frame controller also displayed system load, but did not record discrete data points. Therefore, the only usable data from this system was the maximum (peak) load, which was recorded manually and used as a backup data source. Figure 15 details the load frame controller display.

Figure 13 Buckled Specimen in Load Frame

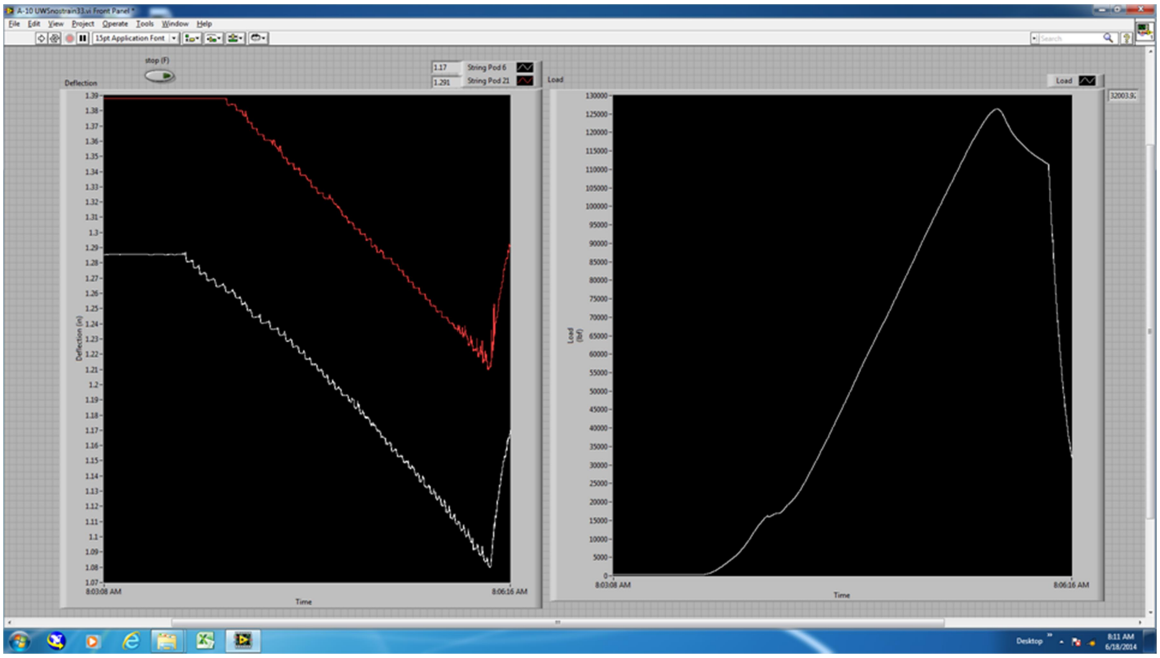

Figure 14 Data Acquisition System Display (Typical Specimen)

Figure 15 Controller Display

3.2.2 Modulus Testing

Procedures for modulus testing were largely the same as those for compression testing, with the following exceptions.

1) Coupons were clamped to the load frame crossheads with grips rather than potted into test fixtures.
2) Crosshead speed was reduced from 0.1 in/min to 0.005 in/min.
3) Multiple load cycles were performed on each coupon rather than a single load application to failure.

With regard to multiple load cycles, each coupon was loaded three times to an equivalent stress of approximately half the expected proportional limit [22]. Coupons were loaded to 35 ksi, then the crosshead was returned to the "zero" position. Coupons were then loaded to 35 ksi a second time, and the crosshead returned to zero again. On the third load application, coupons were loaded to 35 ksi, but load ramping continued uninterrupted until material yielding occurred. This loading profile can be seen graphically in Figure 16. Five data channels were recorded for the modulus tests: load, crosshead position, extensometer, strain 1, and strain 2. A single strain gage was placed on each side of the test coupon (one front and one back) at its geometric center.

3.3 Test Results

With the exception of some lost and erroneous data (discussed in further detail in section 3.3.2 and section 3.3.3), there are no major test anomalies to report. Instability occurred near the predicted loads and specimen material properties are determined in accordance with standard test methods. See Table 4 for stability test results and Table 5 for modulus test results. Aircraft compression specimens are identified by a single

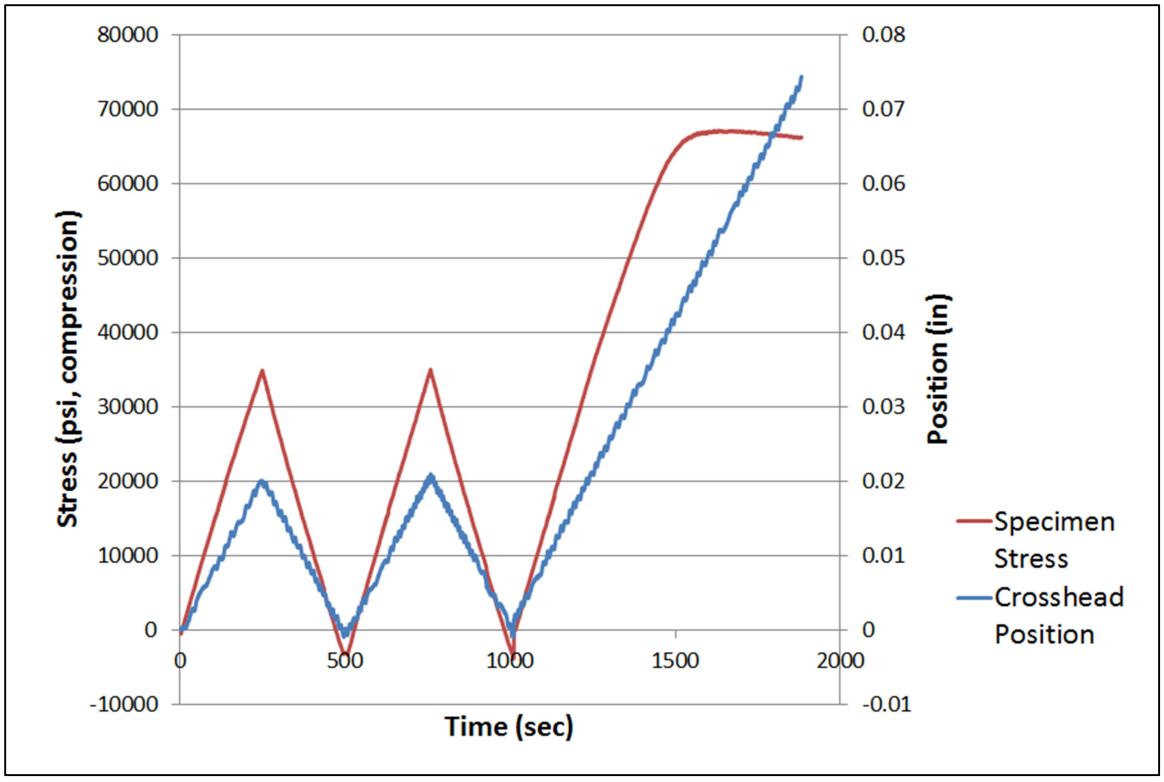

Figure 16 Modulus Test Loading Profile (Typical Specimen)

number and letter (e.g., 2B). “B” indicates an unblended specimen and “C” indicates a blended specimen (while somewhat counterintuitive, this numbering scheme was implemented during the initial machining of test specimens and retained for all later test and reporting phases). Bar specimens are identified by the code “FP” (due to initial consideration as “flat plate” specimens, which, in the opinion of this author, gives an erroneous conception of the test intent). Modulus specimens are identified as follows: “AFTM” for specimens from the aft skin panel, “FWDM” for specimens from the forward skin panel, and “FPM” for bar specimen (i.e., flat plate) material stock.

Table 4 Compression Test Results

Specimen ID	Column Length (in)	Blend Depth (in)	Max Load (Primary) (lb)	Max Load (Backup) (lb)	Percent Difference
2B	24.10	N/A	134394	133090	0.98%
2C	24.27	0.08	117236	116119	0.96%
3B	21.33	N/A	179901	178292	0.90%
3C	21.24	0.08	--	176784	N/A
5B	21.77	N/A	199184	197090	1.06%
5C	22.02	0.14	179741	--	N/A
7B	21.60	N/A	158443	156653	1.14%
7C	21.85	0.11	153682	--	N/A
8B	21.65	N/A	140185	--	N/A
8C	21.66	0.08	126354	--	N/A
FP-1	21.79	N/A	14996	--	N/A
FP-2	21.66	N/A	15352	--	N/A
FP-3	21.48	N/A	15720	--	N/A

Table 5 Modulus Test Results

Specimen ID	Modulus Data			$F_{cy,\ 0.2\%\ offset}$ (psi)
	E_c (psi)	r^2	V_1	
AFTM-1	1.067E+07	0.99994	0.022%	66837
AFTM-2	1.076E+07	0.99993	0.026%	70335
FWDM-1	1.062E+07	0.99995	0.023%	62362
FWDM-2	1.090E+07	0.99993	0.027%	63640
FPM-1	1.102E+07	0.99993	0.026%	65792
FPM-2	1.106E+07	0.99992	0.027%	66180

3.3.1 Data Interpretation

Interpretation of compression test data is relatively straightforward, with maximum load obtained during the test being the principal data of interest. Primary load data were recorded by a standalone data acquisition system, while backup data were provided by the load frame controller. The data acquisition system recorded discrete data points at 100 Hz, while the controller (backup data) displayed maximum load but did not store or export discrete data points.

Modulus test data require more in-depth analysis in order to obtain usable results. Young's modulus for compression (E_c) is determined by the method of least squares as described in standard E111. The coefficient of determination (r^2) and coefficient of variation (V_1) are provided in Table 5 for reference purposes, but are not utilized for any experimental purposes within this study. Calculations for each of these values are as follows in Equations (1), (2), and (3) [22],

$$E_c = \frac{\Sigma(XY) - K\bar{X}\bar{Y}}{\Sigma X^2 - K\bar{X}^2} \tag{1}$$

$$r^2 = \left[\left(\Sigma(XY) - \frac{\Sigma X * \Sigma Y}{K}\right)^2\right] \Big/ \left[\left(\Sigma(X^2) - \frac{(\Sigma X)^2}{K}\right)\left(\Sigma(Y^2) - \frac{(\Sigma Y)^2}{K}\right)\right] \tag{2}$$

$$V_1 = \sqrt{\frac{(1/r^2) - 1}{K - 2}} * 100\% \tag{3}$$

where

X	applied axial stress;
Y	corresponding strain;
$\bar{X}$ and $\bar{Y}$	average of all X values and Y values, respectively;
K	number of X, Y data pairs;

Σ sum from 1 to K.

The calculated modulus and associated coefficients for each specimen represent average values from multiple datasets. For each modulus specimen, the relevant test data are broken up into a series of ten datasets consisting of three load cycles (see Figure 16) using two strain gage data channels. (Extensometer data are neglected from modulus calculations – see section 3.3.3 for additional details.) E_c, r^2, and V_1 are calculated for each of these ten datasets. The results shown in Table 5 are the averages of the ten individual results for each specimen. In order to prevent the possibility of skewed data near the beginning and end of each load cycle, only the data between approximately 2 ksi and 33 ksi are used for modulus calculations (with 0 ksi and 35 ksi being the approximate minimum and maximum stresses for each load cycle).

Each specimen experienced only one load application beyond the material yield stress (F_{cy}). Therefore, the yield stress data shown in Table 5 are simply the average of the results for each of three data channels (extensometer, strain gage 1, and strain gage 2), except where otherwise noted in section 3.3.3. A standard offset of 0.002 in/in (0.2%) [17] is used for determination of the yield point. This method is shown graphically in Figure 17.

3.3.2 Lost Data

Backup load data for the compression tests were not consistently recorded (as shown via blank cells in Table 4). Fortunately, these backup data are only required for one test: specimen 3C. At a load of approximately 40 kips on this specimen, the primary load channel stopped recording and did not resume recording until the load dropped back below 40 kips again. The cause of this data loss is unknown.

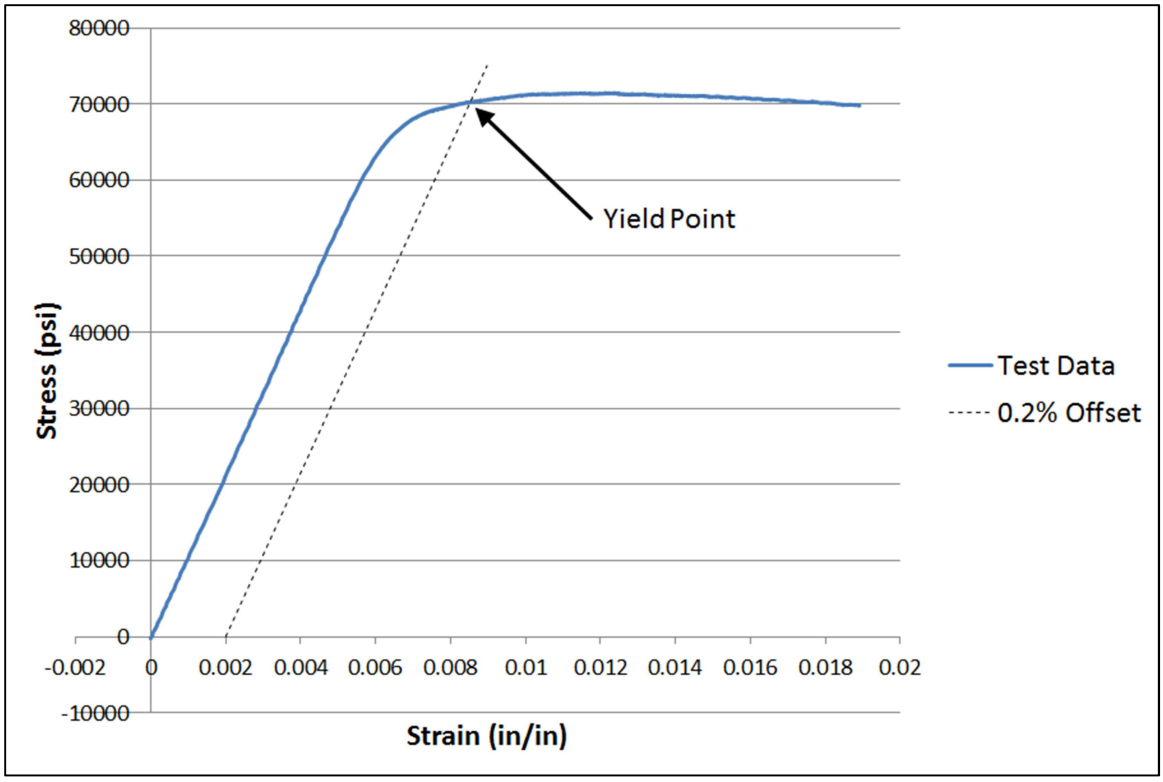

Figure 17 0.2% Offset Yield Stress (Typical Specimen)

In order to allow for consistent data analysis in later sections of this report, it is necessary to adjust the backup data recorded for specimen 3C. Both primary and backup load data exist for five of the compression specimens. These results show an average difference between the primary and backup load channels of 1.01%. Therefore, a 1.01% adjustment is applied to the backup data for specimen 3C. This correction is shown in tabular form for ease of reference in Table 6.

Table 6 Specimen 3C Load Correction

Specimen ID	Max Load (lb)	Correction Factor	Adjusted Load (lb)
3C	176784	+1.01%	178570

3.3.3 Erroneous Data

As previously mentioned, extensometer data are neglected from all modulus calculations. For most specimens, the two strain gage channels correlate well with one another. Stress vs. strain slopes for extensometer data, however, are approximately 5% lower (on average) than strain gage data. This variation is assumed to be significant enough to warrant filtering the data, relying instead on only strain gage data. An example of this phenomenon is shown in Figure 18. (Note that data from the two strain gage channels overlap sufficiently so as to be indistinguishable within the figure.)

An additional dataset is neglected from specimen AFTM-2. In this case, one of the strain gage channels recorded a stress vs. strain slope which was over 20% greater than average slopes from similar specimens (two strain gage channels from specimen AFTM-1 and the remaining strain gage channel from AFTM-2). Although the cause of this anomaly is unknown, it is likely the result of a misaligned strain gage. A sample of stress vs. strain data for this specimen is shown in Figure 19 for visual reference. Specimen AFTM-2 is the only specimen which utilized a single data channel for modulus calculations.

In all but two tests (specimens FPM-1 and FPM-2), instability of the modulus coupons occurred prior to reaching the compressive yield stress. An example is shown visually in Figure 20. In such cases, one of the strain curves begins to reverse before crossing the 0.2% offset line. Therefore, the data from that strain gage cannot be used for determination of the material yield stress. Unlike in the modulus calculations, however, extensometer data are considered appropriate for yield stress calculations. Discrepancies between extensometer curve slopes and strain gage curve slopes are irrelevant because a

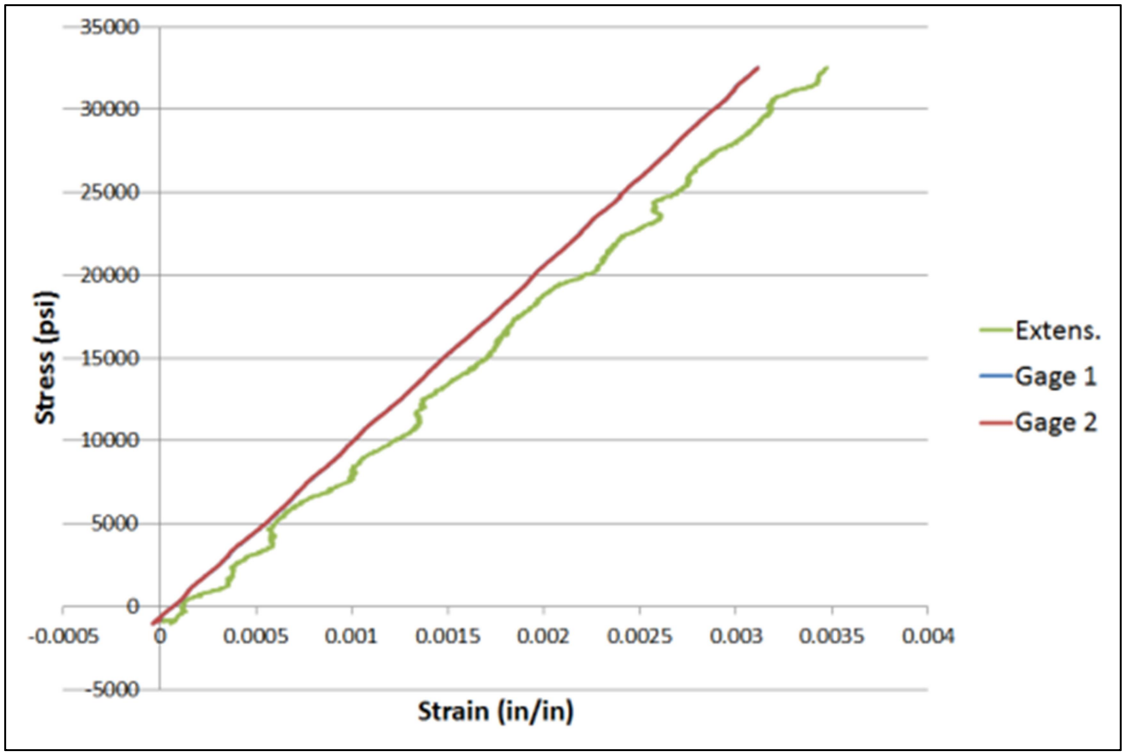

Figure 18 Erroneous Extensometer Data (Typical Specimen)

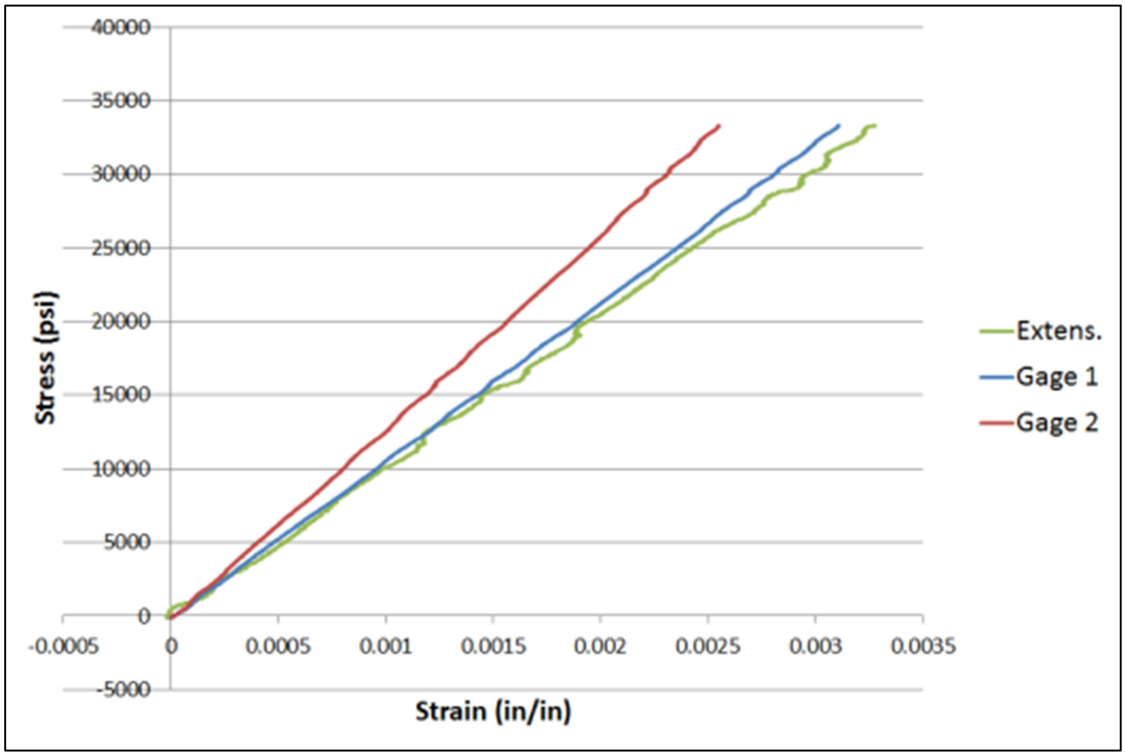

Figure 19 Erroneous Strain Gage Data (Specimen AFTM-2)

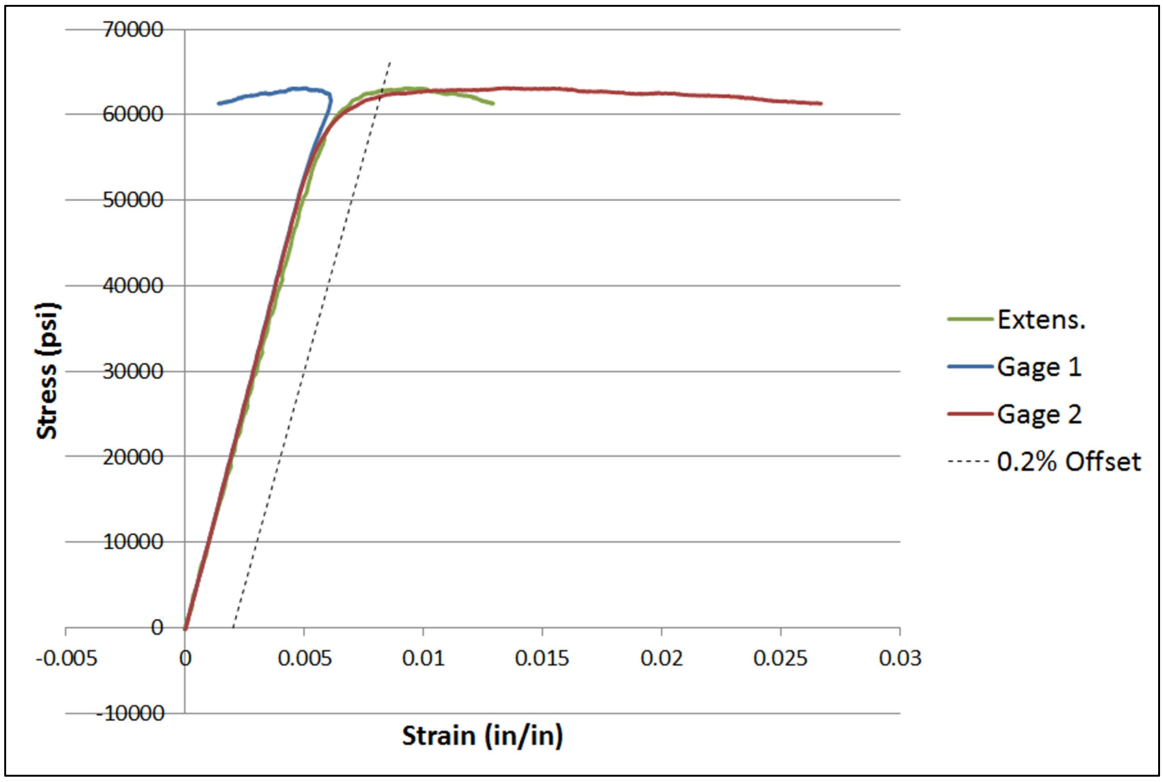

Figure 20 Modulus Specimen Instability (Typical Specimen)

separate 0.2% offset line can be used for each data channel. On average, yield stress results from extensometer data and strain gage data are within 1% of each other. However, an unknown error resulted in unusable extensometer data for specimen FPM-2. Yield stress for this specimen is based on the two strain gage data channels.

CHAPTER 4

ANALYSIS AND DISCUSSION

4.1 Material Properties

4.1.1 Comparisons Against Published Data

Common buckling equations rely upon certain material properties, including the compressive modulus and material yield stress (E_c and F_{cy}, respectively) [11], [17]. For reference purposes, this experiment's material property testing results (Table 7) are compared to published material property values (Table 8). The published values shown in Table 8 represent the values which are typically used in aircraft structural design/analysis; both the grain direction and the statistical basis for evaluation are important variables. Longitudinal (L-direction) and B-basis values are shown. It is generally understood that the nature of extrusion processing gives a longitudinal grain in the axial direction (i.e., the L-direction grain orientation is parallel to the direction of primary loading). For the statistical basis, B-basis values are typically selected for analysis of multiple loadpath designs, a criterion which is typically met by designs incorporating integrally stiffened skin panels [23]. B-basis is defined as "at least 90 percent of the population of values is expected to equal or exceed the statistically calculated mechanical property value, with a confidence of 95 percent" [16]. Grain orientation is unknown for the bar specimens, so the most conservative grain direction is assumed. Furthermore, only S-basis values are available for the bar material. S-basis is

Table 7 Average Material Properties

Specimen ID	E_c (psi)	F_{cy} (psi)	Material Source	Material Type	Average E_c (psi)	Average F_{cy} (psi)
	(ref. Table 5)					
AFTM-1	1.067E+07	66837	Aft Skin Panel	7075-T76511 Extrusion	1.072E+07	68586
AFTM-2	1.076E+07	70335				
FWDM-1	1.062E+07	62362	Fwd Skin Panel	7075-T76511 Extrusion	1.076E+07	63001
FWDM-2	1.090E+07	63640				
FPM-1	1.102E+07	65792	Bar Specimens	7075-T7651 Plate	1.104E+07	65986
FPM-2	1.106E+07	66180				

Table 8 Material Property Comparison

Material Source	Material Type	$E_{c,\ published}$ (psi) [16]	$E_{c,\ test}$ (psi)	Percent Difference	$F_{cy,\ published}$ (psi) [16]	$F_{cy,\ test}$ (psi)	Percent Difference
Aft Skin Panel	7075-T76511 Extrusion	1.070E+07	1.072E+07	0.17%	67000	68586	2.37%
Fwd Skin Panel	7075-T76511 Extrusion	1.070E+07	1.076E+07	0.54%	67000	63001	-5.97%
Bar Specimens	7075-T7651 Plate	1.060E+07	1.104E+07	4.18%	59000	65986	11.84%

defined as “the specification minimum value specified by the governing industry specification” [16].

Table 8 reveals some unexpected anomalies in the material property test results. First is the 4.18% increase in compressive modulus over published values for 7075-T7651 aluminum plate, especially considering the <1% increase for both of the aircraft skin materials. Although discussion on the consistency of Young’s modulus in aluminum is outside the scope of this report, it is noted that individual test results for the bar specimens are highly consistent. The standard deviation in modulus calculations across two test specimens, each with two strain gages and five loads/unloads (20 individual results), is only 0.6% of the average; the total range (maximum result minus minimum result) is less than 2%. Thus, this anomaly does not appear to be due to errors in data interpretation and/or strain gage placement and it is assumed that the test results accurately represent the state of the material.

The second anomaly is the 11.84% increase in compressive yield stress over published values, also for the 7075-T7651 aluminum plate. Although this is a significant increase considering the importance of this material property to engineering analysis, closer examination reveals that the result is not surprising. As previously mentioned, the published value represents the S-basis, or the minimum specification allowance [16]. It follows, then, that any given sample of 7075-T7651 should meet or exceed the published value. Additionally, the reported value is the minimum of all possible grain orientations. If the test specimens were confirmed to be cut to length in the long-transverse (LT) grain direction, for example, the variance between the published value and test result would be reduced to 4.74%. Indeed, the material certification for the bar specimen material

includes material property test results (tensile ultimate and tensile yield stresses) in the range of 7%-10% greater than published values (see Appendix C for the material certification test report). Thus, the test results documented in this report appear to be consistent with the test results documented on the material certification report.

Finally, perhaps the most unexpected result is the 5.97% *decrease* in compressive yield stress as compared to published values for the forward skin panel's 7075-T76511 aluminum extrusion. Test results are 5.97% lower than published B-basis values and 3.08% lower than A-basis values (representing the lower 90^{th} percentile and lower 99^{th} percentile, respectively, both with 95% confidence) [16]. Thus, the statistical likelihood of any given sample of 7075-T76511 extrusion having a lower material strength than the published value is quite low. A review of the consistency of test results across two test specimens, each with strain gage and extensometer data channels (four individual results), shows a standard deviation of only 1.3% of the average and a total range of 3.7%. While not as consistent as the bar specimen test results, the total range of test values is still less than the difference between the test result and the published B-basis value (3.7% vs. 5.97%), and not a single test result exceeds even the A-basis value (65,000 psi [16]). As with the previous anomalies, the variation in results does not appear to be due to errors in data interpretation and/or strain gage placement. Potential causes for such low material strength can only be speculated upon, but residual stresses due to peening of the panel surfaces at manufacture (for the purposes of shape forming and improved fatigue life) may have played a role.

4.1.2 Stress-Strain Curve Manipulation

In order to present the data in as smooth and consistent a form as possible, a series of modifications and manipulations are performed on the material property test results. This step is especially important for use in later finite element analysis setup. The Ramberg-Osgood relationship is deemed to be both a simple and effective means to convert raw stress/strain curves into smooth profiles which can be easily compared against published data. Only two additional data points are needed from each raw stress/strain curve: the 70% and 85% secant yield stresses (commonly referred to as $F_{0.7}$ and $F_{0.85}$). The Ramberg-Osgood factor (n) is found via the following equation [24]:

$$n = 1 + \frac{\ln(17/7)}{\ln(F_{0.7}/F_{0.85})} \tag{4}$$

Using this factor, the tangent modulus (E_t) at any given stress can be found [24]:

$$E_t = \frac{E}{1 + \frac{3}{7} n \left(\frac{F}{F_{0.7}}\right)^{n-1}} \tag{5}$$

With the tangent modulus known at any given stress, a simple manipulation of the point-slope equation of a line is used to back calculate corresponding strains:

$$m = \frac{y_2 - y_1}{x_2 - x_1}$$

which can be rewritten as

$$x_2 - x_1 = \frac{y_2 - y_1}{m}$$

or

$$\varepsilon_2 - \varepsilon_1 = \frac{F_2 - F_1}{E_t} \tag{6}$$

One final modification of the data is necessary. ANSYS recommends converting

engineering stress and strain values to true stress and strain when nonlinear material response is assumed. The following equations are utilized for conversion of engineering stress/strain to true stress/strain (though it is noted that without accurate coupon cross-sectional area measurements, the results are only approximations) [25]:

$$\sigma_{true} = \sigma_{eng}(1 + \varepsilon_{eng}) \tag{7}$$

$$\varepsilon_{true} = \ln(1 + \varepsilon_{eng}) \tag{8}$$

See Table 9 and Table 10 for the results of Equations (4) through (8). The displayed values for $F_{0.7}$ and $F_{0.85}$ are based on average results from all applicable test data (similar to the method used to calculate F_{cy} – see section 3.3.1). Note, however, that the stress and strain values shown in Table 9 and Table 10 were calculated prior to rounding $F_{0.7}$ and $F_{0.85}$ to whole numbers. Slight variations may therefore be expected during attempts to verify and/or duplicate the full results of the tables. For reference purposes, graphical comparisons between test data, Ramberg-Osgood modifications, and true stress/strain approximations for the aft and forward panels are shown in Figure 21 and Figure 22, respectively.

4.2 Finite Element Analysis Setup and Validation

This study utilizes finite element analysis (FEA) as a means to examine the effects of various blend shapes and sizes on overall compressive load carrying capability. FEA results were first validated against physical testing before expanding the scope of the simulations to a wider range of blend geometries. All FEA simulations are performed using ANSYS version 16.2.

Table 9 Aft Panel Stress/Strain Data

E_c (psi)	F_{cy} (psi)	$F_{0.7}$ (psi)	$F_{0.85}$ (psi)	n
10720000 (ref. Table 8)	68586 (ref. Table 8)	69023	67219	34.51
F (psi)	**E_t (psi)**	**ε (in/in)**	**F_{true} (psi)**	**ε_{true} (in/in)**
0	10720000	0.0000	0	0.0000
3000	10720000	0.0003	3001	0.0003
6000	10720000	0.0006	6003	0.0006
9000	10720000	0.0008	9008	0.0008
12000	10720000	0.0011	12013	0.0011
15000	10720000	0.0014	15021	0.0014
18000	10720000	0.0017	18030	0.0017
21000	10720000	0.0020	21041	0.0020
24000	10720000	0.0022	24054	0.0022
27000	10720000	0.0025	27068	0.0025
30000	10720000	0.0028	30084	0.0028
33000	10720000	0.0031	33102	0.0031
36000	10720000	0.0034	36121	0.0034
39000	10719999	0.0036	39142	0.0036
42000	10719991	0.0039	42165	0.0039
45000	10719906	0.0042	45189	0.0042
48000	10719180	0.0045	48215	0.0045
51000	10713750	0.0048	51243	0.0047
54000	10677706	0.0050	54272	0.0050
57000	10466229	0.0053	57304	0.0053
60000	9442864	0.0056	60339	0.0056
63000	6329249	0.0061	63385	0.0061
66000	2494397	0.0073	66483	0.0073
69000	686047	0.0117	69807	0.0116
72000	173230	0.0290	74089	0.0286
75000	44647	0.0962	82215	0.0919
78000	12032	0.3455	104952	0.2968

Table 10 Forward Panel Stress/Strain Data

E_c (psi)	F_{cy} (psi)	$F_{0.7}$ (psi)	$F_{0.85}$ (psi)	n
10760000 (ref. Table 8)	63001 (ref. Table 8)	62853	60870	28.68
F (psi)	**E_t (psi)**	**ε (in/in)**	**F_{true} (psi)**	**ε_{true} (in/in)**
0	10760000	0.0000	0	0.0000
3000	10760000	0.0003	3001	0.0003
6000	10760000	0.0006	6003	0.0006
9000	10760000	0.0008	9008	0.0008
12000	10760000	0.0011	12013	0.0011
15000	10760000	0.0014	15021	0.0014
18000	10760000	0.0017	18030	0.0017
21000	10760000	0.0020	21041	0.0019
24000	10760000	0.0022	24054	0.0022
27000	10760000	0.0025	27068	0.0025
30000	10760000	0.0028	30084	0.0028
33000	10759998	0.0031	33101	0.0031
36000	10759974	0.0033	36120	0.0033
39000	10759758	0.0036	39141	0.0036
42000	10758115	0.0039	42164	0.0039
45000	10747290	0.0042	45188	0.0042
48000	10684586	0.0045	48214	0.0045
51000	10368096	0.0048	51242	0.0047
54000	9088554	0.0051	54274	0.0051
57000	5907546	0.0056	57319	0.0056
60000	2446821	0.0068	60409	0.0068
63000	762446	0.0108	63677	0.0107
66000	221745	0.0243	67603	0.0240
69000	65746	0.0699	73824	0.0676
72000	20328	0.2175	87659	0.1968
75000	6575	0.6737	125531	0.5151
78000	2221	2.0243	235896	1.1067

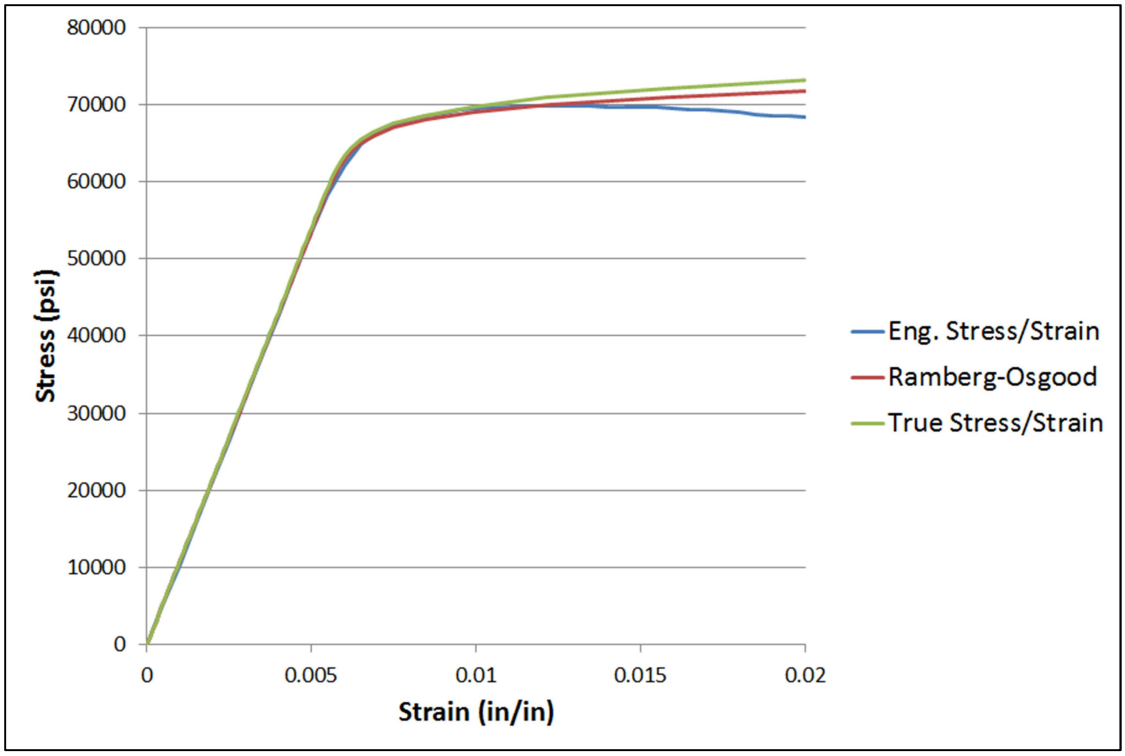

Figure 21 Aft Panel Stress/Strain Curves

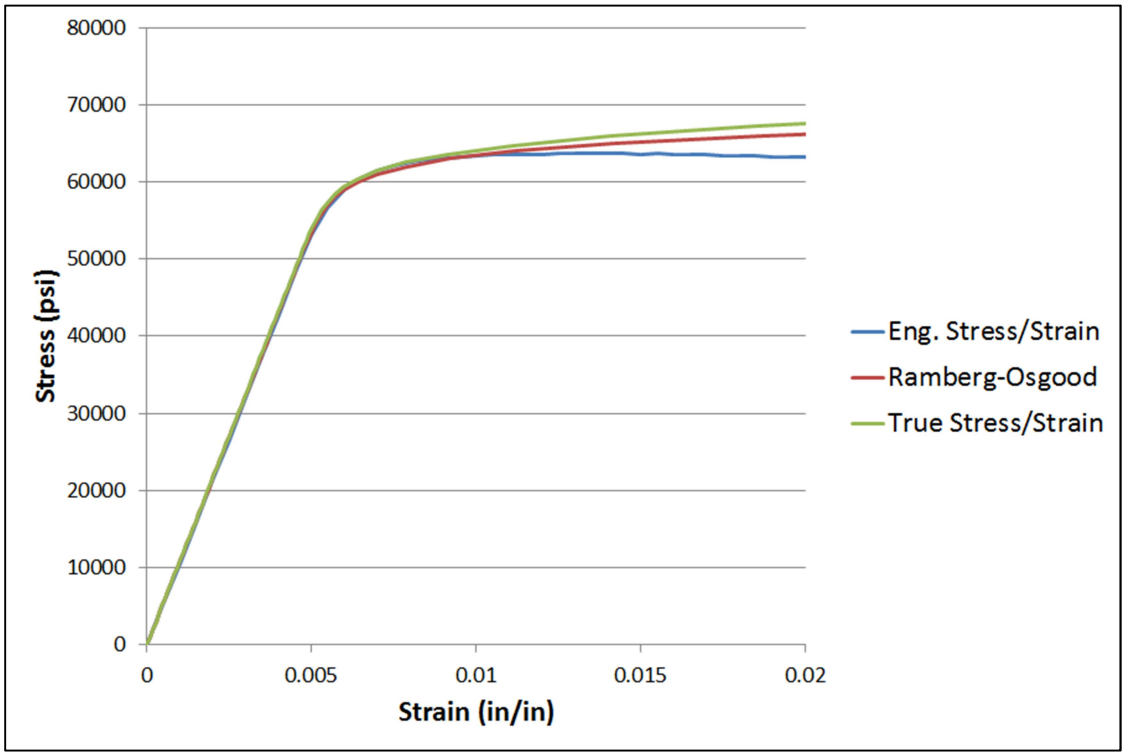

Figure 22 Forward Panel Stress/Strain Curves

4.2.1 FEA Setup and Methodology

Preliminary analysis of both simulated and real-world test results revealed significant departures from pure linear-elastic behavior. Therefore, the primary findings of this study are based on nonlinear simulation methods. Linear (i.e., eigenvalue) buckling analysis is not explored or detailed within this report.

FEA models duplicate the physical specimen measurements and material property test results to the maximum extent possible. All simulations utilize the "Static Structural" utility within ANSYS Workbench. Individual data modules are setup as shown below (default properties can be assumed when not specifically detailed herein).

1) "Engineering Data." The Isotropic Elasticity and Multilinear Isotropic Hardening properties are utilized in order to simulate nonlinear material behavior as follows:
    a) isotropic elasticity: i) defined by: Young's Modulus (E_c, per Table 9 and Table 10); ii) Poisson's Ratio = 0.33 [16];
    b) multilinear isotropic hardening: tabular data (per Table 9 and Table 10, true stress and true strain utilized [25]).
2) "Geometry." 3D solid models for each specimen were created in Solidworks and imported into ANSYS. Model geometry is as shown in Table 1 and Appendix A. Blend dimensions are per Figure 8 and Table 3. Due to the difficulty in accurately modeling an elliptical blend with a radiused base, all blends are idealized as a cone (i.e., taper to a single point rather than a radiused base). This idealization is shown graphically in Figure 23. Additionally, all FEA models include a 0.25 in fillet radius at the

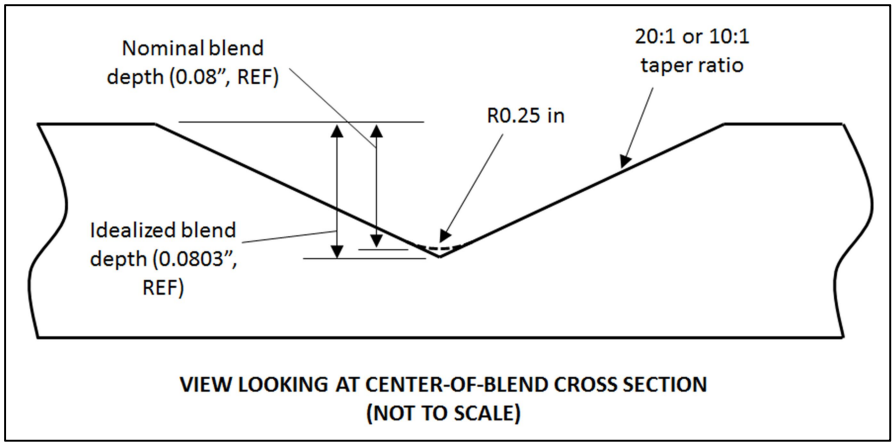

Figure 23 Blend Idealization

skin/stringer interfaces in order to better represent the physical skin panel specimens (this fillet is neglected from all reported section properties and analytical calculations).

3) "Model." This study utilizes ANSYS' automated mesh generation using a combination of brick (quad) and tetrahedral (tri) elements (ANSYS codes Solid186 and Solid187, respectively). The presence of geometric irregularities, including vent holes, surface blends, and corner radii, preclude the use of an all quad mesh. See the convergence study results in section 4.2.2 for additional details. Specific options selected are: a) hex dominant method (quad/tri); b) 0.1 in element size.

4) "Setup." Setup options are as follows.

    a) Analysis settings:

        i. Step controls: time steps are applied in order to reduce computation time and ensure a high-fidelity solution at the point of maximum load. Steps are assigned in deflection increments of 0.05 in. Initial steps (step 1 and step 2) are

assigned up to five substeps, increasing to up to 50 substeps at the point of maximum load. Note that maximum load is attained in either step 5 or step 6 in all simulations.

ii. Auto time stepping: on (define by: substeps).

iii. Large deflection: on.

b) Supports:

i. Fixed support: a fixed support is applied to one of the end faces of the model. This simulates a potted specimen at the fixed side of a test frame.

ii. Remote displacement: as with physical testing, FEA simulations are run via a displacement-controlled method. A remote displacement is applied to the opposite face of the model from the fixed support. All displacements and rotations are fixed except for the Z-direction (axial).

- Z displacement: 0.05 in per step;
- Behavior: rigid (to prevent "twisting" of the end face due to flange buckling).

5) "Solution." Axial load and deflection are the only required data for comparison against experimental results. Hard drive storage was extremely limited and could not support full data saves for all specimens.

a) Force reaction: applied at the fixed end (for functionality similar to a load cell).

b) Deformation probe: applied at the displaced end (for functionality

similar to a stringpot or extensometer).

4.2.2 Convergence Studies

As previously mentioned, hard drive storage was limited on the computers available to the author (8 GB). In many cases, especially for high element counts, this was insufficient to store full stress and strain data for a single simulation. For this reason, as well as a desire to reduce required computation time, it was necessary to reduce the element count as much as possible while still ensuring an accurate solution.

Two primary variables are examined in this section: element type (quad vs. tri) and element size. Additionally, two specimens are chosen for analysis. Specimen 2C is chosen due to its greater number of geometric features than other specimens, including a surface blend, fuel vent holes, and the presence of a stepped stringer shape (as opposed to a constant taper); see Appendix A for additional details of the stepped stringer shape. Specimen 8B is chosen as the other validation specimen due to its lesser degree of geometric features than other specimens, namely the lack of fuel vent holes and surface blends. It was initially assumed that these two specimens represent, respectively, the lowest and highest quad:tri element ratios for a given element size. Although this was later proven untrue (specimens 3B, 5B, and 7B all mesh with higher quad:tri ratios than 8B, most likely due to their greater thicknesses, and therefore higher total element counts), the results of specimens 2C and 8B are deemed consistent enough so as to not require additional convergence testing.

The same analysis setup and conditions as described previously in section 4.2.1 are utilized, except for the element meshing options. Convergence testing requires variations in the meshing method (tetrahedrons vs. hex dominant) and element size.

Results are shown in Table 11 and Table 12.

As can be seen in these tables (specifically, the column for percent change in maximum load), the hex dominant mesh shows a greater degree of convergence at a 0.1 in element size than the tetrahedron mesh achieves even at 0.08 in. Stated another way, the hex dominant method shows better convergence at approximately half the number of total elements. This is especially important considering the limited computing power and storage space available to this author (as shown by the failed solution in Table 12).

For the purposes of this study, an element size of 0.1 in is assumed to give a converged solution. In both test cases, this element size (using the hex dominant method) results in a less than 0.2% change in maximum load despite a nearly twofold increase in the total number of elements of a larger element size. For easier comparison, the convergence test results are presented graphically in Figure 24, Figure 25, Figure 26, and Figure 27. Figure 24 and Figure 25 are shown in terms of maximum load vs. element size. Although a less common method of displaying convergence results, the element size represents a reasonable method for modifying the mesh density of an auto-meshed model (as opposed to the total number of elements, which is not directly defined by the user). More typical representations of convergence using maximum load vs. the total number of elements are shown in Figure 26 and Figure 27. Especially at smaller element sizes, it is clearly shown that a relatively small change in element size can result in a significant change in the total number of elements. It is also clearly shown that that the hex dominant meshes provide for more rapid converge than tetrahedron-only meshes, at least for the geometries tested in this study. For graphical comparison, Figure 28 shows specimen 2C meshed with an element size of 0.1 in. Mesh detail through the cross section and around

Table 11 Convergence of Tetrahedron Mesh

Element Size (in)	No. of Elements	Max Load (lb)	Delta (lb)	Delta (%)
Specimen 2C				
0.5	4242	128080	--	--
0.4	5641	120150	-7930	-6.19%
0.3	9114	115330	-4820	-4.01%
0.2	18142	112380	-2950	-2.56%
0.15	37366	111280	-1100	-0.98%
0.125	51560	111020	-260	-0.23%
0.1	80851	110700	-320	-0.29%
0.09	111261	110460	-240	-0.22%
0.08	163276	110250	-210	-0.19%
Specimen 8B				
0.5	3670	155600	--	--
0.4	4949	149650	-5950	-3.82%
0.3	7278	147660	-1990	-1.33%
0.2	17117	143380	-4280	-2.90%
0.15	28022	142450	-930	-0.65%
0.125	46825	141800	-650	-0.46%
0.1	73347	141650	-150	-0.11%
0.09	100658	141460	-190	-0.13%
0.08	145074	141320	-140	-0.10%

Table 12 Convergence of Hex Dominant Mesh

Element Size (in)	No. of Elements	Quad:Tri Ratio	Max Load (lb)	Delta (lb)	Delta (%)
Specimen 2C					
0.5	2161	Unknown	116960	--	--
0.4	3775	Unknown	116560	-400	-0.34%
0.3	5111	Unknown	112690	-3870	-3.32%
0.2	11794	8.0	111420	-1270	-1.13%
0.15	29570	5.7	110340	-1080	-0.97%
0.125	50710	7.9	110030	-310	-0.28%
0.1	93844	7.8	109890	-140	-0.13%
0.09	112656	10.6	109880	-10	-0.01%
0.08	160593	11.0	Could not solve (insufficient memory)		
Specimen 8B					
0.5	2250	3.8	150250	--	--
0.4	2580	8.2	146090	-4160	-2.77%
0.3	3792	16.6	142590	-3500	-2.40%
0.2	10116	14.4	141610	-980	-0.69%
0.15	20190	16.0	141420	-190	-0.13%
0.125	38948	27.8	141070	-350	-0.25%
0.1	77268	12.5	141000	-70	-0.05%
0.09	97671	12.5	141000	0	0.00%
0.08	134719	20.2	140990	-10	-0.01%

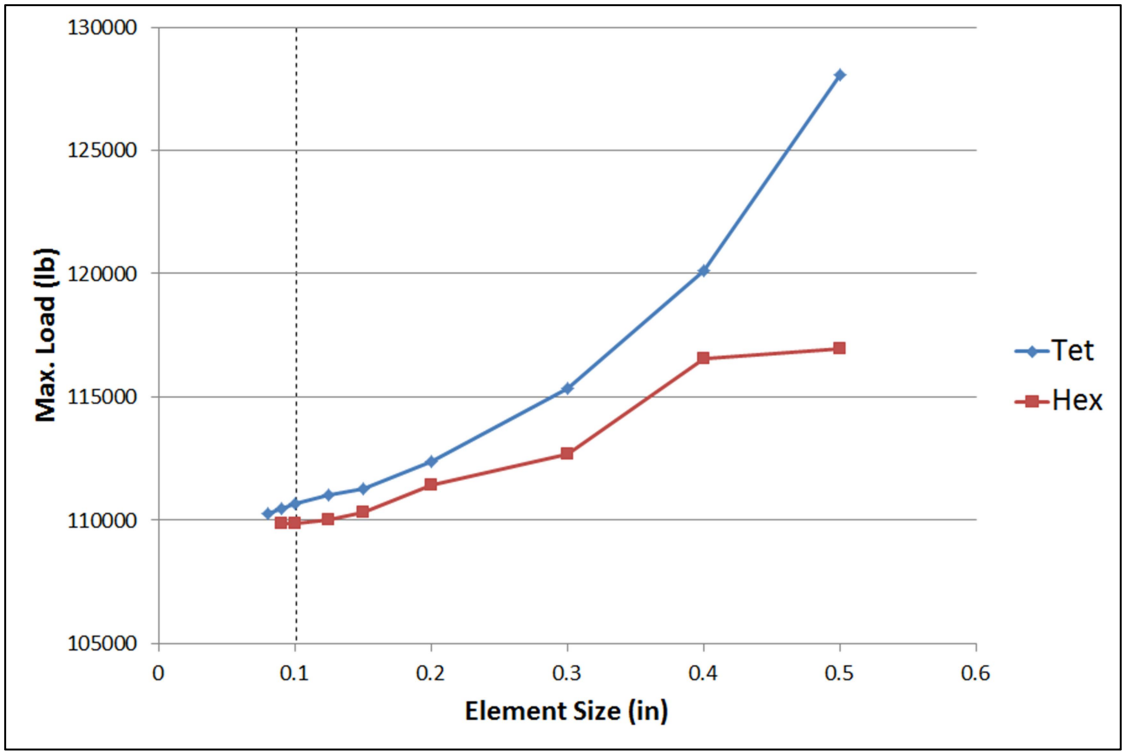

Figure 24 Convergence of Specimen 2C, Maximum Load vs. Element Size

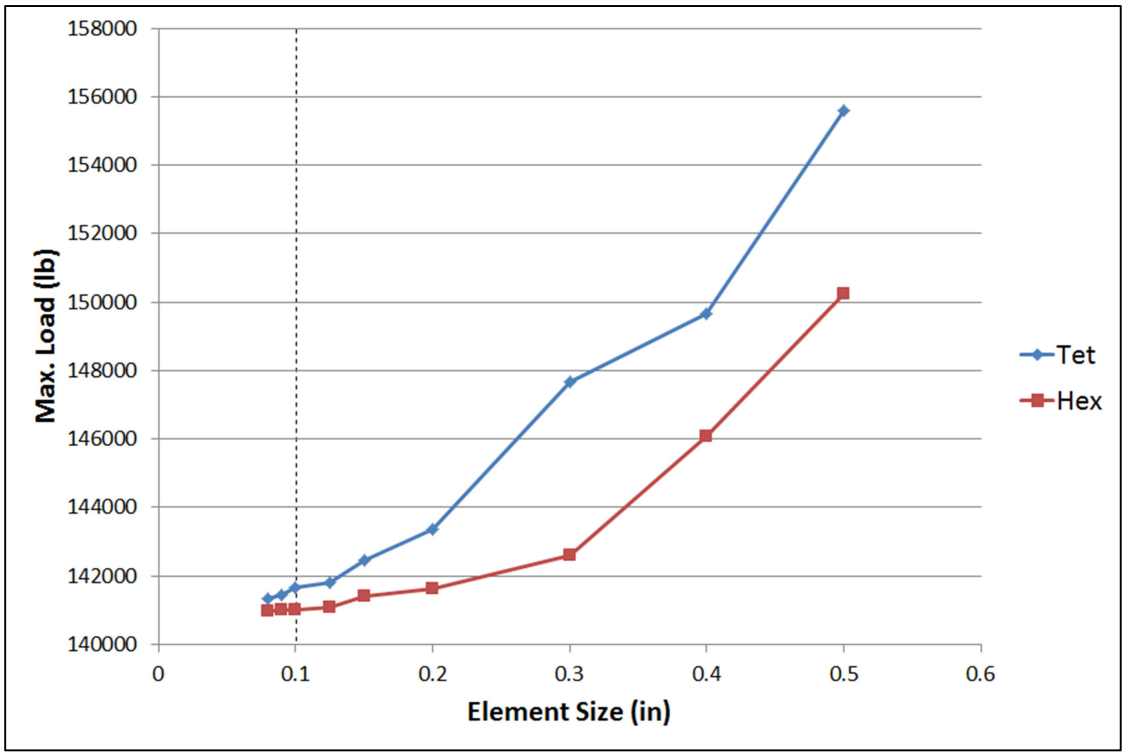

Figure 25 Convergence of Specimen 8B, Maximum Load vs. Element Size

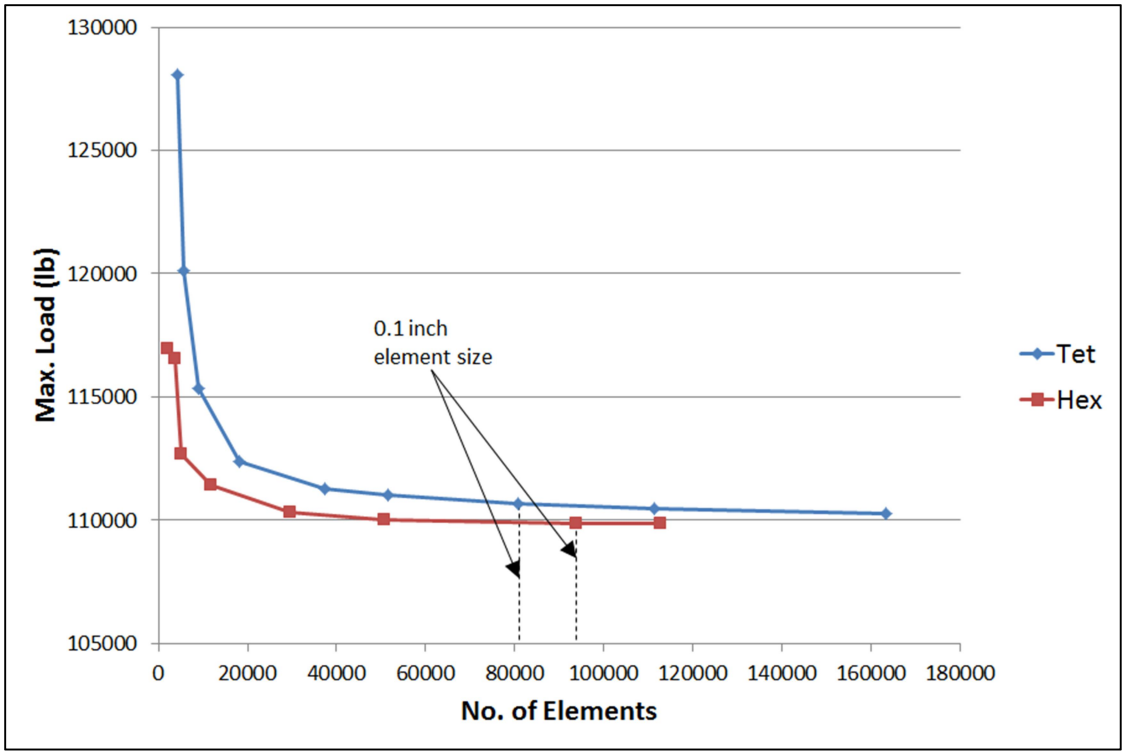

Figure 26 Convergence of Specimen 2C, Maximum Load vs. Number of Elements

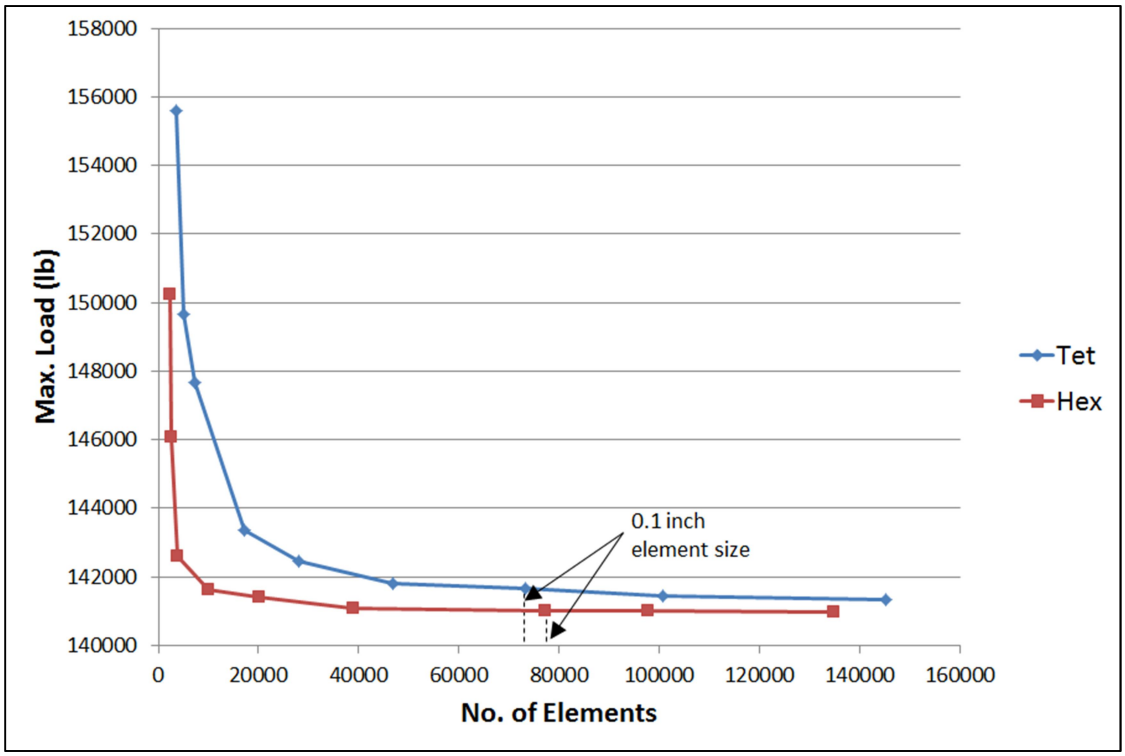

Figure 27 Convergence of Specimen 8B, Maximum Load vs. Number of Elements

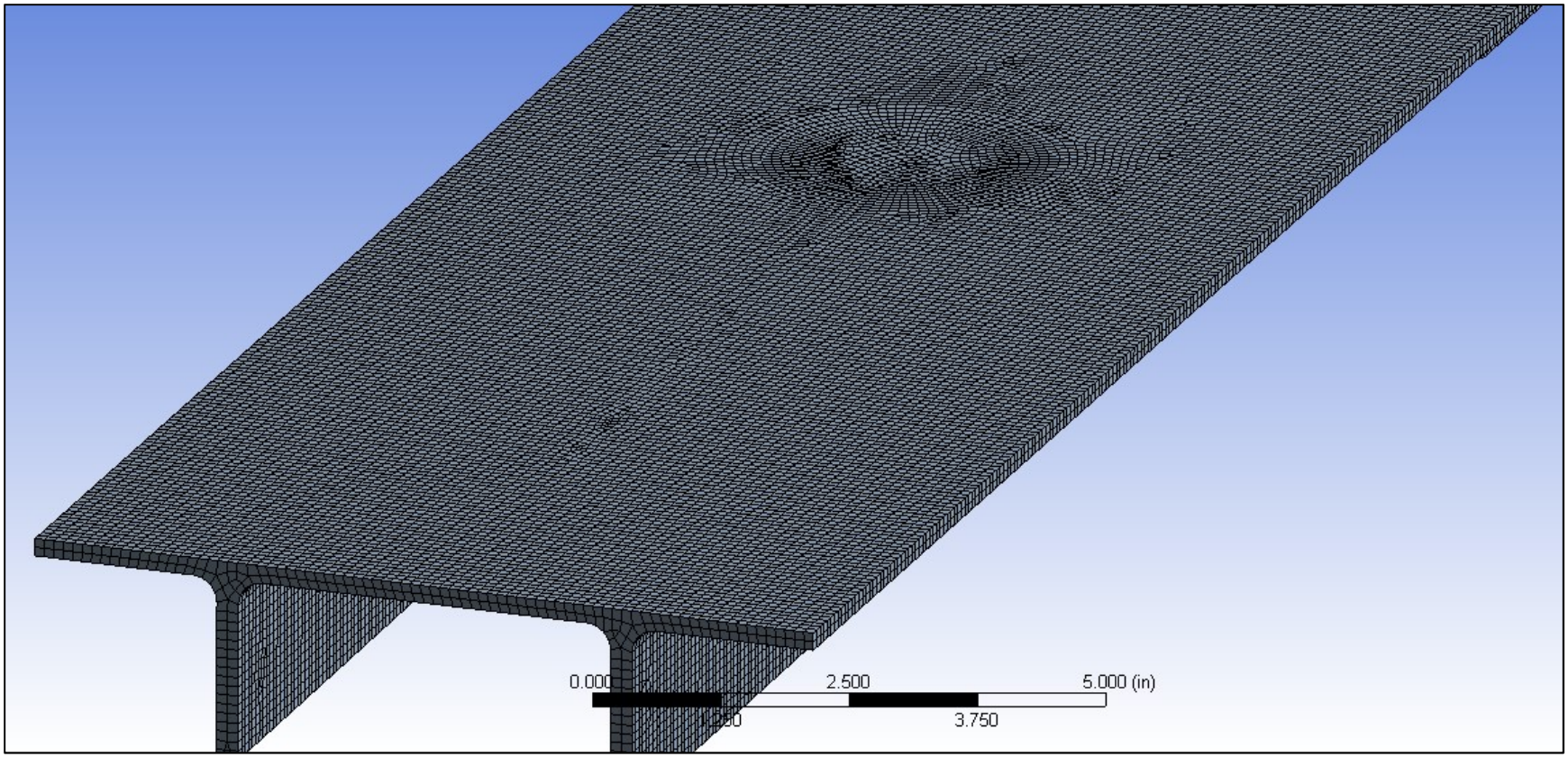

Figure 28 Finite Element Mesh Example

the blend is visible.

4.2.3 FEA Validation

Validation of FEA results is an important step in ensuring that the simulation setup is appropriate. Physical/experimental test results are documented previously in Table 4 and Table 6. Comparisons against tabular FEA data are shown in Table 13. These results are compared visually in Figure 29 with ±10% error bands against the experimental data.

All FEA results are within 8.7% of the associated experimental result; the average variance is 3.6%. The worst correlations are for specimens 2B and 2C (the average variance drops to 2.6% if these results are excluded). It is unknown why both of the "2-series" specimens are the worst correlators, but may be due to the nonstandard geometry of these specimens. The stringers of specimens 2B and 2C contain a stepped profile which is difficult to measure, and therefore model, with a high degree of accuracy. Note also that specimens 8B and 8C are modeled without fuel vent holes in order to simulate the plugged vent holes on the associated physical test specimens.

An interesting phenomenon to note is the conservative nature of the FEA results as compared to experimental findings. Only two specimens (7B and 8B) show the FEA results to be unconservative, and even then by a margin of less than 0.6% in both cases. This is surprising for a few reasons. First, FEA simulations utilize fully rigid end restraints against deflection, rotation, and deformation in general. In contrast, the Wood's metal potting compound used in physical testing is an elastic restraint, less rigid than both the steel fixturing and the aluminum test specimens (see also section 2.4.2). Secondly, the physical test specimens were subject to imperfections in perpendicularity/flatness of the

Table 13 FEA Results and Validation

Specimen	Max Load, Test (lb)	Max Load, FEA (lb)	Variation (%)	Critical Deflection (in)	No. of Elements	Quad:Tri Ratio
2B	134394	122700	-8.7%	0.2475	91576	8.9
2C	117236	109890	-6.3%	0.2350	93844	7.8
3B	179901	174080	-3.2%	0.2500	83494	12.8
3C	178570	167400	-6.3%	0.2400	91310	10.0
5B	199184	192090	-3.6%	0.2850	82084	13.9
5C	179741	173430	-3.5%	0.2325	94073	9.1
7B	158443	158870	0.3%	0.2525	80997	13.0
7C	153682	151290	-1.6%	0.2350	88880	10.0
8B	140185	141000	0.6%	0.2375	77628	12.5
8C	126354	121470	-3.9%	0.2225	87251	8.3

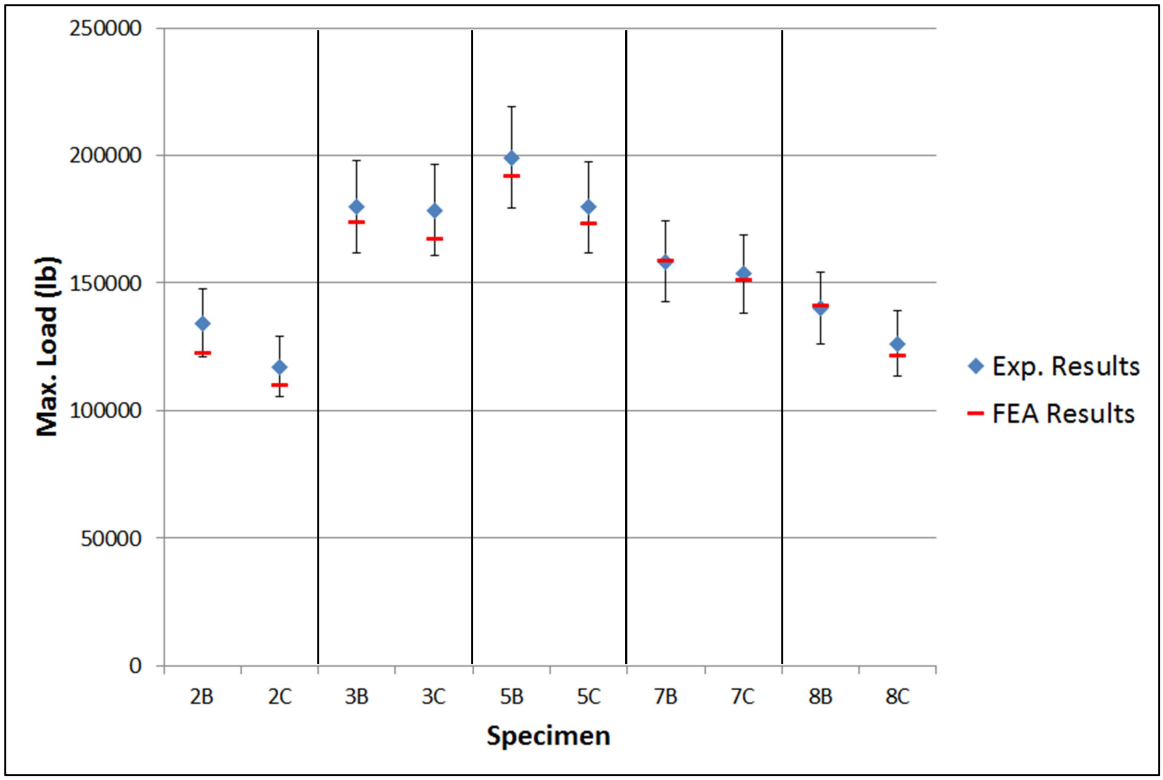

Figure 29 FEA Validation

loaded edges, as well as imperfect alignment into the load frame. In theory, this should have reduced their ability to resist buckling as compared to the "perfect" geometry and loading of the FEA simulations. One factor that may have contributed to this effect is that the physical test specimens were cut from an upper wing skin with slight aerodynamic curvature. Although the radius of curvature for each specimen is assumed sufficiently large as to be insignificant [24], its absence may have resulted in an "artificial" reduction in strength for the FEA simulations.

Nevertheless, it is important to note that absolute errors between experimental and FEA results are less important than the relative differences between each blended and unblended specimen pair. In other words, the stated purpose of this study is to predict reductions in buckling resistance due to the presence of corrosion blends. Comparisons of

blended and unblended pairs are detailed in Table 14 (with reference to Table 13 for the buckling load of each specimen). Despite an 8.7% maximum and 3.6% average variation between experimental and FEA results for absolute load carrying capability, Table 14 shows only a 4.0% maximum and 1.3% average variation between experimental and FEA results for reductions in load carrying capability. Note that these results include a variety of blend depths (0.08 to 0.14 in), blend shapes (circular and elliptical), and plugged vs. open fuel vent holes (see also section 2.3.2 and section 2.3.3).

4.3 Analysis of Test Variables

Additional finite element simulations and closed-form calculations are documented in order to determine the effects of various test variables. Specifically, a series of blend shapes, blend depths, and plugged or unplugged fuel vent hole configurations are analyzed. All FEA simulations are set up as previously discussed in section 4.2.1. Although some of the simulations closely mirror geometries and results previously reported in the FEA validation studies, the below sections represent independent analysis phases.

Table 14 Reductions in Buckling Load due to Blending

Specimen Pair	Load Reduction, Experimental (lb)	Load Reduction, FEA (lb)	Load Reduction, Experimental (%)	Load Reduction, FEA (%)	Variance (%)
2B/2C	17158	12810	12.8%	10.4%	-2.3%
3B/3C	1331	6680	0.7%	3.8%	3.1%
5B/5C	19443	18660	9.8%	9.7%	0.0%
7B/7C	4761	7580	3.0%	4.8%	1.8%
8B/8C	13831	19530	9.9%	13.9%	4.0%

4.3.1 Effects of Blend Shape

Both circular and elliptical blends are considered in this study. As discussed in section 2.3.2, all blends are modeled at a 20:1 blend ratio in the axial direction. For circular blends, the transverse ratio is also 20:1. However, for elliptical blends this ratio is reduced to 10:1 in the transverse direction in order to simulate an alternate blend shape which may be considered during real-world aircraft repair. The real-world intent would likely be to reduce the total blend width, which for deep blends may be excessively wide and/or extend over substructural features (such as integral stringer flanges). Therefore, elliptical blends are only simulated for deeper blends (60% and 75% of the skin thickness).

Ultimately, FEA simulations show negligible differences between the two blend shapes when compared against certain sectional properties (namely, lost cross-sectional area and lost moment of inertia of the section). This is not to say that structural stability is irrespective of blend shape, but rather that blend shape does not appear to affect overall correlations with lost area and/or inertia. Therefore, results of the blend shape analyses are combined with those of the blend depth analyses and are reported together in section 4.3.2.

4.3.2 Effects of Blend Depth

In order to quantify the effects of blend depth on buckling resistance, a series of finite element simulations are performed on each of the five blended specimen geometries (specimens 2C, 3C, 5C, 7C, and 8C). Simulations are performed for each geometry with circular blends at depths of 0%, 15%, 30%, 45%, 60%, and 75% of the skin thickness. Additionally, each of the geometries are also analyzed with simulated

elliptical blends (10:1 ratio in the transverse direction) with depths of 60% and 75% of the skin thickness. All simulations are performed with open fuel vent hole configurations.

Results of these simulations are compared against various sectional properties including skin thickness (t), cross-sectional area (A), moment of inertia (I), and radius of gyration (ρ). It is assumed that these properties, and associated methods of calculating them, are commonly known among the engineering community. It is also assumed that determination of section properties for other-than-simple geometries is often performed via computer modeling rather than hand calculations. In fact, the complexities of detailing the variables and equations necessary to duplicate hand calculations for each of the 40 specimen models considered in this section make such a table impractical to include in this report. Therefore, in the interests of brevity, hand calculations for section properties are not shown in this report (though all displayed values can be verified, if desired, by referring to the geometries and blend shapes detailed in Table 1, Table 3, and Appendix A). Only the data of importance to this study (i.e., the relative change in each section property due to the presence of a surface blend) is shown. Note that most of the specimens include tapering skin and stringer thicknesses; all section properties are therefore calculated at the center of the blend (which corresponds to the center of each specimen along its axial length). See Table 15 for full details. In order to more easily visualize these results and any associated correlations, results are shown graphically in terms of lost thickness (Figure 30), lost area (Figure 31), lost inertia (Figure 32), and increase in radius of gyration (Figure 33).

As previously discussed, the circular and elliptical blend data are nearly indistinguishable in Figure 31 and Figure 32. Since it is desirable to document

Table 15 Effects of Blend Depth and Shape

Speci-men	Blend Ratio	Blend Depth (%)	Blend Depth (in)	Blend Width (in)	Max Load (lb)	Lost Load (%)	t_{lost} (%)	A_{lost} (%)	I_{lost} (%)	ρ_{gained} (%)
2C	20:1	0%	0.000	0.00	125530	0.00%	0.00%	0.00%	0.00%	0.00%
2C	20:1	15%	0.026	1.04	126140	-0.49%	14.99%	0.64%	0.36%	0.14%
2C	20:1	30%	0.052	2.08	118250	5.80%	29.97%	2.53%	1.41%	0.57%
2C	20:1	45%	0.078	3.12	110370	12.08%	44.96%	5.67%	3.14%	1.34%
2C	20:1	60%	0.104	4.16	104290	16.92%	59.94%	10.08%	5.60%	2.46%
2C	20:1	75%	0.130	5.20	98036	21.90%	74.93%	15.73%	8.94%	3.95%
3C	20:1	0%	0.000	0.00	177930	0.00%	0.00%	0.00%	0.00%	0.00%
3C	20:1	15%	0.030	1.20	178310	-0.21%	14.93%	0.62%	0.45%	0.09%
3C	20:1	30%	0.060	2.40	176980	0.53%	29.85%	2.48%	1.78%	0.36%
3C	20:1	45%	0.090	3.60	163920	7.87%	44.78%	5.58%	3.99%	0.83%
3C	20:1	60%	0.121	4.84	153510	13.72%	60.20%	10.07%	7.32%	1.52%
3C	20:1	75%	0.151	6.04	143600	19.29%	75.12%	15.67%	11.76%	2.29%
5C	20:1	0%	0.000	0.00	193210	0.00%	0.00%	0.00%	0.00%	0.00%
5C	20:1	15%	0.030	1.20	193810	-0.31%	15.08%	0.59%	0.46%	0.06%
5C	20:1	30%	0.060	2.40	185970	3.75%	30.15%	2.35%	1.82%	0.27%
5C	20:1	45%	0.090	3.60	175380	9.23%	45.23%	5.29%	4.09%	0.63%
5C	20:1	60%	0.119	4.76	165730	14.22%	59.80%	9.23%	7.26%	1.08%
5C	20:1	75%	0.149	5.96	155930	19.30%	74.87%	14.47%	11.72%	1.60%
7C	20:1	0%	0.000	0.00	162390	0.00%	0.00%	0.00%	0.00%	0.00%
7C	20:1	15%	0.031	1.24	160300	1.29%	15.16%	0.73%	0.46%	0.13%
7C	20:1	30%	0.061	2.44	159960	1.50%	29.83%	2.80%	1.75%	0.54%
7C	20:1	45%	0.092	3.68	146330	9.89%	44.99%	6.36%	3.96%	1.27%
7C	20:1	60%	0.123	4.92	135850	16.34%	60.15%	11.36%	7.18%	2.33%
7C	20:1	75%	0.153	6.12	125830	22.51%	74.82%	17.57%	11.46%	3.64%
8C	20:1	0%	0.000	0.00	134770	0.00%	0.00%	0.00%	0.00%	0.00%
8C	20:1	15%	0.026	1.04	135130	-0.27%	14.86%	0.60%	0.37%	0.12%
8C	20:1	30%	0.053	2.12	128710	4.50%	30.29%	2.48%	1.48%	0.51%
8C	20:1	45%	0.079	3.16	119250	11.52%	45.14%	5.49%	3.26%	1.17%
8C	20:1	60%	0.105	4.20	112170	16.77%	60.00%	9.70%	5.81%	2.13%
8C	20:1	75%	0.131	5.24	104860	22.19%	74.86%	15.08%	9.25%	3.38%
2C	10:1	60%	0.104	2.08	111650	11.06%	59.94%	5.04%	2.65%	1.25%
2C	10:1	75%	0.130	2.60	108060	13.92%	74.93%	7.87%	4.09%	2.03%
3C	10:1	60%	0.121	2.42	165740	6.85%	60.20%	5.03%	3.47%	0.82%
3C	10:1	75%	0.151	3.02	159510	10.35%	75.12%	7.84%	5.38%	1.32%
5C	10:1	60%	0.119	2.38	177780	7.99%	59.80%	4.62%	3.45%	0.61%
5C	10:1	75%	0.149	2.98	171580	11.20%	74.87%	7.23%	5.40%	0.98%
7C	10:1	60%	0.123	2.46	148430	8.60%	60.15%	5.68%	3.37%	1.21%
7C	10:1	75%	0.153	3.06	142180	12.45%	74.82%	8.78%	5.18%	1.95%
8C	10:1	60%	0.105	2.10	120960	10.25%	60.00%	4.85%	2.76%	1.09%
8C	10:1	75%	0.131	2.62	116810	13.33%	74.86%	7.54%	4.25%	1.76%

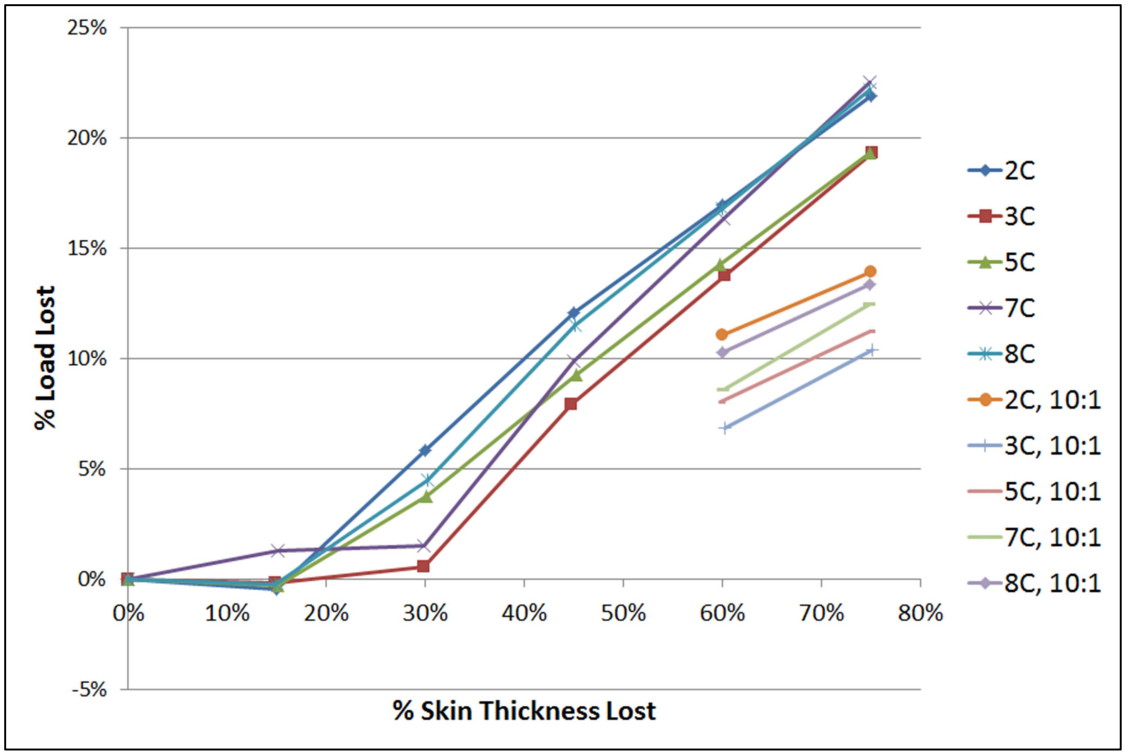

Figure 30 Lost Load vs. Lost Thickness

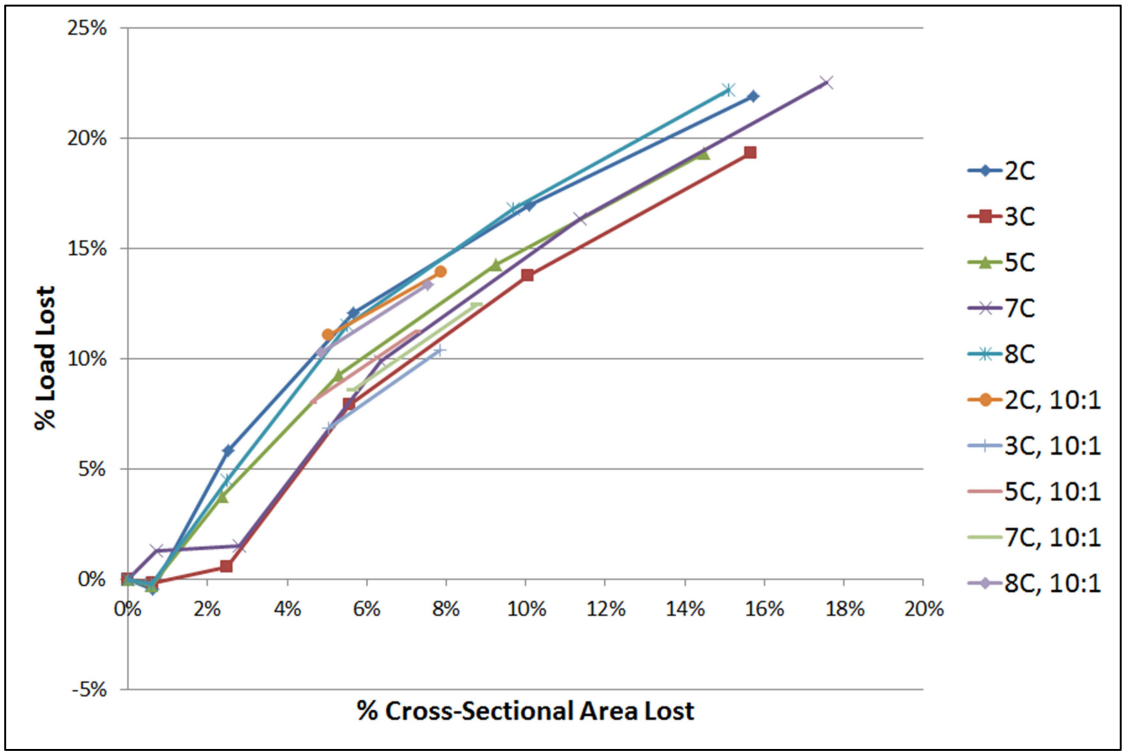

Figure 31 Lost Load vs. Lost Area

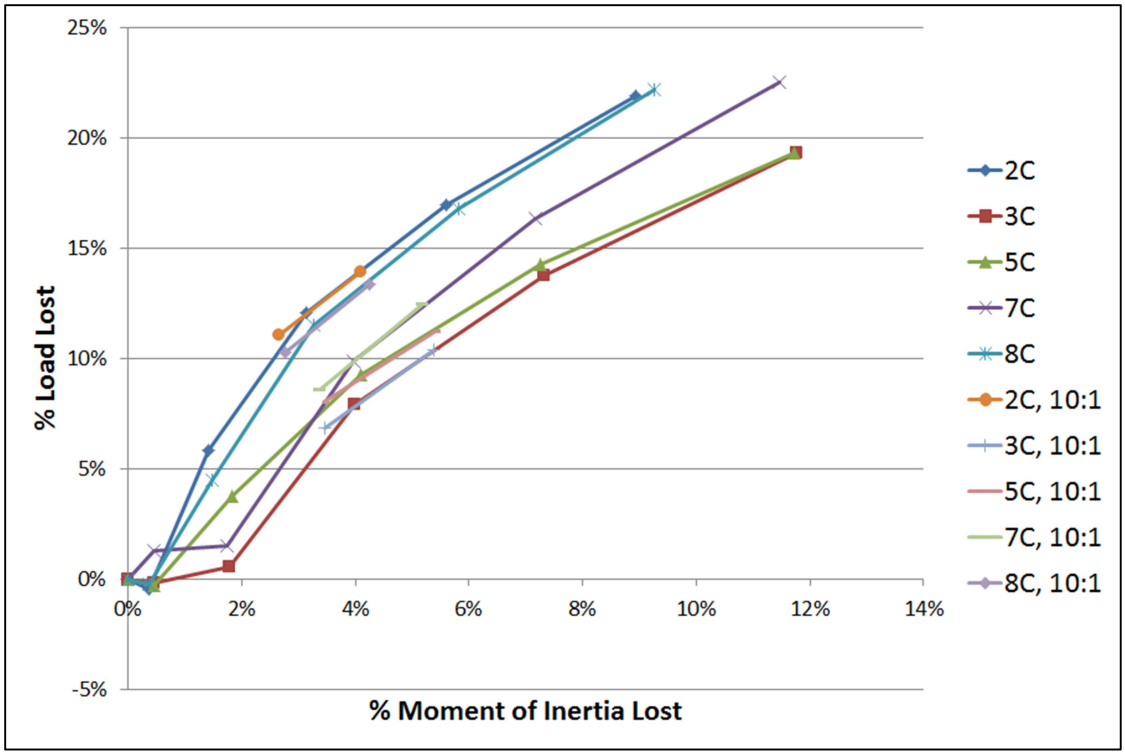

Figure 32 Lost Load vs. Lost Inertia

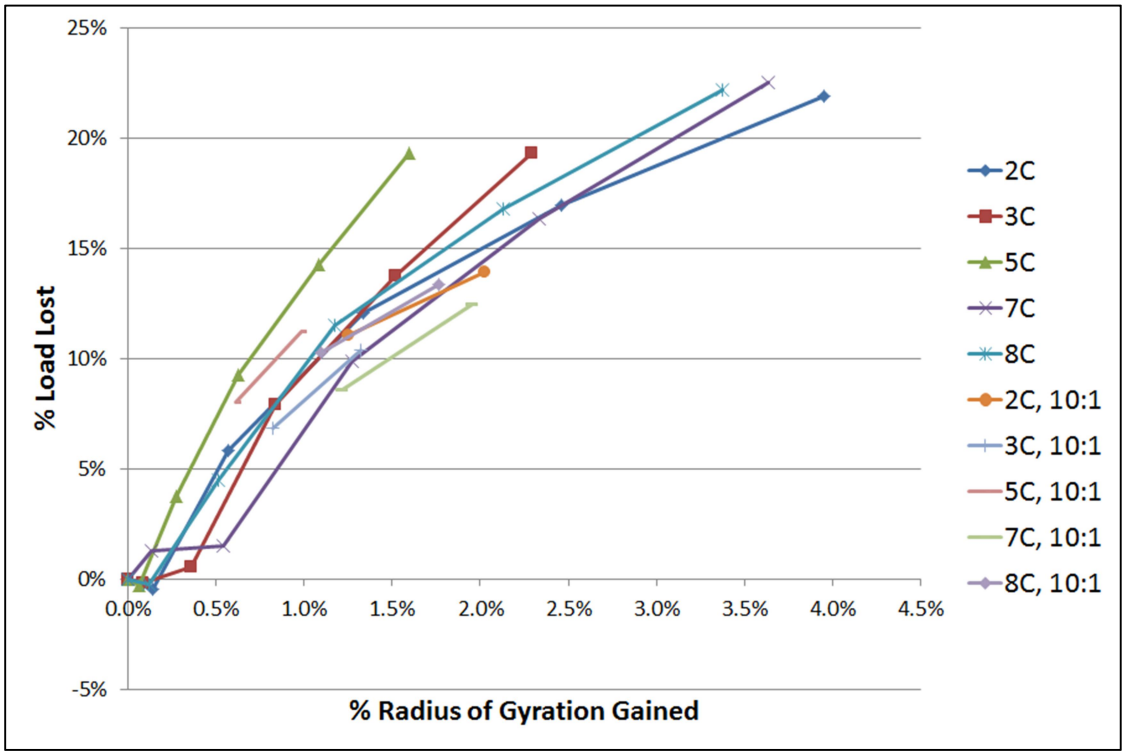

Figure 33 Lost Load vs. Gained Radius of Gyration

correlations which are applicable to a wide range of blend shapes and sizes, these two data series are considered the most relevant for further investigation. Various correlations are attempted in an effort to provide for better data fits against common section properties, with the relationship to skin thickness proving the most reliable. Results of some of the better correlations against lost load carrying capability are shown in Table 16. The obvious trend from Table 16 is that greater powers of t_{skin} in the denominator tend to increase the coefficient of determination. When plotted visually, however, some interesting trends are noted which are difficult to quantify numerically. See Figure 34 and Figure 35 for examples.

In both of these figures, data correlations are strongest through the middle of the data range, but begin to diverge and become unconservative at the upper ranges (which correspond to deeper blends of up to 75% of the skin thickness). Perhaps the most interesting anomaly is the tightly packed nature of the data in Figure 35, with the exception of specimen 7C. In fact, if data from specimen 7C is neglected, the r^2 correlation for this dataset increases from 0.986 to 0.993, though it is not the intent of this study to disregard anomalous data. Therefore, despite the numerically superior r^2 values

Table 16 Comparison of Correlation Variables

X-axis Variable	**r^2**
$\%A_{lost}$	0.982
$\%A_{lost} / t_{skin}$	0.990
$\%A_{lost} / t_{skin}^2$	0.991
$\%I_{lost}$	0.963
$\%I_{lost} / t_{skin}$	0.975
$\%I_{lost} / t_{skin}^4$	0.986

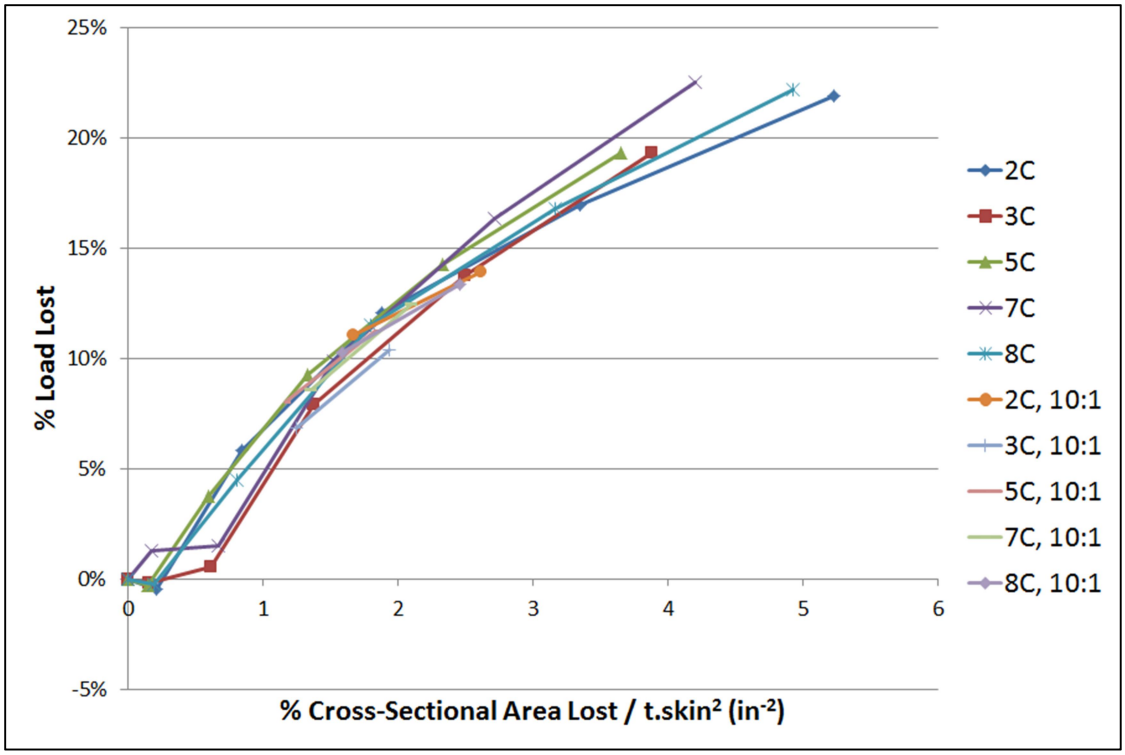

Figure 34 Lost Load vs. Lost Area over Skin Thickness Squared

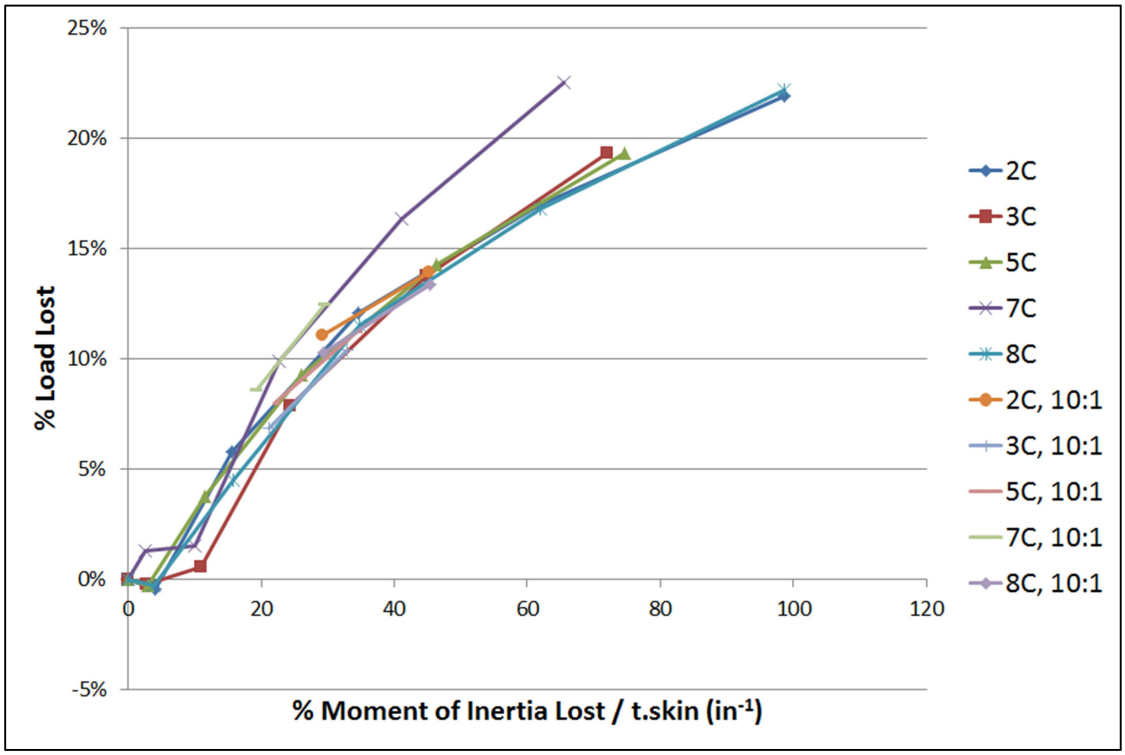

Figure 35 Lost Load vs. Lost Inertia over Skin Thickness to the Fourth Power

associated with exponential skin thickness factors, these data appear to be unreliable for deeper blends.

Considering the above, the best data fit for analytical use appears to be a function of the lost cross-sectional area divided by skin thickness. This conclusion is primarily based on four assumptions: 1) calculation of the cross-sectional area, especially for blended geometry, is significantly simpler and less prone to error than moment of inertia calculations; 2) the resulting r^2 value is the second highest of all the attempted correlations, and even then by only the slightest of margins (0.990 vs. 0.991); 3) although the dataset is slightly unconservative near the middle of the data range, it tends to be conservative at both the lower and upper ends of the range; and 4) the data appear to be converging rather than diverging at the upper end of the data range. These trends can be seen visually in Figure 36.

Experimental data are shown in Figure 36 for reference purposes only. Because each data point is based on stability testing of two separate specimens with slightly different geometries, the lost cross-sectional area and skin thickness calculations are imperfect. The equation for the curve fit shown in Figure 36 is as follows:

$$y = -0.113x^2 + 0.350x$$

or,

$$\%P_{lost} = -0.113in^2\left(\frac{\%A_{lost}}{t_{skin}}\right)^2 + 0.350in\left(\frac{\%A_{lost}}{t_{skin}}\right) \tag{9}$$

In terms more likely to be used in stress analysis, Equation (9) can be rewritten as follows:

$$P_{predict} = P_0\left[1 + 0.113in^2\left(\frac{A_{lost}}{A_0 * t_{skin}}\right)^2 - 0.350in\left(\frac{A_{lost}}{A_0 * t_{skin}}\right)\right] \tag{10}$$

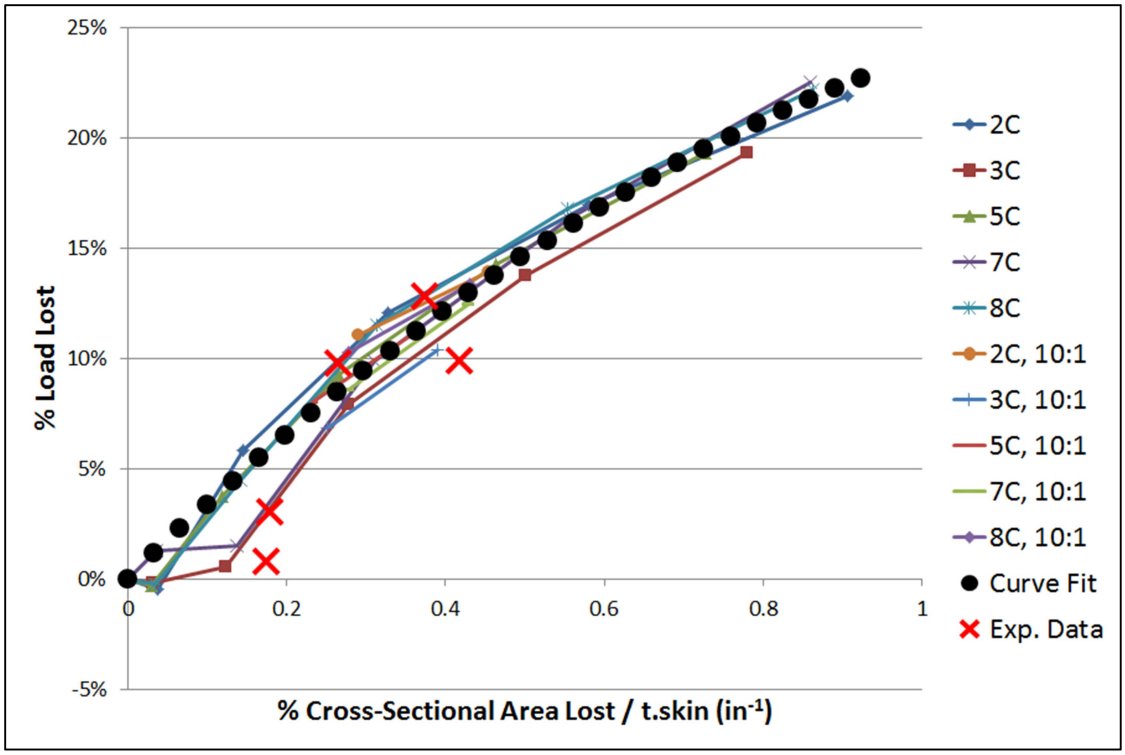

Figure 36 Lost Load vs. Lost Area over Skin Thickness

where

$P_{predict}$ predicted buckling load of the blended specimen;

P_0 calculated buckling load of the unblended specimen;

A_{lost} lost cross-sectional area (measured at center of blend);

A_0 nominal (unblended) cross-sectional area at the center of the blend;

t_{skin} nominal (unblended) skin thickness at the center of the blend.

Interestingly, the quadratic relationship described by Equations (9) and (10) bears similarities with one of the primary variables, *K*, in Niu's method for "Cutouts in Skin-Stringer Panels under Axial Load" [11], where

$$K = \frac{G}{Eb}\left(\frac{t}{A}\right)$$

The physical similarities between cutouts and local blends in skin-stringer panels are not

unnoticed. The material properties G (shear modulus) and E (Young's modulus) and geometric property b (stringer spacing) in the above equation are not examined in this study due to similarities in geometry and material properties among the specimens available for testing. The remaining variables, t and A (thickness and area), are the same variables, at the same exponential-power ratio as those identified herein to best describe the effects of a surface blend (though their relationship is inverted). Niu's method is, however, a stress-based rather than load-based analysis.

Table 17 and Table 18 compare buckling loads as predicted by Equation (10) against experimental test results and FEA validation results, respectively. The blended and unblended test results are as previously reported in Table 4, Table 6, and Table 13. In terms of variance between predicted results and test results, a positive value indicates that the prediction is unconservative and a negative value indicates a conservative prediction.

4.3.3 Effects of Fuel Vent Holes

Although determining the effects of vent holes is not one of the stated purposes of this study, it is a variable that was introduced into the test program and is therefore subject to evaluation (see also section 2.3.3). Specimens 8B and 8C are the only specimens evaluated in this section. Results of this evaluation are shown in Table 19.

Although based on a small sample size, the data indicates that vent holes may affect blended specimens more than unblended specimens. Perhaps not surprisingly, Figure 30 through Figure 32 show specimens 2C and 8C as tending to have the greatest loss in load carrying capability for a given loss in cross section (the data for specimen 8C in these figures are for open vent hole configurations). These specimens are the only two specimens which contain a fuel vent hole within 1 in of the center of the blend (vent

Table 17 Comparison of Experimental Results to Predicted Buckling Loads

Specimen	P_0 (lb)	$A_{nominal}$ (in^2)	$A_{blended}$ (in^2)	t_{skin}	$P_{predict}$ (lb)	P_{exp} (lb)	Variance (%)
2B/2C	134394	2.1658	2.0250	0.1735	118902	117236	1.42%
3B/3C	179901	2.8882	2.7871	0.2010	169554	178570	-5.05%
5B/5C	199184	3.0392	2.8790	0.1990	182299	179741	-1.42%
7B/7C	158443	2.6467	2.5494	0.2045	149055	153682	-3.01%
8B/8C	140185	2.3218	2.1522	0.1750	122470	126354	-3.07%[5]

Table 18 Comparison of FEA Results to Predicted Buckling Loads

Specimen	P_0 (lb)	A_{lost} (in^2)	$A_{nominal}$ (in^2)	t_{skin}	$P_{predict}$ (lb)	P_{FEA} (lb)	Variance (%)
2C	122700	0.1285	2.1535	0.1735	109570	109890	-0.29%
3C	174080	0.1285	2.9156	0.2010	161666	167400	-3.43%
5C	192090	0.1964	3.0755	0.1990	172747	173430	-0.39%
7C	158870	0.1213	2.6708	0.2045	147402	151290	-2.57%
8C	141000	0.1285	2.2807	0.1750	126763	121470	4.36%[5]

Table 19 Effects of Fuel Vent Holes

Specimen	P_{exp} (lb) Plugged	P_{FEA} (lb) Plugged	P_{FEA} (lb) Open	FEA Variance (%)
8B	140185	141000	139470	1.09%
8C	126354	121470	118980	2.05%

[5] Experimental and finite element analysis results for specimens 8B and 8C as shown in this table are for a plugged fuel vent hole configuration.

holes are at least 4 in from the blend center on all other specimens, as measured along the axial length of the specimen).

However, specimens 2C and 8C are also the only two specimens from the aft skin panel. It is therefore possible that the greater losses in load carrying capability are due to material properties rather than vent hole locations. Ultimately, attempts to improve the overall data fit by incorporating material property factors (E_c and F_{cy}) were unsuccessful. This is not surprising since the data in question are losses in load carrying capability of a given structure as opposed to its absolute load carrying capability. In other words, material properties are accounted for during evaluation of the nominal strength of an unblended specimen, and should not need to be reintroduced in order to predict percentage-based strength losses. Nevertheless, it is impossible to quantitatively determine the effects of vent hole location relative to blend location without significant departures from the stated scope of this study. Fortunately, the data fit described by Equation (10) accounts for the presence of fuel vent holes on all specimens with a correlation coefficient of 0.990. Thus, the results are considered applicable to a range of vent hole locations and there is little justification for expanding the scope of this study to include further evaluation.

4.4 Comparisons Against Closed-Form Stability Methods

One of the stated goals of this study is to compare the results of finite element analysis to traditional analysis methods. The ability of traditional analysis methods to account for a surface blend is otherwise unknown. The following sections lay out the groundwork for such an evaluation.

4.4.1 Elastic End Restraint

Many stability analysis methods, especially those focused on global rather than local failure modes, allow for various end restraint conditions as an analysis variable. The simplest conditions are free, pinned (i.e., simply supported), and fixed/clamped. More complex conditions may involve elastic end restraints. The potting compound used in the experimental portion of this study, while well suited for the complexities of testing, is far from rigid. Some form of data analysis is necessary in order to account for the elastic restraint provided by this potting.

The bar testing phase of this study was included primarily for this reason. By performing a series of easily analyzed tests (i.e., Euler buckling), it was hoped that an elastic restraint coefficient could be determined. Three specimens were tested of a material similar to that of the aircraft skin specimens. Overall test methods and results are discussed in previous chapters. More in-depth analysis of these results is provided in Table 20 (with reference to geometry and modulus as shown in Table 2 and Table 7, respectively). End restraint coefficients (C) are calculated via the Euler buckling equation [17]:

$$F_{critical\ (Euler)} = \frac{C\pi^2 E_c}{(L/\rho)^2} \tag{11}$$

4.4.2 Analytical Comparisons Against FEA Data

While the equations and tables which drive closed-form stability analysis methods often apply to a wide range of structural geometries, none are known which accurately account for local changes in cross section. A major challenge in the use of such methods for tapering and/or blended geometry is determining the failure criteria. For the case of a

Table 20 End Restraint Coefficients

Speci-men	E_c (psi)	Max Load (lb)	Area (in^2)	Critical Stress (psi)	ρ (in)	L_{column}	C	Variance from Avg. (%)
FP-1	1.104E7	14966	0.8815	16978	0.1455	21.79	3.495	-1.55%
FP-2	1.104E7	15352	0.8792	17460	0.1452	21.66	3.566	0.44%
FP-3	1.104E7	15720	0.8797	17869	0.1452	21.48	3.589	1.09%
						Avg:	**3.55**	

smoothly tapering specimen, for example, the location of highest stress is at the thinnest cross section, which is likely at one of the ends of the column. Yet it is extremely unlikely for local buckling failure to occur at this location (immediately adjacent to the end fixturing). Simply assuming failure by a maximum stress criterion is therefore not always a reliable method. In order to provide for a consistent methodology in this report, all predictions utilize the stress calculated at the center of the blend (which is the midpoint of the column for all models in this study). Reported section properties are calculated at the same location.

Three commonly-used analysis approaches are evaluated; each is briefly described below. Material properties for all analyses are based on the Ramberg-Osgood relationship as detailed in Table 9 and Table 10. Model geometry is as shown in Table 1 and Appendix A. Unless otherwise noted, all analyses assume a circular blend shape (20:1 taper in all directions) which is idealized as shown in Figure 23.

Approach 1 – column failure:

Euler-Engesser (or modified Euler) equation [17]:

$$F_{critical\ (Engesser)} = \frac{C\pi^2 E_t}{(L/\rho)^2} \tag{12}$$

Rankine equation [26]:

$$F_{critical\ (Rankine)} = \frac{F_{cy}}{1 + \frac{F_{cy}(L/\rho)^2}{C\pi^2 E_c}} \tag{13}$$

Johnson-Euler equation [27]:

$$F_{critical\ (Johnson)} = F_{cy} - \frac{\left(F_{cy}\right)^2 \left(\frac{L}{\rho\sqrt{C}}\right)^2}{4\pi^2 E_c} \tag{14}$$

In each of the above equations, the radius of gyration (ρ) is the geometry variable which changes due to the presence of a blend. Additionally, the cross-sectional area is modified for stress-to-force conversions. Each of the three equations requires use of an end restraint coefficient (C), chosen as 3.55 in this study (reference Table 20). Although physical testing and FEA simulations discount column failure as a likely failure mode for the geometries chosen in this study, the Euler-Engesser equation is known to support analysis of extruded cross sections, even at the short to intermediate column lengths examined herein [28]. It is therefore worth examining. Figure 37 compares results of the Euler-Engesser equation to the FEA curve fit defined in section 4.3.2. Results for the Rankine and Johnson-Euler equations are visually similar to the Euler-Engesser results, and are therefore not shown.

Figure 37 shows that the Euler-Engesser equation (in addition to the Rankine and Johnson-Euler equations), consistently underpredicts the lost load carrying capability for a given loss in cross section. Although alternative methods do exist to predict column failure for tapered and stepped cross sections [11], [24], such methods are even less

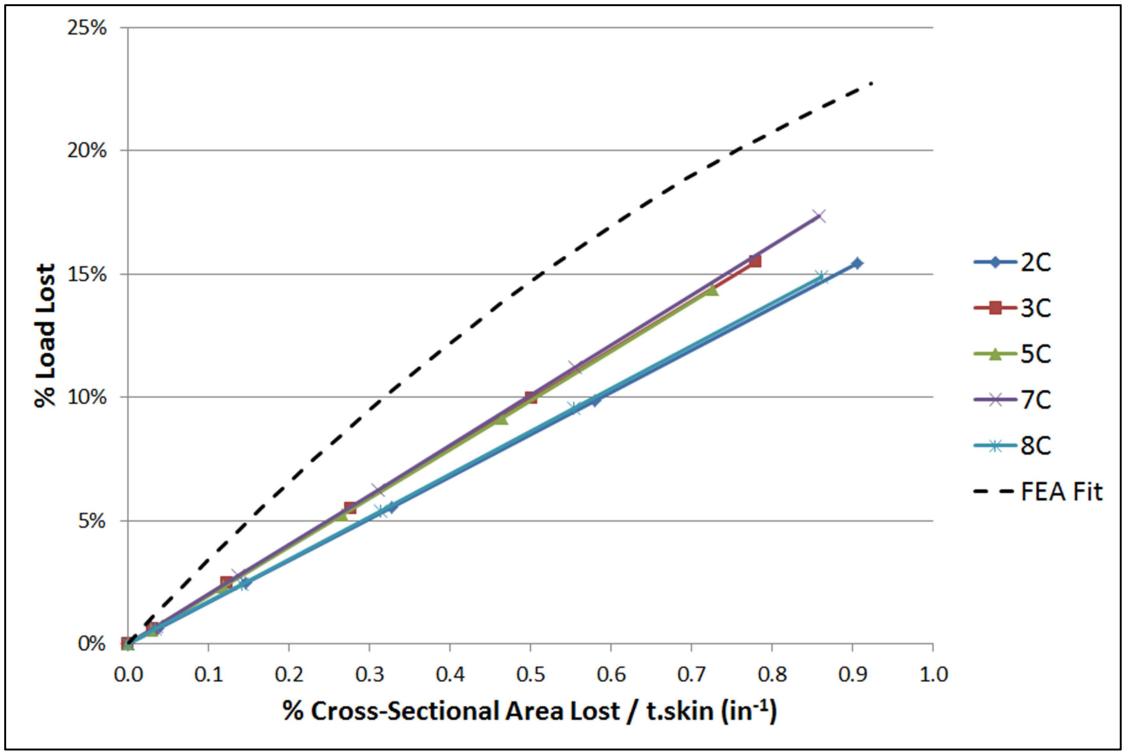

Figure 37 Results of Euler-Engesser Equation

conservative than those examined herein. Therefore, column failure is not further examined in this report.

Approach 2 – integrally stiffened panel (ISP) equation [11]:

$$F_{critical\ (ISP)} = \frac{\eta_c k_c \pi^2 E_c}{12(1-\nu^2)}\left(\frac{t}{b}\right)^2 \tag{15}$$

where

η_c plasticity reduction factor: $(E_t/E)^{0.5}$ [11];

k_c buckling coefficient from geometry-specific charts;

ν Poisson's ratio (assume 0.33 [16]);

t skin thickness;

b distance between stringers.

There are two known versions of this equation as reported in Niu [11] and Bruhn [24].

The OEM structures manual for the aircraft chosen for this study utilizes the Bruhn method, albeit with some factors taken out of the driving equation and added to a modified k_c calculation (though it gives the same end result and is based on the same source data from [9]). Ultimately, the only difference between the Niu and Bruhn methods is the plasticity reduction factor, η_c; the driving equation and k_c determination are identical. More direct comparisons of these two methods are provided in section 4.5.

It is noted that Equation (15) has no direct ability to account for the presence of a blend: the only geometry variables are the skin thickness (t) and spacing between stringers (b). However, modification of the cross-sectional area during stress-to-force conversions can be used to account for changes in cross section. Results of such an approach are shown in Figure 38. The nominal (unblended) skin thickness is used for all stress calculations; the modified cross-sectional area due to blending is used for stress-to-force conversions.

The results of Figure 38 are similar to those shown in Figure 37 for the Euler-Engesser equation: lost load carrying capability is consistently underpredicted. Possibly the most intuitive method to modify the results of Equation (15) is to reduce the assumed skin thickness, t. A highly conservative approach is to simply assume that the skin thickness is fully reduced by the depth of the blend. This approach is shown graphically in Figure 39. Analytical results are shown in Figure 40.

As expected, the results of a full thickness reduction are highly conservative. Additionally, the limited number of data points in Figure 40 is due to limitations in the data which support the stiffened panel analysis method. Specifically, the method does not support determination of the buckling coefficient, k_c, for stringer-to-skin thickness ratios

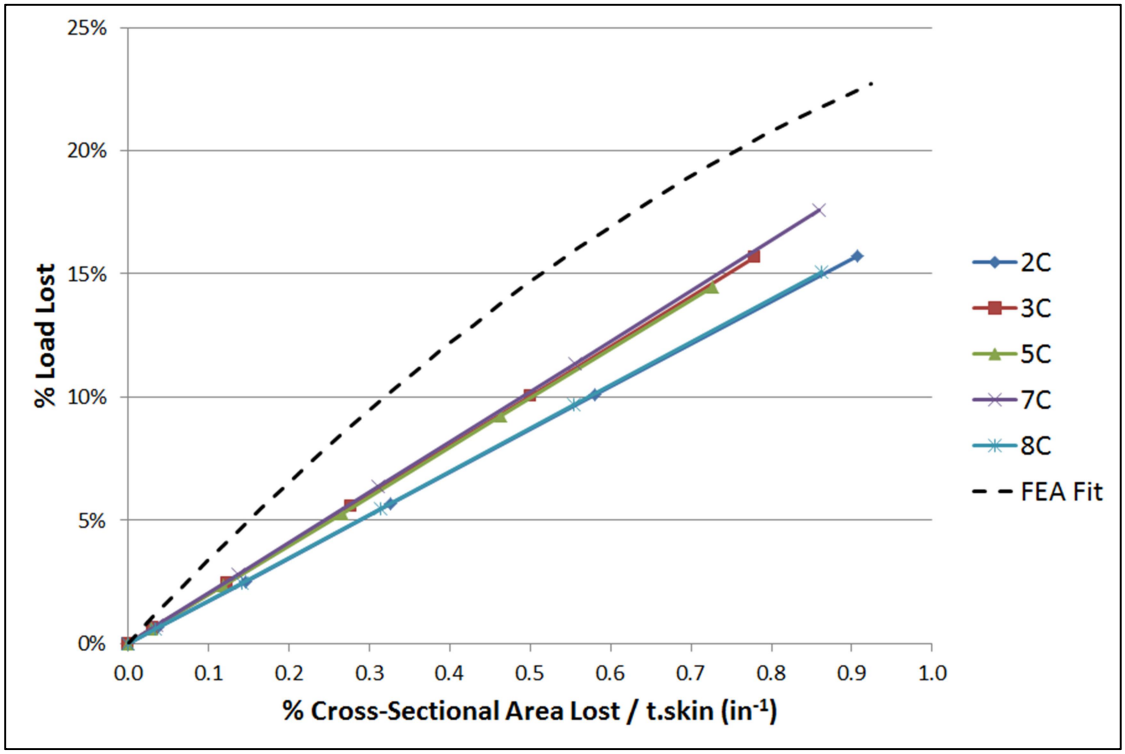

Figure 38 Results of Stiffened Panel Analysis (Nominal Skin Thickness)

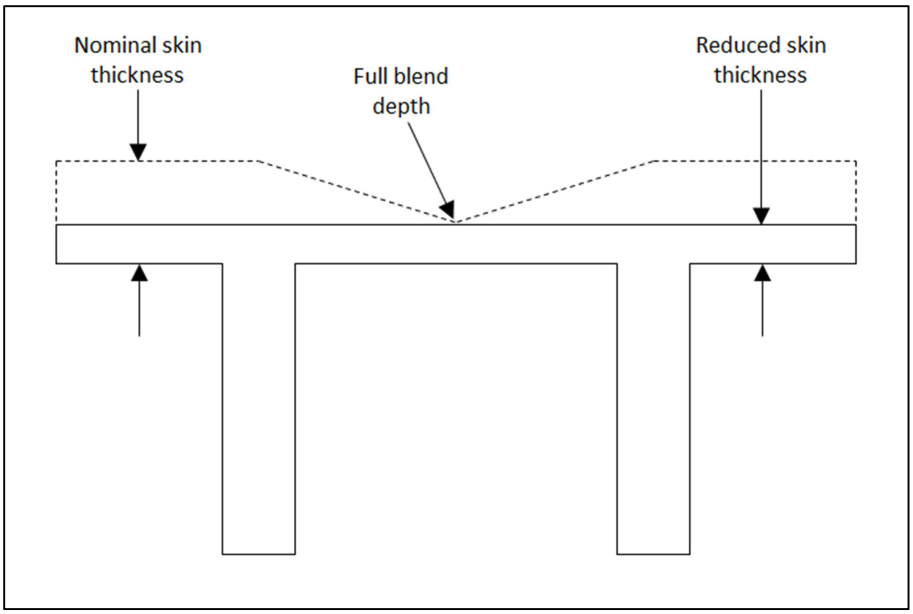

Figure 39 Fully Reduced Skin Thickness

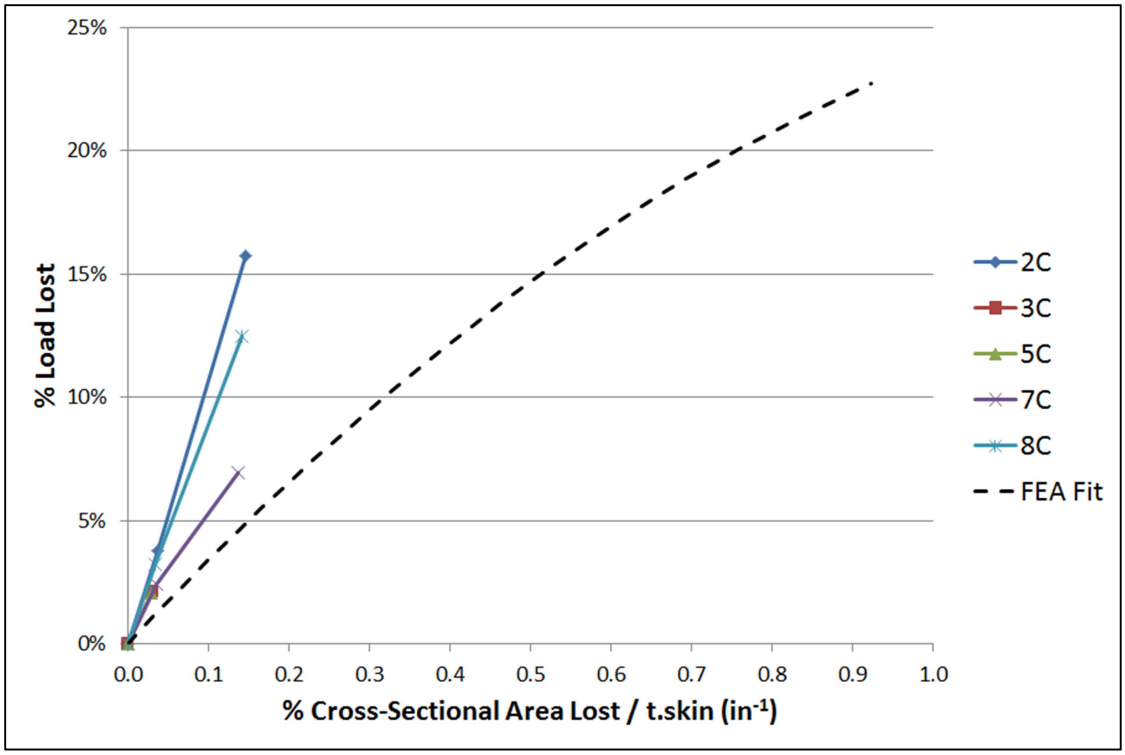

Figure 40 Results of Stiffened Panel Analysis (Full Thickness Reduction)

exceeding 2.0. As a blend gets deeper, the skin thickness is reduced beyond this threshold and the analysis method becomes unsupportable.

The previously discussed relationship between lost area and lost strength suggests an additional method of reducing the skin thickness. In this method, the skin thickness is reduced such that the calculated loss in cross-sectional area is equal to the loss in area due to blending. In equation form, this method is as follows:

$$A_{blend} = A_{reduction} = t_{reduction} * w_{panel} \tag{16}$$

Graphically, this method is shown in Figure 41. Analysis results are shown in Figure 42. Results show that the stiffened panel equation using an equivalent skin thickness is still unconservative, but to a much lower degree than in previous methods (with a worst-case error of approximately 3% as compared to FEA data).

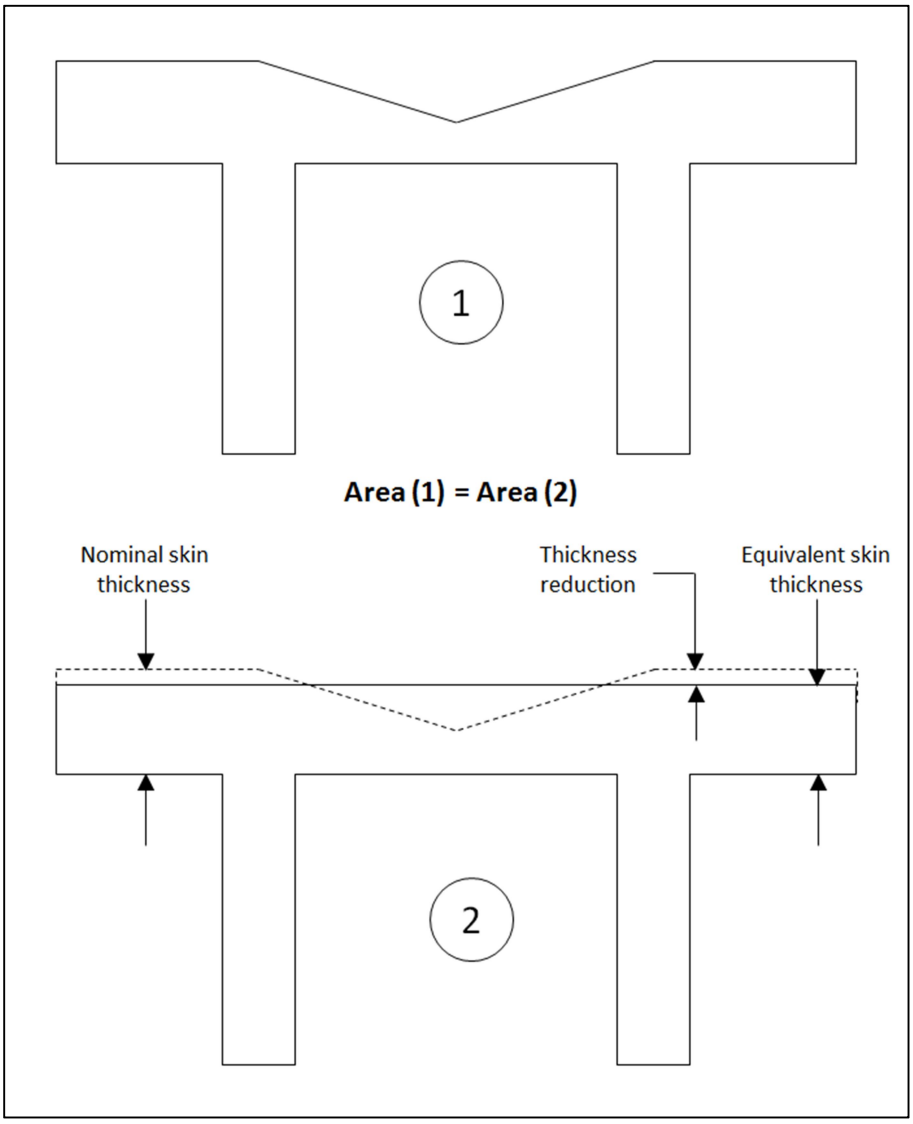

Figure 41 Equivalent Skin Thickness

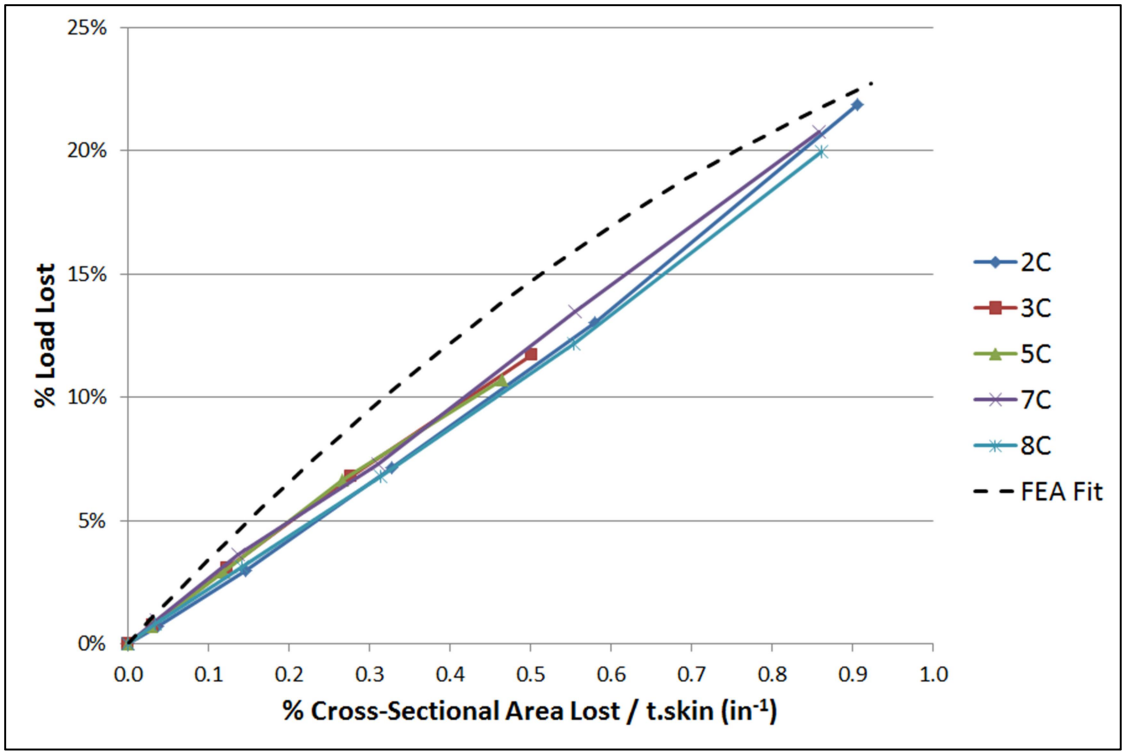

Figure 42 Results of Stiffened Panel Analysis (Equivalent Skin Thickness)

Approach 3 – crippling failure [11]:

$$F_{critical\ (crippling)} = \frac{\sum b_n t_n F_{cc,n}}{\sum b_n t_n} \tag{17}$$

As with the stiffened panel equation, the crippling equation has no direct method to account for the presence of a blend. This section examines the effects of analytical modifications to the assumed skin thickness as previously described in the stiffened panel approach. Results for the nominal skin thickness, full thickness reduction, and equivalent skin thickness are shown in Figure 43, Figure 44, and Figure 45, respectively.

As might be expected, Figure 43 shows unconservative results, while Figure 44 shows overconservative results. Similar trends are noted for the stiffened panel approach. However, the equivalent skin thickness method yields results which are quite similar to the FEA data. With these findings in mind, it is nevertheless noted that all documented

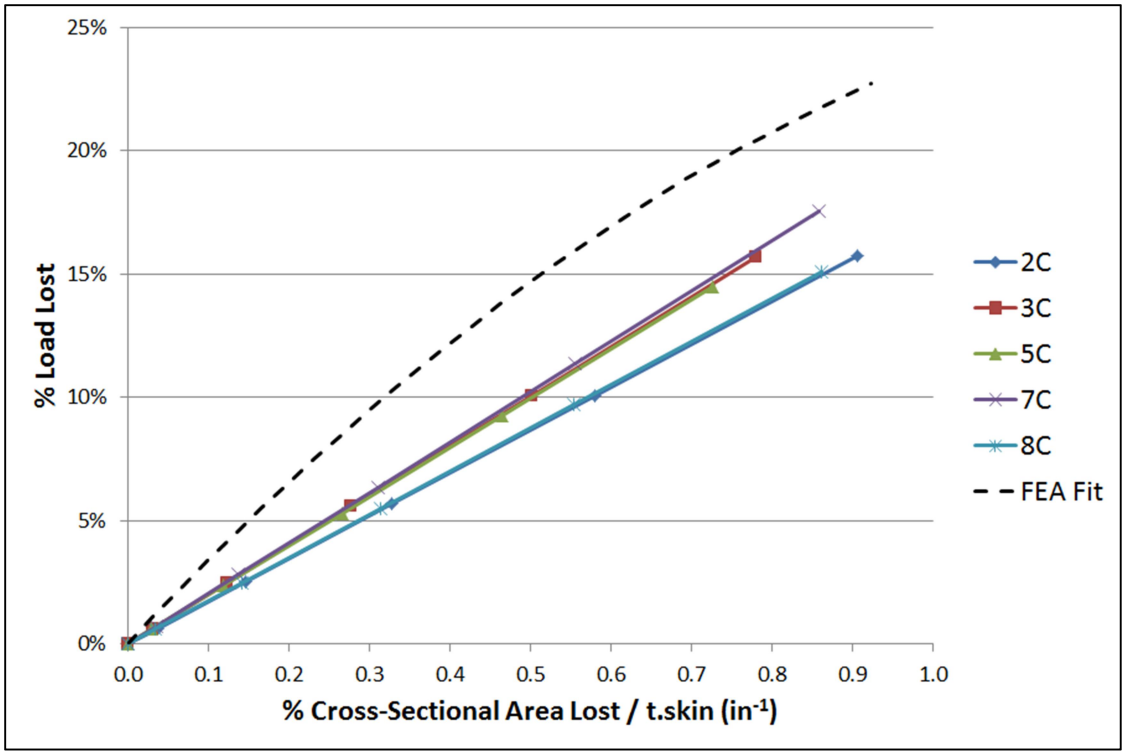

Figure 43 Results of Crippling Analysis (Nominal Skin Thickness)

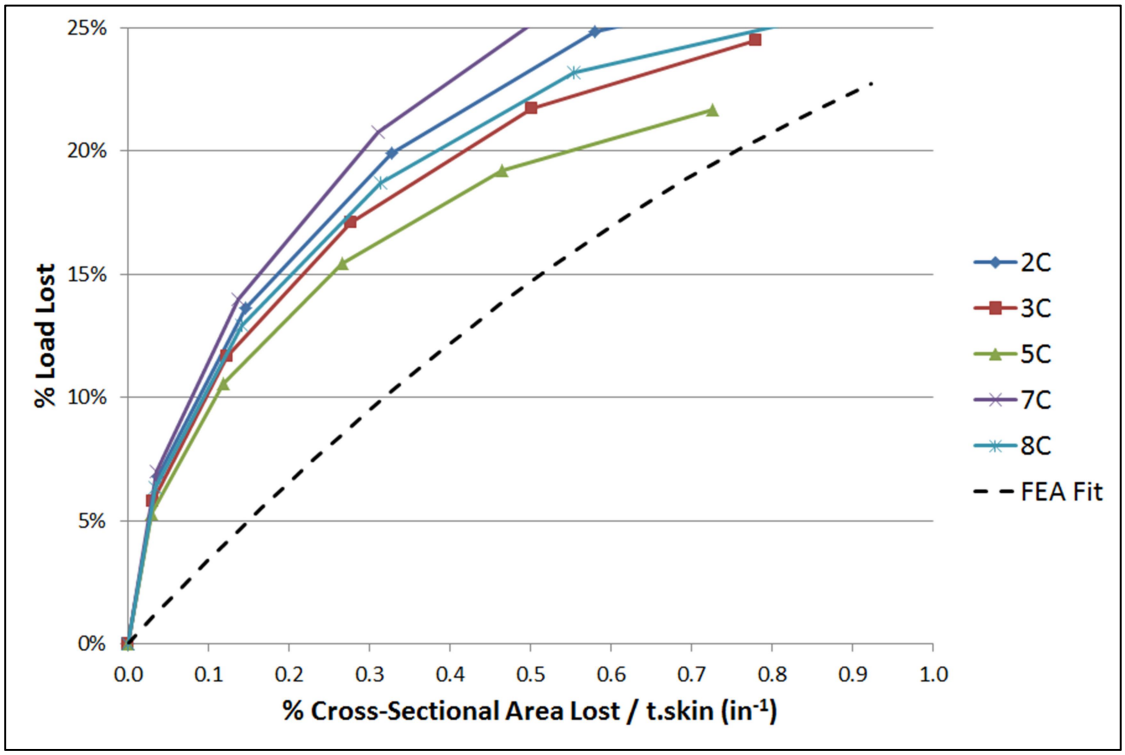

Figure 44 Results of Crippling Analysis (Full Thickness Reduction)

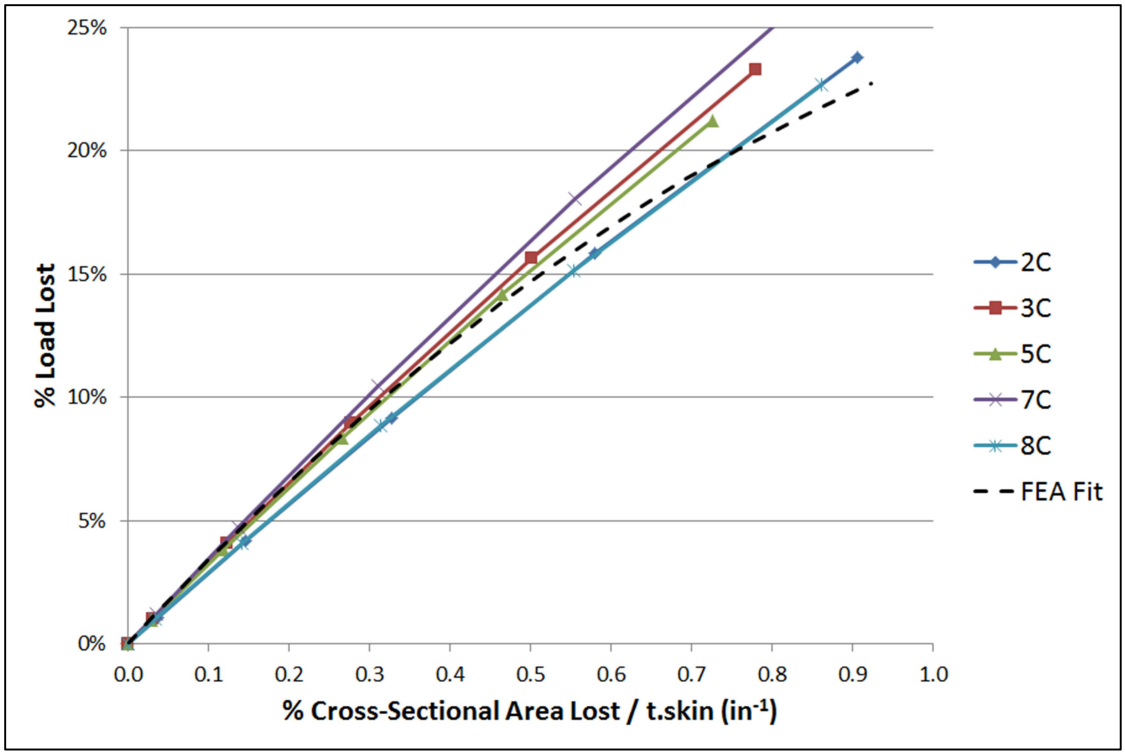

Figure 45 Results of Crippling Analysis (Equivalent Skin Thickness)

results have thus far been based on two-stringer sections. It is unknown how well these results correlate to wider panels.

4.5 Analysis of Wide Panels (Five-Stringer Sections)

This section expands the scope of this study to wide panels (i.e., geometries more appropriate for actual aircraft design). Analytical methods which are further examined include the stiffened panel equation, Equation (15) (both the Niu and Bruhn versions), and the crippling equation, Equation (17), both utilizing an equivalent skin thickness as previously described. Finite element analyses are performed as in section 4.2.1, except the element size is increased from 0.1 in to 0.15 in due to limitations in computer memory. Examination of selected geometries shows that the increased element size yields a change in maximum load of approximately 0.3% as compared to smaller elements,

which is consistent with the convergence testing previously reported in Table 12. The new element size is therefore deemed acceptable for use. Material properties are assumed from the forward skin panel (see Table 10).

The skin and stringer thicknesses chosen for analysis in this section are based on an average of the physical test specimens and are constant along the length (no tapering of thicknesses). Assumed geometry is shown in Figure 46. A single-stringer section is shown; additional stringers are simply added together (i.e., a single-stringer section is 4.1 in wide, a two-stringer section is 8.2 in wide, and so on). In order to document the effects of increasing numbers of stringers, Figure 47 compares the critical stresses for panels consisting of one to five stringers. Analytical results for both stiffened panel equations and the crippling equation are shown for reference.

As can be seen, the critical stress for sections of two to five stringers remains relatively constant. In other words, a five-stringer section can be assumed to fail at approximately the same stress as a two-stringer section (note that the integrally stiffened panel calculations similarly disregard the number of stringers in the panel). Additionally,

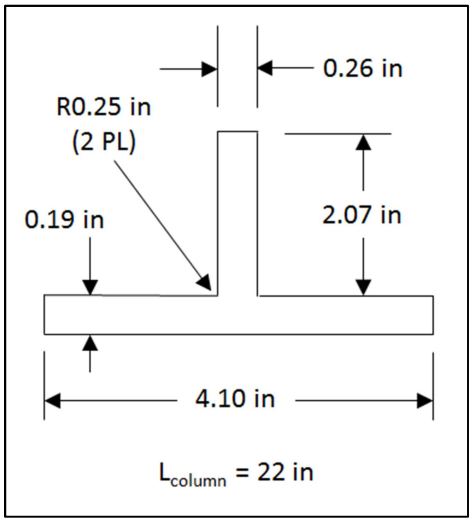

Figure 46 Single Stringer Geometry

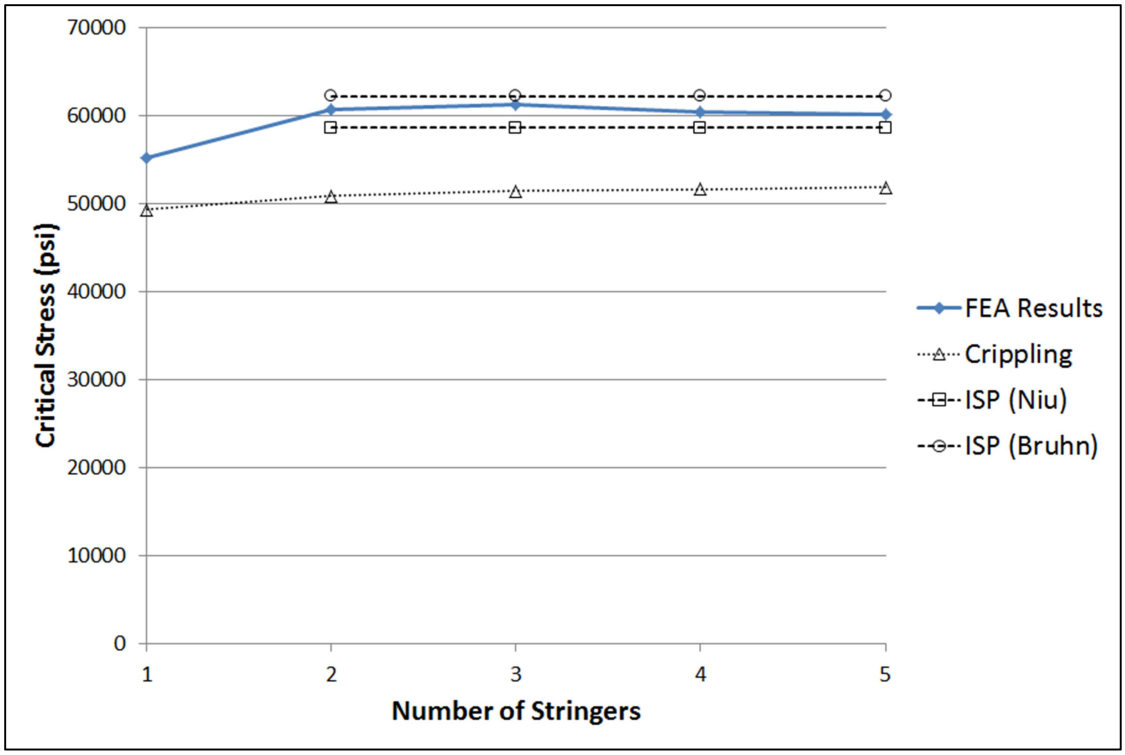

Figure 47 Critical Stress vs. Number of Stringers (Unblended Structure)

the FEA results lie nearly evenly between the analytical results for the Niu and Bruhn stiffened panel calculations, which are themselves separated by approximately 6% (at least for the geometry chosen in this analysis). The crippling calculation shows highly conservative results despite its apparent effectiveness in predicting losses in load carrying capability due to blending (as shown in Figure 45).

Blending of a five-stringer section is examined analytically and numerically, though funding could not be obtained for physical validation testing. As with the two-stringer geometries, both circular and elliptical blends are considered. However, only a single blend depth is considered (at 50% of the skin thickness, or 0.095 in). Instead of varying the blend depth, circular blends are simulated at taper ratios of 10:1, 20:1, 35:1, 50:1, 75:1, and 100:1. The higher ratios allow for examination of blends which are wide

relative to the overall panel width (e.g., a 100:1 blend ratio gives a blend width of 0.095*100*2=19 in, as compared to the overall panel width of 20.5 in). Elliptical blends are simulated at a blend ratio of 20:1 in the axial direction and 10:1, 35:1, 50:1, 75:1, and 100:1 in the transverse direction. Note that the five-stringer simulations examine elliptical blends with the major axis in the transverse direction, whereas the two-stringer simulations in previous sections examine elliptical blends with the major axis in the axial direction. An overview of all simulated blend geometries is shown in Figure 48. A comparison of analytical evaluation results is shown in Figure 49.

It is noted that the results of Figure 49 (five-stringer section) are nearly indistinguishable from the results of Figure 42 and Figure 45 (two-stringer sections), although the two-stringer datasets are omitted from Figure 49 for the purposes of clarity. Therefore, the equivalent skin thickness approach appears to show consistency regardless of blend ratio, blend depth, blend shape, panel width, and number of stringers. Additionally, of the three methods shown, the crippling equation still provides the best data fit. Figure 50 details strength losses in a five-stringer section as predicted by the crippling equation compared to FEA results.

The results shown in Figure 50 highlight three main points. First, the FEA data shows lower than expected losses in load carrying capability for small blends. This effect is also seen for some of the two-stringer sections detailed in Figure 36. The cause of this effect is unknown, but ensures that analytical predictions for small blends are conservative. Second, the FEA data for circular and elliptical blends are highly consistent except at one data point (corresponding to an elliptical blend of taper ratios 20:1 axial and 75:1 transverse). Again, the cause is unknown, but the effects are similarly conservative.

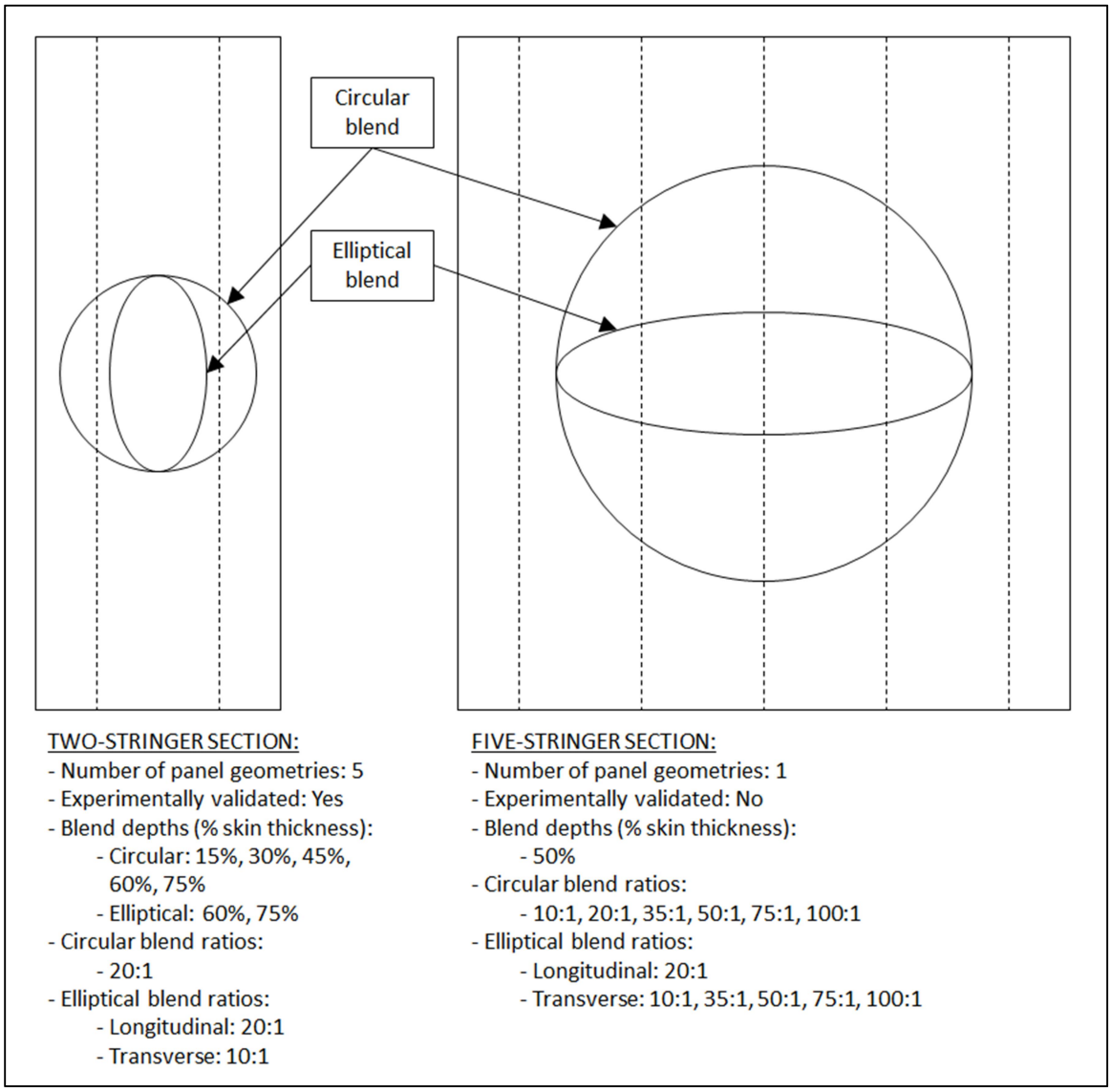

Figure 48 Summary of Blend Geometries

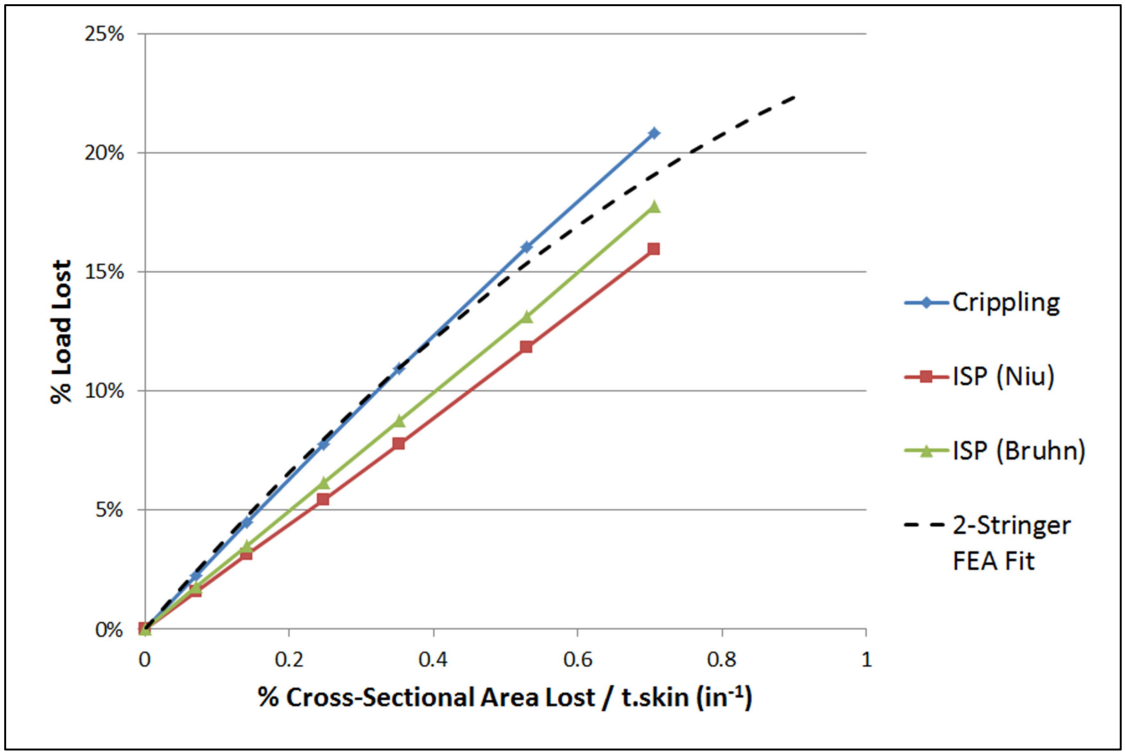

Figure 49 Analytical Results for a Five-Stringer Section

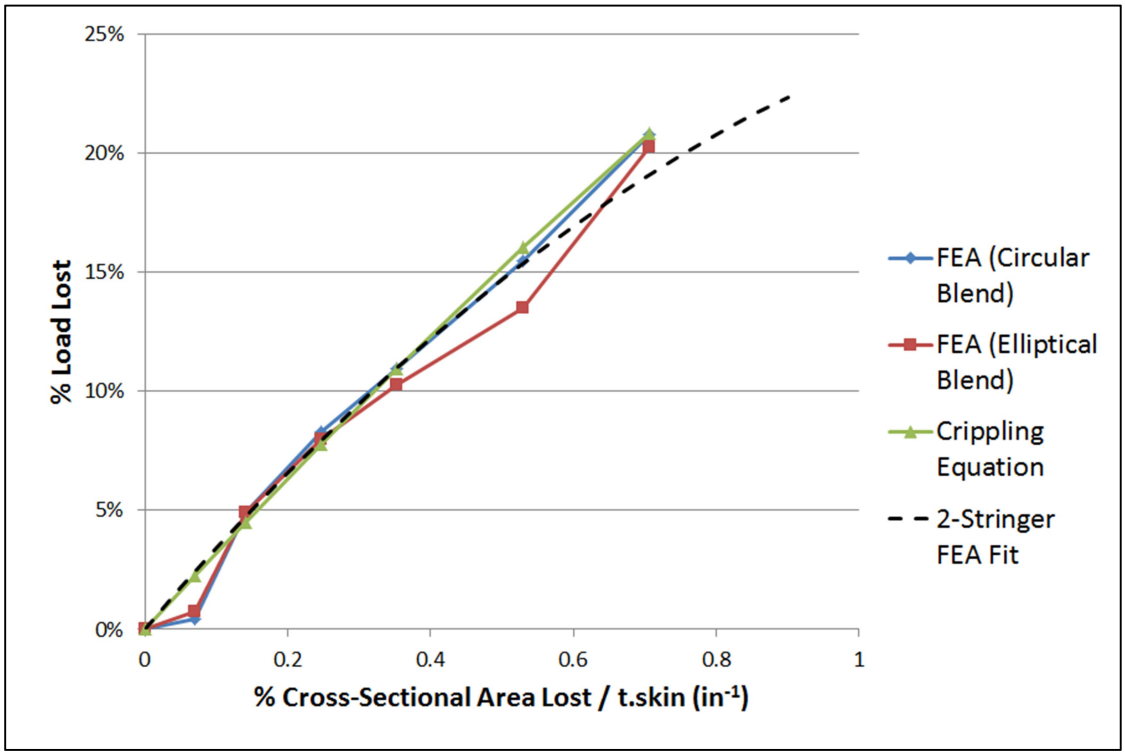

Figure 50 FEA Results for a Five-Stringer Section

Finally, and perhaps most importantly, both FEA datasets are highly consistent with analytical predictions based on the crippling equation (except for the recently discussed conservative data points).

One final comparison is made of the crippling equation's ability to account for losses in load carrying capability as compared to the integrally stiffened panel (ISP) equations. Figure 51 shows the critical stress for a five-stringer section with an equivalent skin thickness using only the integrally stiffened panel equation (both the Niu and Bruhn versions). Figure 52 shows the same FEA data, but with different analytical predictions; nominal (unblended) panel strength is from the integrally stiffened panel equation, but strength losses are determined from the crippling equation.

The obvious trend is that the ISP-only data becomes unconservative (for both the Niu and Bruhn equations) at area losses above approximately 5%. Conversely, the ISP-plus-crippling method gives results that are conservative through the entire data range (at least for Niu's equation; the Bruhn equation gives unconservative results through the entire data range). In fact, the slope of the FEA curves is remarkably similar to the ISP-plus-crippling predictions. Although the ISP-only methods may only be unconservative by a few percent, it is important to note that stability of structures can often be highly variable from one specimen to the next. Thus, it is recommended that unconservative analytical methods, no matter how slight, be avoided. The Niu equation is consistently more conservative than the Bruhn equation for all geometries examined in this study.

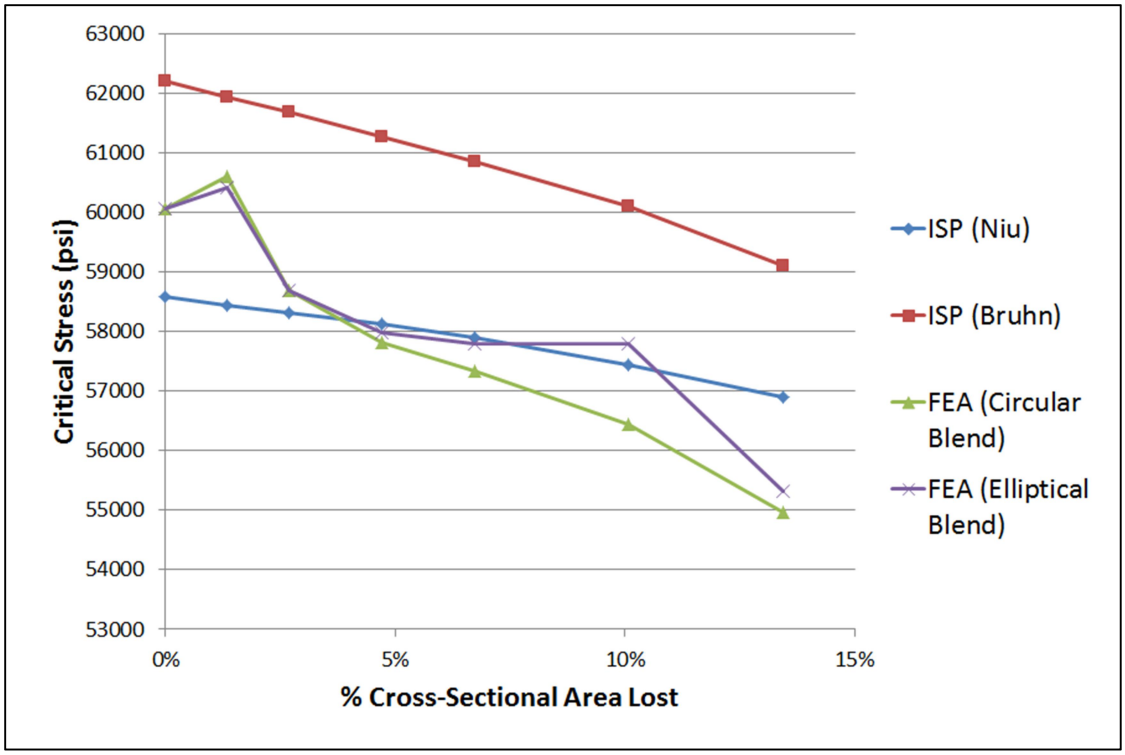

Figure 51 Critical Stress Predictions (Equivalent Thickness, ISP-Only Method)

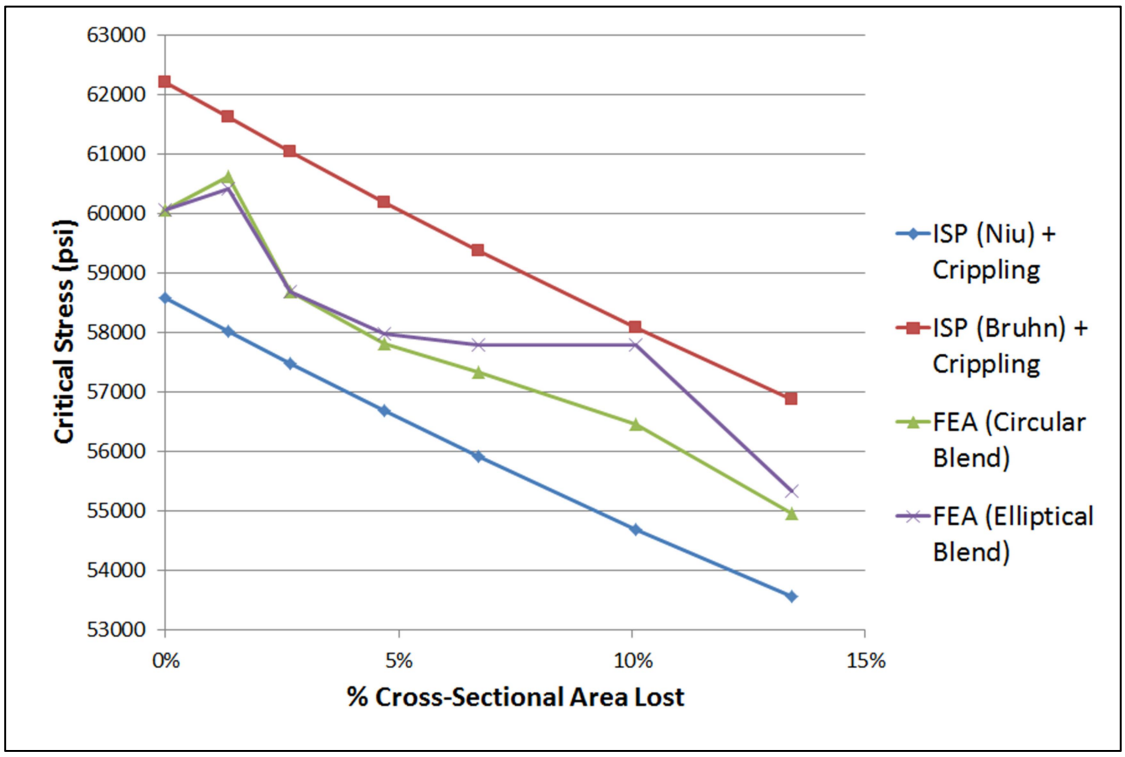

Figure 52 Critical Stress Predictions (Equivalent Thickness, ISP-Plus-Crippling Method)

CHAPTER 5

SUMMARY

5.1 Conclusions

After evaluating the full results of this study, the following conclusions are reported.

1) This study examines the effects of blending on sturdy, integrally stiffened panels with blade-type stringers. Consistent results are reported across a wide range of blend depths, blend ratios, blend shapes, panel widths, and number of stringers.
2) The bulk of this study's findings are based on finite element simulations. Experimental validation of the two-stringer sections shows that nonlinear finite element analysis accurately predicts reductions in buckling resistance due to blending (within 4% of experimental test results). Results of the five-stringer simulations are not experimentally validated, but are consistent with the two-stringer results.
3) Traditional closed-form analysis methods are shown to be poorly suited for analysis of blended structure. However, the use of an equivalent skin thickness in equations which predict local buckling failure (e.g., stiffened panel, crippling) yields accurate results while retaining reasonable conservatism. The equivalent skin thickness is calculated such that the true

skin thickness is reduced by an amount equal to the lost area due to blending. (See also Equation (16) and Figure 41.)

4) The following is reported as the preferred method for analytical evaluation of blended structure:
    a. Determine the analysis location. If the blend is symmetric, use the location of the blend center. If the blend is not symmetric, use the location of maximum cross-sectional area loss. All further calculations will utilize the cross-sectional geometry at this location.
    b. Calculate an equivalent skin thickness for analysis based on the blend's cross-sectional area at the location determined in step a. (See also Equation (16) and Figure 41 of this report.)
    c. Calculate the critical stress for the nominal (unblended) cross section using the stiffened panel method reported by Niu [11]. (See also Equation (15) of this report.)
    d. Recalculate the critical stress of the nominal (unblended) cross section using the crippling method reported by Niu [11]. (See also Equation (17) of this report.)
    e. Calculate the critical stress of the blended cross section using the crippling method reported by Niu [11]. Assume an equivalent skin thickness as calculated in step b. for all skin "flanges."
    f. Divide result e. by result d. This is the percent reduction in buckling resistance.
    g. Multiply result f. by result c. This is the critical stress for the blended

cross section. If desired, conversion to a critical load is possible at this point using the true (blended) cross-sectional area at the location determined in step a.

Note: the above procedures assume that the blended cross section is the critical cross section, which may be untrue for a panel of tapering thickness. These procedures further assume that local buckling (a.k.a. short-wave buckling) is the critical failure mode. Analysis of column failure/long-wave buckling interaction is well documented, to include sections of nonconstant cross section, and is not discussed in detail in this report. Engineering judgment is required in validating the above assumptions before applying these procedures.

5.2 Recommendations

Recommendations for follow-up research, as well as cautionary recommendations for use of the findings included herein, are as follows.

1) The results of this study are based on simulations of blade-type, integral stringers. Further research is recommended before applying these results to additional stringer geometries (e.g., z-stringers or bulbed stringers). Similarly, it is unknown if the findings of this study correlate to built-up panels consisting of stiffeners riveted or bolted to the skin.
2) This study only examines center-of-panel blends. For local buckling failure, the axial location of a blend is assumed to be irrelevant (panel length is not considered in either the crippling or stiffened panel equations). The transverse location of a blend, however, may be relevant. Fortunately, the results of this

study are consistent for both two-stringer and five-stringer geometries. Therefore, it is assumed that the failure stress of a blended panel is independent of the number of stringers. A five-stringer panel with an off-center blend can easily be modeled as, for example, a two-stringer panel with a centered blend. Similarly, a wide panel with multiple blends in a single cross section can easily be modeled as a series of narrower panels, each with a single blend. However, it is recommended that all analytical models utilize a panel width with a minimum of two stringers. Single-stringer sections (i.e., tee extrusions) are not considered stiffened panels and cannot be assumed to fail at similar stresses (see also Figure 47).

3) 7000-series aluminums are assumed as the most common material for compression-dominated structure in metallic aircraft designs [11]. In addition, FEA simulations in this study revealed consistencies in lost load carrying capability between two panel materials, despite a more than 8% difference in material yield stress. This conclusion appears to be supported by a similar study reported in [12]. That study compared two 7000-series aluminum tempers with a 14.8% difference in yield stress, but only a 3.3% difference in lost load carrying capability for a blended structure. Therefore, the results of this study are assumed applicable to all 7000-series aluminums. However, for nonaircraft use (i.e., other than 7000-series aluminums) additional sensitivity studies may be prudent.
4) The presence of fuel vent holes is shown to have a minor, but noticeable, effect on overall compressive load carrying capability. FEA models and

physical test specimens utilized in this study include geometries with vent holes located adjacent to a blend, geometries with vent holes located away from a blend, and geometries without vent holes. Ultimately, the findings of this study are consistent across all three scenarios. Thus, vent hole location is not recommended as a variable in predicting the buckling resistance of blended structure.

5) In FEA simulations, four of the five two-stringer geometries examined show *increased* buckling resistance for blend depths of 15% of the skin thickness (a phenomenon noted and briefly discussed in a similar experiment [12], but not further speculated upon herein). Two specimens also show greater than expected buckling resistance at a 30% blend depth. Similar results are reported for the sole five-stringer geometry examined. Thus, the results of this study may be overly conservative for blends which are small relative to the overall panel size. Additional research which is focused on small blends may yield improved results in this area. However, the proximity of fuel vent holes to a blend is anticipated to be of significantly greater importance in such attempts to reduce the conservatism of small blend analyses. This factor should not be neglected.
6) Shear loading was neglected from this study despite being present to some degree under true flight loads. Evaluation of the magnitudes of shear loads in a given aircraft structure may be prudent before applying the results of this study to real-world design.
7) This study did not examine phenomena such as the onset of plasticity or

yielding. Although such factors are known to be significantly affected by the presence of a surface blend [12], their use as failure criteria in traditional aircraft stability analysis and design is assumed to be uncommon. The results of this study are applicable only to the maximum load carrying capability of an integrally stiffened panel (i.e., final failure). Alternate failure criteria are incompatible with the findings of this study.

APPENDIX A

COMPRESSION SPECIMEN GEOMETRY

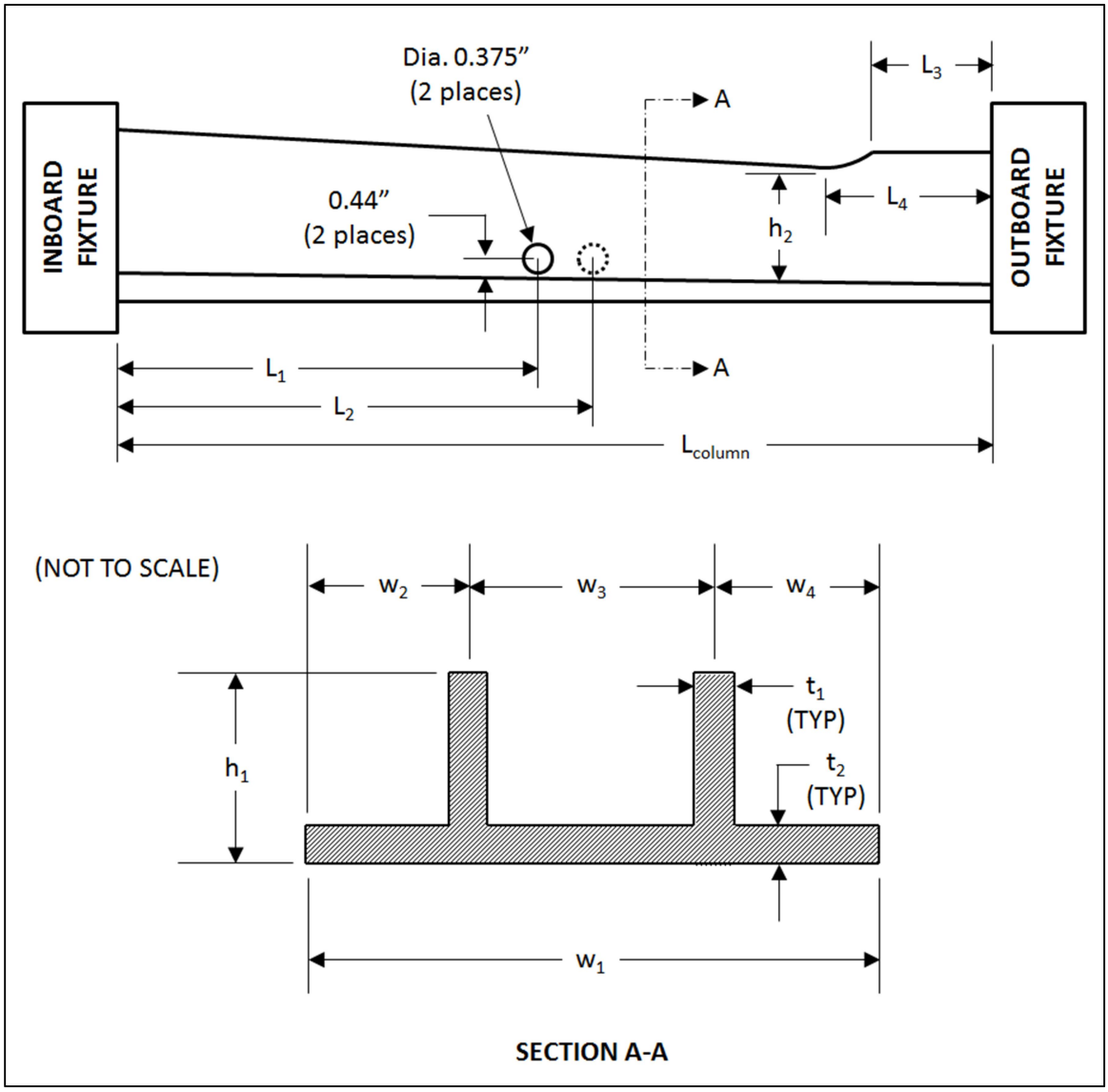

Figure 53 Compression Specimen Geometry Overview

Table 21 Specimen 2B Geometry (Aft Skin Panel)

	Inboard	Center	Outboard		Vent Holes
t_1 (in)	0.222	0.2120	0.202	d_{hole} (in)	0.375
t_2 (in)	0.177	0.1745	0.172	L_1 (in)	15.00
w_1 (in)	8.062	8.062	8.062	L_2 (in)	16.00
w_2 (in)	1.995	1.995	1.995	L_{column} (in)	24.10
w_3 (in)	4.079	4.079	4.079		
w_4 (in)	1.988	1.988	1.988		
h_1 (in)	2.0325	1.9645	2.1210		
	For Stepped Sections Only:				
h_2 (in)	--	--	1.740		
L_3 (in)	--	--	4.357		
L_4 (in)	--	--	3.070		
	Section Properties:				
A (in^2)	2.2508	2.1658	2.1741		
I (in^4)	0.7795	0.6819	0.8175		
ρ (in)	0.5885	0.5611	0.6132		

Table 22 Specimen 2C Geometry (Aft Skin Panel)

	Inboard	Center	Outboard		Vent Holes
t_1 (in)	0.222	0.2120	0.202	**d_{hole} (in)**	0.375
t_2 (in)	0.177	0.1735	0.170	**L_1 (in)**	13.13
w_1 (in)	8.074	8.074	8.074	**L_2 (in)**	14.19
w_2 (in)	1.999	1.999	1.999	**L_{column} (in)**	24.27
w_3 (in)	4.084	4.084	4.084		
w_4 (in)	1.991	1.991	1.991		
h_1 (in)	2.0210	1.9486	2.1090		
	For Stepped Sections Only:				
h_2 (in)	--	--	1.726		
L_3 (in)	--	--	4.983		
L_4 (in)	--	--	3.090		
	Section Properties:				
A (in^2)	2.2479	2.1535	2.1559		
I (in^4)	0.7673	0.6659	0.8033		
ρ (in)	0.5842	0.5561	0.6104		
	With 0.08" Blend (20:1 Ratio):				
A (in^2)	--	2.0250	--		
I (in^4)	--	0.6440	--		
ρ (in)	--	0.5639	--		

Table 23 Specimen 3B Geometry (Forward Skin Panel)

	Inboard	Center	Outboard		Vent Holes
t_1 (in)	0.308	0.2935	0.279	**d_{hole} (in)**	0.375
t_2 (in)	0.200	0.1970	0.194	**L_1 (in)**	17.19
w_1 (in)	8.095	8.095	8.095	**L_2 (in)**	18.13
w_2 (in)	2.024	2.024	2.024	**L_{column} (in)**	21.77
w_3 (in)	4.039	4.039	4.039		
w_4 (in)	2.032	2.032	2.032		
h_1 (in)	2.5090	2.4005	2.2920		
For Stepped Sections Only:					
h_2 (in)	--	--	--		
L_3 (in)	--	--	--		
L_4 (in)	--	--	--		
Section Properties:					
A (in^2)	3.0414	2.8882	2.7411		
I (in^4)	1.8290	1.5574	1.3151		
ρ (in)	0.7755	0.7343	0.6927		

Table 24 Specimen 3C Geometry (Forward Skin Panel)

	Inboard	Center	Outboard		Vent Holes
t_1 (in)	0.307	0.2920	0.277	d_{hole} (in)	0.375
t_2 (in)	0.205	0.2010	0.197	L_1 (in)	15.19
w_1 (in)	8.080	8.080	8.080	L_2 (in)	16.25
w_2 (in)	2.025	2.025	2.025	L_{column} (in)	22.02
w_3 (in)	4.049	4.049	4.049		
w_4 (in)	2.006	2.006	2.006		
h_1 (in)	2.5203	2.4125	2.3047		
For Stepped Sections Only:					
h_2 (in)	--	--	--		
L_3 (in)	--	--	--		
L_4 (in)	--	--	--		
Section Properties:					
A (in^2)	3.0780	2.9156	2.7594		
I (in^4)	1.8557	1.5786	1.3318		
ρ (in)	0.7765	0.7358	0.6947		
With 0.08" Blend (20:1 Ratio):					
A (in^2)	--	2.7871	--		
I (in^4)	--	1.5289	--		
ρ (in)	--	0.7406	--		

Table 25 Specimen 5B Geometry (Forward Skin Panel)

	Inboard	Center	Outboard		Vent Holes
t_1 (in)	0.312	0.3120	0.312	**d_{hole} (in)**	0.375
t_2 (in)	0.196	0.1960	0.196	**L_1 (in)**	18.89
w_1 (in)	8.085	8.085	8.085	**L_2 (in)**	19.75
w_2 (in)	2.037	2.037	2.037	**L_{column} (in)**	21.33
w_3 (in)	4.038	4.038	4.038		
w_4 (in)	2.010	2.010	2.010		
h_1 (in)	2.5270	2.5270	2.5270		
For Stepped Sections Only:					
h_2 (in)	--	--	--		
L_3 (in)	--	--	--		
L_4 (in)	--	--	--		
Section Properties:					
A (in^2)	3.0392	3.0392	3.0392		
I (in^4)	1.8744	1.8744	1.8744		
ρ (in)	0.7853	0.7853	0.7853		

Table 26 Specimen 5C Geometry (Forward Skin Panel)

	Inboard	Center	Outboard		Vent Holes
t_1 (in)	0.313	0.3130	0.313	d_{hole} (in)	0.375
t_2 (in)	0.199	0.1990	0.199	L_1 (in)	16.00
w_1 (in)	8.081	8.081	8.081	L_2 (in)	17.00
w_2 (in)	2.014	2.014	2.014	L_{column} (in)	21.24
w_3 (in)	4.071	4.071	4.071		
w_4 (in)	1.996	1.996	1.996		
h_1 (in)	2.5430	2.5430	2.5430		
For Stepped Sections Only:					
h_2 (in)	--	--	--		
L_3 (in)	--	--	--		
L_4 (in)	--	--	--		
Section Properties:					
A (in^2)	3.0755	3.0755	3.0755		
I (in^4)	1.9176	1.9176	1.9176		
ρ (in)	0.7896	0.7896	0.7896		
With 0.14" Blend (10:1 Ratio):					
A (in^2)	--	2.8790	--		
I (in^4)	--	1.8261	--		
ρ (in)	--	0.7964	--		

Table 27 Specimen 7B Geometry (Forward Skin Panel)

	Inboard	Center	Outboard		Vent Holes
t_1 (in)	0.275	0.2575	0.240	d_{hole} (in)	0.375
t_2 (in)	0.211	0.2010	0.191	L_1 (in)	17.50
w_1 (in)	8.092	8.092	8.092	L_2 (in)	18.50
w_2 (in)	2.027	2.027	2.027	L_{column} (in)	21.60
w_3 (in)	4.046	4.046	4.046		
w_4 (in)	2.019	2.019	2.019		
h_1 (in)	2.3023	2.1820	2.0617		
	For Stepped Sections Only:				
h_2 (in)	--	--	--		
L_3 (in)	--	--	--		
L_4 (in)	--	--	--		
	Section Properties:				
A (in^2)	2.8576	2.6467	2.4435		
I (in^4)	1.3362	1.0854	0.8701		
ρ (in)	0.6838	0.6404	0.5967		

Table 28 Specimen 7C Geometry (Forward Skin Panel)

	Inboard	Center	Outboard		Vent Holes
t_1 (in)	0.273	0.2560	0.239	d_{hole} (in)	0.375
t_2 (in)	0.215	0.2045	0.194	L_1 (in)	0.375
w_1 (in)	8.079	8.079	8.079	L_2 (in)	15.63
w_2 (in)	2.022	2.022	2.022	L_{column} (in)	16.63
w_3 (in)	4.053	4.053	4.053		
w_4 (in)	2.004	2.004	2.004		
h_1 (in)	2.3145	2.1940	2.0735		
For Stepped Sections Only:					
h_2 (in)	--	--	--		
L_3 (in)	--	--	--		
L_4 (in)	--	--	--		
Section Properties:					
A (in^2)	2.8833	2.6708	2.4657		
I (in^4)	1.3525	1.1000	0.8832		
ρ (in)	0.6849	0.6418	0.5985		
With 0.11" Blend (10:1 Ratio):					
A (in^2)	--	2.5494	--		
I (in^4)	--	1.0702	--		
ρ (in)	--	0.6479	--		

Table 29 Specimen 8B Geometry (Aft Skin Panel)

	Inboard	Center	Outboard		Vent Holes
t_1 (in)	0.236	0.2265	0.217	**d_{hole} (in)**	0.375
t_2 (in)	0.190	0.1800	0.170	**L_1 (in)**	12.63
w_1 (in)	8.083	8.083	8.083	**L_2 (in)**	13.50
w_2 (in)	2.006	2.006	2.006	**L_{column} (in)**	21.65
w_3 (in)	4.078	4.078	4.078		
w_4 (in)	1.999	1.999	1.999		
h_1 (in)	2.1449	2.0935	2.0421		
	For Stepped Sections Only:				
h_2 (in)	--	--	--		
L_3 (in)	--	--	--		
L_4 (in)	--	--	--		
	Section Properties:				
A (in^2)	2.4585	2.3218	2.1866		
I (in^4)	0.9614	0.8636	0.7729		
ρ (in)	0.6253	0.6099	0.5945		

Table 30 Specimen 8C Geometry (Aft Skin Panel)

	Inboard	Center	Outboard		Vent Holes
t_1 (in)	0.238	0.2275	0.217	**d_{hole} (in)**	0.375
t_2 (in)	0.184	0.1750	0.166	**L_1 (in)**	10.50
w_1 (in)	8.081	8.081	8.081	**L_2 (in)**	11.50
w_2 (in)	2.005	2.005	2.005	**L_{column} (in)**	21.66
w_3 (in)	4.075	4.075	4.075		
w_4 (in)	2.001	2.001	2.001		
h_1 (in)	2.1309	2.0795	2.0281		
	For Stepped Sections Only:				
h_2 (in)	--	--	--		
L_3 (in)	--	--	--		
L_4 (in)	--	--	--		
	Section Properties:				
A (in^2)	2.4136	2.2807	2.1496		
I (in^4)	0.9450	0.8464	0.7552		
ρ (in)	0.6257	0.6092	0.5927		
	With 0.08" Blend (20:1 Ratio):				
A (in^2)	--	2.1522	--		
I (in^4)	--	0.8181	--		
ρ (in)	--	0.6165	--		

APPENDIX B

ELECTRON DISCHARGE MACHINING DETAIL

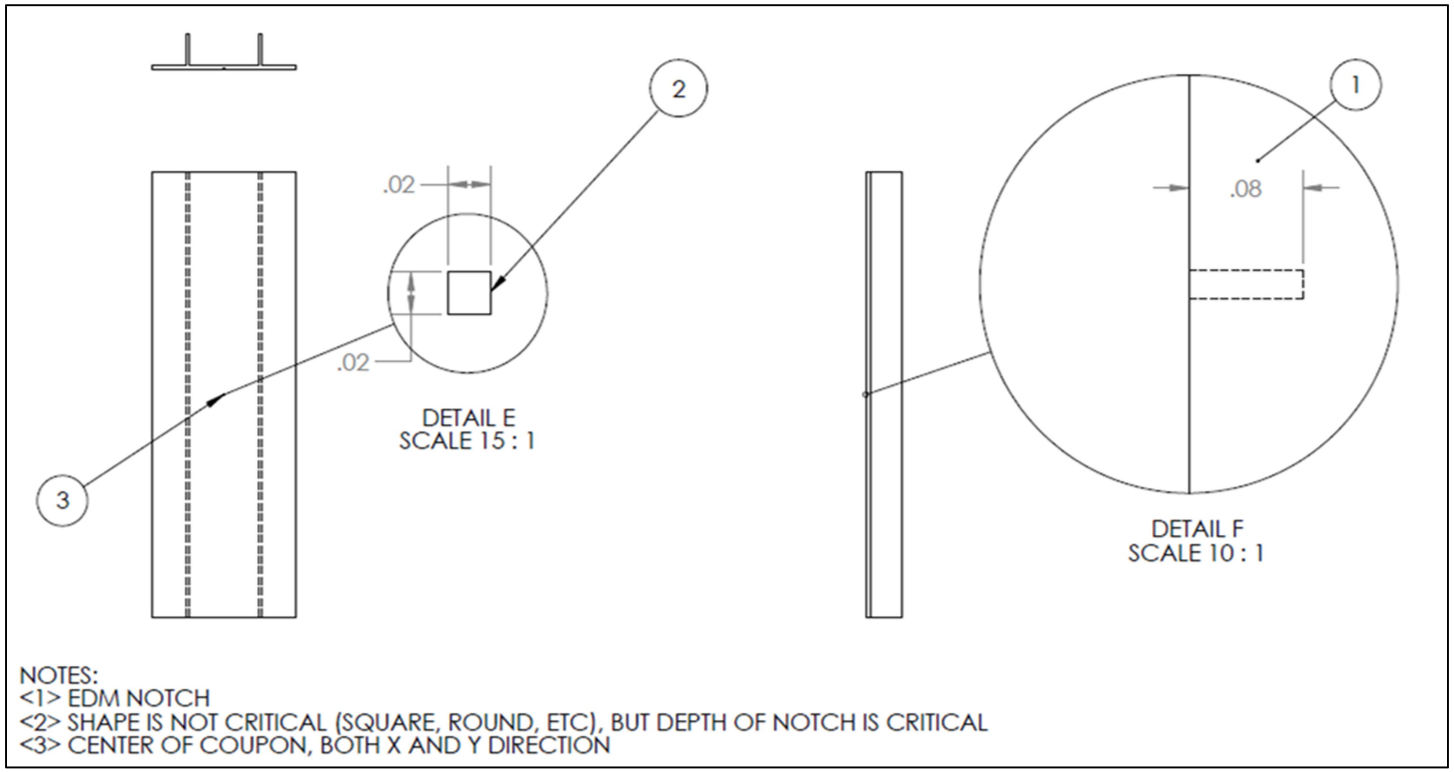

Figure 54 Electron Discharge Machining (EDM) Detail, 0.08 In Depth

APPENDIX C

BAR SPECIMEN MATERIAL CERTIFICATION

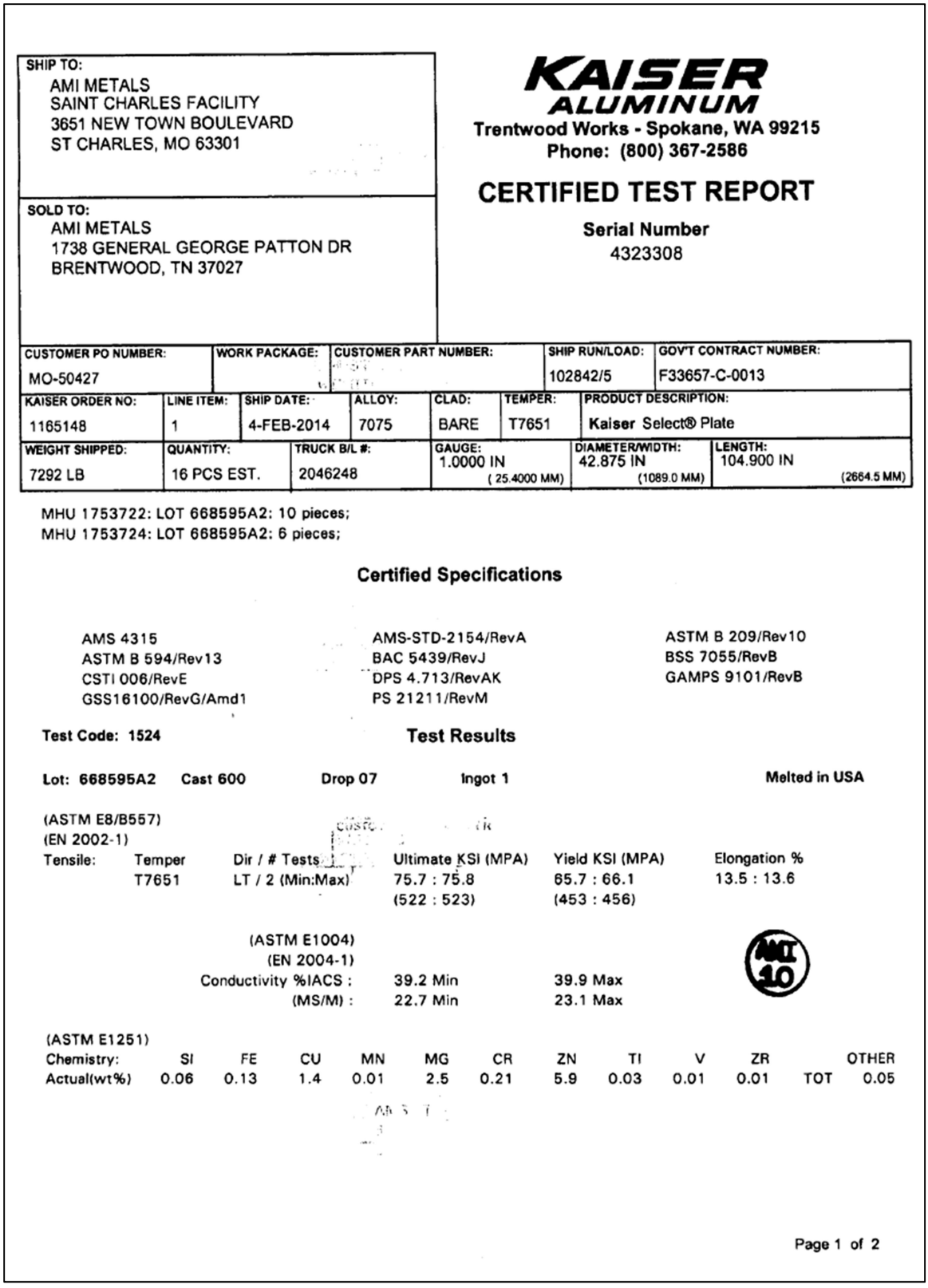

SHIP TO:
AMI METALS
SAINT CHARLES FACILITY
3651 NEW TOWN BOULEVARD
ST CHARLES, MO 63301

SOLD TO:
AMI METALS
1738 GENERAL GEORGE PATTON DR
BRENTWOOD, TN 37027

KAISER ALUMINUM
Trentwood Works - Spokane, WA 99215
Phone: (800) 367-2586

CERTIFIED TEST REPORT

Serial Number
4323308

CUSTOMER PO NUMBER:	WORK PACKAGE:	CUSTOMER PART NUMBER:	SHIP RUN/LOAD:	GOV'T CONTRACT NUMBER:
MO-50427			102842/5	F33657-C-0013

KAISER ORDER NO:	LINE ITEM:	SHIP DATE:	ALLOY:	CLAD:	TEMPER:	PRODUCT DESCRIPTION:
1165148	1	4-FEB-2014	7075	BARE	T7651	Kaiser Select® Plate

WEIGHT SHIPPED:	QUANTITY:	TRUCK B/L #:	GAUGE:	DIAMETER/WIDTH:	LENGTH:
7292 LB	16 PCS EST.	2046248	1.0000 IN (25.4000 MM)	42.875 IN (1089.0 MM)	104.900 IN (2664.5 MM)

MHU 1753722: LOT 668595A2: 10 pieces;
MHU 1753724: LOT 668595A2: 6 pieces;

Certified Specifications

AMS 4315
ASTM B 594/Rev13
CSTI 006/RevE
GSS16100/RevG/Amd1
AMS-STD-2154/RevA
BAC 5439/RevJ
DPS 4.713/RevAK
PS 21211/RevM
ASTM B 209/Rev10
BSS 7055/RevB
GAMPS 9101/RevB

Test Code: 1524

Test Results

Lot: 668595A2 **Cast 600** **Drop 07** **Ingot 1** **Melted in USA**

(ASTM E8/B557)
(EN 2002-1)

Tensile:	Temper	Dir / # Tests	Ultimate KSI (MPA)	Yield KSI (MPA)	Elongation %
	T7651	LT / 2 (Min:Max)	75.7 : 75.8 (522 : 523)	65.7 : 66.1 (453 : 456)	13.5 : 13.6

(ASTM E1004)
(EN 2004-1)

Conductivity %IACS :	39.2 Min	39.9 Max
(MS/M) :	22.7 Min	23.1 Max

(ASTM E1251)

Chemistry:	SI	FE	CU	MN	MG	CR	ZN	TI	V	ZR		OTHER
Actual(wt%)	0.06	0.13	1.4	0.01	2.5	0.21	5.9	0.03	0.01	0.01	TOT	0.05

Page 1 of 2

Figure 55 Bar Specimen Material Certification Test Report

REFERENCES

[1] Federal Aviation Administration, "Fact sheet - FAA's aging airplane program," Mar. 29, 2006. [Online]. Available: http://www.faa.gov/news/fact_sheets/news_story.cfm?contentKey=4027

[2] R. Tyron, A. Dey, R. McDaniels, and J. Burns, "Improved life cycle management of corroded structures," presented at the Aircraft Airworthiness and Sustainment Conf., Grapevine, TX, 2016.

[3] F. C. Spinney, "Defense death spiral," Defense and the Nat. Interest, 1998. [Online]. Available: http://pogoarchives.org/labyrinth/01/05.pdf

[4] The Boeing Company, "Structures engineering support for out-of-production airplanes," *Aero*, vol. 1, no. 2, Jun. 1998. [Online]. Available: http://www.boeing.com/commercial/aeromagazine/aero_02/ps/ps01/index.html

[5] R. M. Pillo and A. Hoggard, "Complying with the aging airplane safety rule," *Aero*, vol. 1, no. 38, pp. 15-19, Jun. 2010.

[6] "Sustaining Air Force aging aircraft into the 21st century," United States Air Force Scientific Advisory Board, Washington, DC, USA, Rep. SAB-TR-11-01, 2011.

[7] J. Yoon, G. Bray, R. Valente, and T. Childs, "Buckling analysis for an integrally stiffened panel structure with a friction stir weld," *Thin-Walled Structures*, vol. 47, no. 12, pp. 1608-1622, Dec. 2009.

[8] C. Hurst and P. Saville, "Reimagining residual strength analyses for stiffened panels," presented at the Aircraft Airworthiness and Sustainment Conf., Baltimore, MD, 2015.

[9] H. Becker, "Handbook of structural stability Part II - Buckling of composite elements," Nat. Advisory Committee for Aeronautics, Washington, DC, USA, Tech. Note 3782, 1957.

[10] "Acceptable methods, techniques, and practices - Aircraft inspection and repair," Federal Aviation Admin., Washington, DC, USA, Advisory Circular 43.13-1B, 1998.

[11] M. C. Y. Niu, *Airframe Stress Analysis and Sizing*, 2nd ed. Hong Kong, China:

Conmilit Press, 1999.

[12] G. Li, G. Shi, and M. Yanishevsky, "Numerical simulation of C-141 lower wing panels with and without simulated exfoliation corrosion under compression," in *25th Int. Congr. Aeronautical Sci.*, Hamburg, 2006, pp. 2-8.

[13] M. Casafont, M. Pastor, J. Bonada, F. Roure, and T. Pekoz, "Linear buckling analysis of perforated steel storage rack columns with the finite strip method," *Thin-Walled Structures*, vol. 61, pp. 71-85, Dec. 2012.

[14] E. Riks, "Buckling and post-buckling analysis of stiffened panels in wing box structures," *Int. J. of Solids and Structures*, vol. 37, no. 46-47, pp. 6975-6824, Nov. 2000.

[15] J. Caseiro, R. Valente, A. Andrade-Campos, and J. Yoon, "Elasto-plastic buckling of integrally stiffened panels (ISP): An optimization approach for the design of cross-section profiles," *Thin-Walled Structures*, vol. 49, no. 7, pp. 864-873, Jul. 2011.

[16] "Metallic materials and elements for aerospace vehicle structures," United States Department of Defense, Washington, DC, USA, Rep. MIL-HDBK-5J, 2003.

[17] *Standard Test Methods of Compression Testing of Metallic Materials at Room Temperature*, ASTM Standard E9, 2009.

[18] C. Rans, P. V. Straznicky, and R. Alderliesten, "Riveting process induced residual stresses around solid rivets in mechanical joints," *J. of Aircraft*, vol. 44, no. 1, pp. 323-329, Jan. 2007.

[19] "Material safety data sheet," Aldon Corporation, Avon, NY, USA, MSDS No. WW 40, 1998.

[20] D. G. Kim, X. N. Dong, T. Cao, K. C. Baker, R. R. Shaffer, and Y. N. Fyhrie, "Evaluation of filler materials used for uniform load distribution at boundaries during structural biomechanics testing of whole vertebrae," *J. of Biomechanical Eng.*, vol. 128, no. 1, pp. 161-165, Feb. 2006.

[21] "Super 'L' hydraulic universal testing machines for critical materials testing up to 3,000 kN," Tinius Olsen, Horsham, PA, USA, Bulletin 117-G, 2010.

[22] *Standard Test Method for Young's Modulus, Tangent Modulus, and Chord Modulus*, ASTM Standard E111, 2004.

[23] "Metallic materials properties development and standardization (MMPDS)," Federal Aviation Admin., Washington, DC, USA, Rep. MMPDS-06, 2011.

[24] E. Bruhn, *Analysis and Design of Flight Vehicle Structures*, Indianapolis, IN, USA:

Jacobs Publishing, 1973.

[25] *ANSYS Mechanical, Introduction to Structural Nonlinearities - Lecture 4: Rate Independent Plasticity*, 16.0 Release, ANSYS Inc., Canonsburg, PA, 2015, pp. 26-27.

[26] T. Megson, *Structural and Stress Analysis*, 2nd ed., Oxford, UK: Elsevier, 2005.

[27] S. R. Schmid, *Fundamentals of Machine Elements*, 3rd ed., Boca Raton, FL, USA: Taylor & Francis Group, 2014.

[28] O. Basquin, "Tangent modulus and the strength of steel columns in tests," *Technologic Papers of the Bureau of Standards*, vol. 18, no. 263, pp. 381-442, Sep. 1924.